

Simulation Studies of the Mechanisms of Interaction between Carbon Nanotubes and Amino Acids

by

George Bassem Botros Abadir

B.Sc., Ain Shams University, Cairo, Egypt, 2000

M.Sc., Ain Shams University, Cairo, Egypt, 2005

A THESIS SUBMITTED IN PARTIAL FULFILLMENT OF
THE REQUIREMENTS FOR THE DEGREE OF

DOCTOR OF PHILOSOPHY

in

The Faculty of Graduate Studies

(Electrical and Computer Engineering)

THE UNIVERSITY OF BRITISH COLUMBIA

(Vancouver)

August 2010

© George Bassem Botros Abadir 2010

Abstract

In this thesis, molecular dynamics and *ab initio* density functional theory/non-equilibrium Green's function simulations are used to study the interaction between carbon nanotubes and amino acids. Firstly, rules for the proper choice of the parameters used in these simulations are established. It is demonstrated how the improper choice of these parameters (particularly the basis set used in *ab initio* simulations) can lead to quantitatively and qualitatively erroneous conclusions regarding the bandgap of the nanotubes. It is then shown that the major forces responsible for amino-acid adsorption on carbon nanotubes are van der Waals forces, and that hydrophobic interactions may accelerate the adsorption process, but are not necessary for it to occur. The mechanisms of interaction between carbon nanotubes and amino acids are elucidated. It is found that geometrical deformations do not play a major role in the sensing process, and that electrostatic interactions represent the major interaction mechanism between the tubes and amino acids. Fully metallic armchair tubes are found to be insensitive to various amino acids, while small-radius nanotubes are shown to be inadequate for sensing in aqueous media, as their response to the motion of the atoms resulting from the immersion in water is comparable to that of an analyte adsorption. Short semi-metallic tubes are revealed to be sensitive to charged amino acids, and it is demonstrated that the conductance changes induced by the adsorption of the analyte in such tubes in a two-terminal configuration are bias-dependent. The effects of the length of the tube and adsorption-site position on the conductance of the tube are discussed. In addition, the adsorption near metallic electrodes is shown to have a negligible effect on the conductance of the tube due to the metal-induced gap states injected from the metal electrodes into the tube. Finally, the results are used to provide general guidelines for the design of carbon-nanotube-based biosensors, as well as to help explaining previously published experimental results.

Table of Contents

Abstract	ii
Table of Contents	iii
List of Tables	vi
List of Figures	vii
Acknowledgements	xiii
Dedication	xiv
1 Introduction	1
1.1 Device Architectures	1
1.1.1 Electrode-Type Sensors	2
1.1.2 FET-Type Sensors	2
1.2 Sensing Mechanisms	3
1.3 Examples of Previous Experimental Work using Carbon Nanotubes as Biosensors	6
1.4 Thesis Objectives	8
1.5 Methodology	10
1.6 Thesis Overview	11
2 Simulation Methods and Models	12
2.1 Molecular Dynamics	12
2.1.1 Models and Parameters	12
2.2 Density Functional Theory/Non-Equilibrium Green's Function Approach	17
2.2.1 Density Functional Theory	18
2.2.2 Open Systems	20
2.2.3 Non-Equilibrium Green's Function and the Electron Density	21

3	Basis-Set Choice for DFT/NEGF Simulations of Carbon Nanotubes	29
3.1	Simulated Structures	29
3.2	SET I	31
3.3	SET II	43
3.4	SET III	44
3.5	Effect of the Electrode Length	45
3.6	Overcompleteness	47
3.7	Conclusion	48
4	Simulation Results	49
4.1	Driving Forces for the Adsorption Process	49
4.1.1	Simulation Flow	49
4.1.2	Results	50
4.2	Metallic Tubes	53
4.2.1	Armchair Tubes	53
4.2.2	Small-Radius Zigzag Tubes	53
4.3	Semi-Metallic Nanotubes	54
4.3.1	Simulated Structures	57
4.3.2	Results and Discussion	59
4.3.3	Effect of Amino-Acid Vibration in Water	71
4.3.4	Repeatability of the Results	72
4.3.5	Effect of the Length of the Nanotube	74
4.3.6	Effect of the Position of the Adsorption Site	76
4.3.7	Connection with Experimental Results and Previously Suggested Sensing Mechanisms in the Literature	78
4.3.8	Conclusion	81
4.4	Metal-Induced Gap States and the Adsorption near Metallic Electrodes	83
4.4.1	Simulation Flow	83
4.4.2	Results	83
4.4.3	Conclusion	84
5	Conclusions	87
5.1	Contributions	87
5.2	Future Work	90
	Bibliography	91

Appendices

A Chemical Structures	103
B Related Publications	105

List of Tables

2.1	Parameter values used in the MD simulations.	15
3.1	Near-zero-bias conductance for the metallic tubes in units of Siemens. The subscript of G designates the corresponding tube.	38
3.2	Computational resources for both the DZ and DZP basis sets used for computing the data in Figure 3.4. Parallel calculations were conducted on a 64-bit, 8-processor (Intel(R), Xeon(TM), 2.66 GHz CPU each) Dell machine.	38
3.3	Computational resources for both the DZ and DZP basis sets used for computing the data in Figure 3.18. Parallel calculations were conducted on a 64-bit, 8-processor (Intel(R) Xeon(TM) 2.66 GHz CPU each) Dell machine.	46
4.1	Different components of the current for the (9,0) and (12,0) tubes with and without the adsorbed dimer of arginine, and at the two bias points 0.01 V and 0.12 V. Currents less than 1 nA were considered to be exactly zero.	67
A.1	Side chains of the different amino acids used in the thesis. . .	104

List of Figures

1.1	FET-type sensors: a) Back-gated, b) Liquid-gated [1] (© Reproduced with permission from Springer Science + Business Media).	3
1.2	Example of amperometric measurements upon successive additions of 2nM of glucose to (a) CNT-based electrode, (b) Glassy carbon electrode [4] (© Reproduced with permission from the Materials Research Society).	5
1.3	(a) Shift of the I-V characteristics (b) Suppression of the drain current [1] (© Reproduced with permission from Springer Science + Business Media).	5
1.4	Setup used in [20] for the detection of PSA (© Reproduced with permission from The Japan Society of Applied Physics).	6
1.5	Results for the PSA detection a) Time-dependent drain current, b) Drain current vs. gate voltage, c) Drain current vs. drain voltage [20] (© Reproduced with permission from The Japan Society of Applied Physics).	7
1.6	Schematic of a biotin-coated CNTFET. Biotin binds tightly to streptavidin molecules and thus sharpens the selectivity towards streptavidin [23] (© Reproduced with permission from the American Chemical Society).	9
1.7	Results with and without streptavidin for a) biotin-coated device, b) bare device [23] (© Reproduced with permission from the American Chemical Society).	9
2.1	Illustration of the Lennard-Jones potential used to describe non-bonded interactions in the MD simulations.	14
2.2	Flowchart for the DFT loop [60] (© Reproduced with permission from Springer Science + Business Media).	19
2.3	Flowchart for the DFT-NEGF loop [60] (© Reproduced with permission from Springer Science + Business Media).	26

3.1	Transmission coefficient vs. energy for the (2,2) tube with different basis sets.	32
3.2	The first transmission eigenstate calculated for the (2,2) tube in units of $\text{\AA}^{(-3/2)}$ at an energy 0.05 eV above the Fermi level, (a) using the DZ basis set, (b) using the DZP basis set. The horizontal white line in the middle denotes the axis of the tube.	33
3.3	Transmission coefficient vs. energy for the (3,3) tube with different basis sets.	34
3.4	Transmission coefficient vs. energy for the (4,4) tube with different basis sets.	34
3.5	Transmission coefficient vs. energy for the (5,5) tube with different basis sets.	35
3.6	Transmission coefficient vs. energy for the (4,0) tube with different basis sets.	35
3.7	Transmission coefficient vs. energy for the (8,0) tube with different basis sets.	36
3.8	Transmission coefficient vs. energy for the (10,0) tube with different basis sets.	36
3.9	Transmission coefficient vs. energy for the (11,0) tube with different basis sets.	37
3.10	Transmission coefficient vs. energy for the (13,0) tube with different basis sets.	37
3.11	Transmission coefficient vs. energy for the (14,0) tube with different basis sets.	38
3.12	Bandgap for the semiconducting $(n,0)$ tubes as calculated using different basis sets vs. the chirality index n	40
3.13	Difference in the calculated bandgap using the SZ, DZ, and SZP basis sets, and that calculated using the DZP basis set for the semiconducting $(n,0)$ tubes vs. the chirality index n	40
3.14	The lowest conduction subband and the top valence subband of the E-k band diagram of graphene calculated using different basis sets. The G, K, and M points are the high-symmetry points Γ , K , and M , respectively. The vertical lines are the cut-lines at which the bandgap of the (10,0), (11,0), (19,0), and (20,0) tubes is calculated according to the zone-folding scheme. Lines to the left of the K point correspond to $(n,0)$ tubes with $n = 3p + 2$, and lines to the right of the K point correspond to $(n,0)$ tubes with $n = 3p + 1$	42

3.15	Difference in the calculated bandgap for the same zigzag tubes shown in Figure 3.13 using the SZ, DZ, and SZP basis sets, and that calculated using the DZP basis set, according to the zone-folding scheme.	42
3.16	Transmission coefficient vs. energy for the (10,0) tube after an MD simulation, and with different basis sets.	43
3.17	Different views for the configuration of the central region of the structure simulated in Set III following a 2 ns MD simulation. The arrows indicate the aromatic rings of the tyrosine dimer.	45
3.18	Transmission coefficient vs. energy for the (10,0) tube with an adsorbed tyrosine dimer after an MD simulation, and with different basis sets.	46
3.19	Transmission coefficient vs. energy for the (5,5) tube with different electrode lengths, and with different basis sets. . . .	47
4.1	Initial configuration of ASN dimers surrounding a (12,11) CNT at a radial distance of 1 nm from the CNT surface. The water molecules in which the dimers and CNT are immersed are omitted for clarity.	50
4.2	Final radial distances between the dimers and the nanotube surface after a 6 ns simulation. (a) (10,0) CNT. (b) (12,11) CNT. The dashed line indicates the initial radial position of the dimers.	51
4.3	Evolution of the VDW-associated potential energies vs. time for ASN and ILE at an initial position of 1.0 nm distance from the tube. (a) (10,0) CNT, (b) (12,11) CNT.	52
4.4	Transmission coefficient for the 2.2 nm (4,0) tube at two different times of the MD simulation.	54
4.5	Displacement of the (5,0)-nanotube atoms for (a) 2.2 nm tube (b) 4.4 nm tube. The displacements in (b) are significantly larger than in (a) and also the differences between the displacements at 1.5 ns and 2 ns in (b) are larger than in (a), indicating larger oscillations.	55
4.6	I-V characteristics of the (5,0) tube both bare and with an adsorbed dimer of arginine for (a) 2.2 nm tube, (b) 4.4 nm tube.	56
4.7	I-V characteristics for the bare (9,0) tube and the same tube with an adsorbed dimer of each of the aromatic amino acids TYR, TRP, and PHE. The vertical line indicates the bias value at which $V = E_G/q$	60

4.8	I-V characteristics for the bare (9,0) tube and the same tube with an adsorbed dimer of each of the neutral non-aromatic amino acids ASN and ILE, and the positively-charged amino acid ARG. The vertical line indicates the bias value at which $V = E_G/q$	61
4.9	I-V characteristics for the bare tubes and for the tubes with an adsorbed dimer of arginine. From left to right, the vertical lines denote the bias value at which $V = E_G/q$ for the (18,0), (15,0), (12,0), and the (9,0) tubes, respectively.	62
4.10	Relative change in the current compared to the current of the bare tubes upon ARG adsorption. From left to right, the vertical lines denote the bias value at which $V = E_G/q$ for the (18,0), (15,0), (12,0), and the (9,0) tubes, respectively. . .	63
4.11	Schematic band diagram for the bare tube for (a) $V = 0$, (b) $0 < V < E_G/q$, and (c) $V > E_G/q$. The dashed lines depict the Fermi level or quasi-Fermi level in each of the contacts. .	65
4.12	Transmission coefficient of the bare (9,0) at two bias points: 0.01 V and 0.12 V.	66
4.13	Schematic band diagram illustrating the effect of the adsorption of ARG on the electrostatic potential energy in the CNT for $V > E_G/q$	66
4.14	Difference in the electrostatic potential in the central region between CNT-ARG and CNT-ARG-bare on one hand, and CNT-bare on the other hand. The difference is shown in (b) along the line shown in (a). The ellipses in (a) denote the guanidino groups.	69
4.15	LDOS at an energy of 0.0 eV, and a bias of 0.12 V, in units of $\text{\AA}^{-3} \text{eV}^{-1}$ on a cut-plane perpendicular to the transport direction at the line shown in (a) for (b) bare tube, (c) tube with adsorbed arginine.	70
4.16	I-V characteristics for CNT-ARG-bare, CNT-ASN-bare, CNT-ILE-bare. The results for CNT-ARG, CNT-ASN, CNT-ILE, and CNT-bare are also included for comparison.	72
4.17	I-V characteristics for (12,0) tube with an adsorbed dimer of arginine at different times of the MD simulation.	73
4.18	The relative change in the current for the (12,0) tube with an adsorbed dimer of arginine at different times of the MD simulation, compared to the bare-tube current.	73

4.19 I-V characteristics for (12,0) tube with an adsorbed dimer of arginine at different times of the MD simulation with an initial separation of 0.7 nm between the dimer and the surface of the tube.	74
4.20 The relative change in the current for the (12,0) tube with an adsorbed dimer of arginine at different times of the MD simulation, and with an initial separation of 0.7 nm between the dimer and the surface of the tube, compared to the bare-tube current.	75
4.21 I-V characteristics for the 8.8 nm (12,0) tube with an adsorbed dimer of arginine at different times of the MD simulation with an initial separation of 0.5 nm between the dimer and the surface of the tube.	76
4.22 The relative change in the current for the 8.8 nm (12,0) tube with an adsorbed dimer of arginine at different times of the MD simulation with an initial separation of 0.5 nm between the dimer and the surface of the tube. The dotted line show the relative difference compared to the bare-tube current at 1.5 ns, while the continuous lines show the relative difference compared to the bare-tube current at 2 ns	77
4.23 I-V characteristics for the 8.8 nm (9,0) bare tube at different times showing larger fluctuations than with the shorter tube.	77
4.24 8.8 nm (9,0) tube with an arginine dimer adsorbed (a) near one of the electrodes, (b) near the middle of the tube.	78
4.25 I-V characteristics corresponding to the simulated structures shown in Figure 4.24.	79
4.26 Band diagram illustrating the cases of adsorption near the electrode (green dotted line) and near the middle of the tube (red line). The black line shows the case for the bare tube.	79
4.27 Band diagram illustrating the effect of the position of the adsorption site on the response of the nanotube in the region before the onset of the tunneling current. The red lines show the disturbance in potential energy due to the presence of a charged species near the surface of the tube.	80
4.28 Band diagram showing the effect of the presence of a localized charge centre near the surface of a nanotube acting as a CNTFET channel, (a) $V_G < V_D/2$, (b) $V_G > V_D/2$. The red lines show the disturbance in potential energy due to the localized charge centre.	82
4.29 Simulated structure showing a molecule of asparagine.	84

List of Figures

4.30	Transmission coefficient (T) as a function of energy (E) at equilibrium.	85
4.31	I-V characteristics for the simulated structures. The results for ILE were very close to the bare-tube case and were omitted for clarity.	85
4.32	Simulation box with smaller dimensions.	86
4.33	I-V characteristics for the simulated structures using a small simulation box. Erroneous results of asparagine are obtained showing the importance of the proper choice of the simulation box dimensions.	86

Acknowledgements

I would like to thank my parents who supported me in this research in more ways than I can mention. I would also like to thank my colleagues for the fruitful discussions and support, especially Ali Mahmoudzadeh and Faizal Karim. I would like to thank Dr. Anders Blom from Quantumwise, the company providing the *ab initio* simulator used in this thesis, for his continuous support throughout this research. Finally, I feel very privileged to have worked under the supervision of Prof. David Pulfrey and Dr. Konrad Walus, with their collegial way of supervision and extreme care for details that unquestionably added much value to this work.

Dedication

To my father...

Chapter 1

Introduction

The detection of biomaterials is of central importance to the diagnosis and treatment of genetic diseases, to the detection of infectious agents, drug discovery, or warning against bio-warfare agents [1]. Therefore, the development of accurate and fast biosensors has become an indispensable need in today's medicine. Carbon nanotubes (CNTs) have a high potential to offer specific advantages in the field of biosensing. Firstly, their size is in the nanometer range, which is compatible with the size of proteins, DNA chains and living cells, making them more suitable as implantable sensors than the larger (and more power-consuming) MEMS sensors [2]. Secondly, in a CNT-field-effect transistor (CNTFET) the current flows on the surface of the nanotube, which is in direct contact with the environment. This, in addition to the high surface-to-volume ratio, gives CNTFET sensors an inherently higher sensitivity than silicon-based sensors [1]. Furthermore, the excellent conducting properties of CNTs and the fact that they can catalyze many electrochemical reactions, allow them to play a vital role in enhancing oxidation-reduction processes that are used in the detection of some biomaterials, *e.g.*, glucose [3]. There is experimental evidence for changes in the conductance of carbon nanotubes upon adsorption of biomolecules (proteins, DNA, glucose), as will be presented in the following section. The exact mechanisms of adsorption and change in conductance are not well understood. This research aims to understand the physical mechanisms of the adsorption of biomolecules on carbon nanotubes as well as the physical mechanisms involved in the change in conductance.

In the following sections, a brief description of the carbon nanotube-based biosensors (CNT-biosensors) presented in the research literature will be presented, and the objectives of the thesis and the methodology used in the research will be outlined.

1.1 Device Architectures

CNT-based biosensors that have been reported in the literature can be broadly divided into two categories: electrode-type sensors and FET-type

sensors.

1.1.1 Electrode-Type Sensors

There are two subcategories for electrode-type sensors:

- Electrodes modified by carbon nanotubes (glassy carbon electrodes (GCE) or metal electrodes). Sensing in this type usually relies on the detection of a certain oxidation process, typically through cyclic, differential-pulse voltammograms or amperometric measurements [4–8]. Bare electrodes suffer from poor sensitivity, low-stability, low-reproducibility, and large response time [3]. CNTs can enhance the electron transfer rate and thus decrease the response time and increase the sensitivity. This type is suitable for glucose detection through the oxidation of glucose in the presence of glucose oxidase [9]. It can also be used to detect DNA via the oxidation of guanine [10, 11]. The guanine on a bare GCE could not be oxidized but electron transfer occurred in the presence of a single-walled nanotube (SWNT) coating.
- CNT-based electrodes, either bare or modified by metallic nanoparticles [3]. The metallic nanoparticles are highly catalytic and can increase the sensitivity to a specific analyte. The carbon nanotubes are used as electrodes to benefit from their excellent conductive properties. This type has been specifically used to sense hydrogen peroxide, which is the product of some oxidation processes such as the oxidation of glucose in the presence of the enzyme glucose oxidase [12–14], and can thus be used to detect glucose. In some cases the glucose was directly oxidized by the metal nanoparticle [15].

1.1.2 FET-Type Sensors

This type also can be subdivided into two subcategories [1]:

- Single-tube sensors. In this type a single nanotube connects the source to the drain. This type is highly sensitive, but suffers from substantial variation during fabrication between different devices due to the still poor control over the fabrication process of carbon nanotubes [16].
- Tube-array sensors. In this type the devices have a random array of nanotubes functioning as the conducting channel. This type is less sensitive than the single nanotube type but offers better reproducibility. The FET devices can be alternatively categorized according to

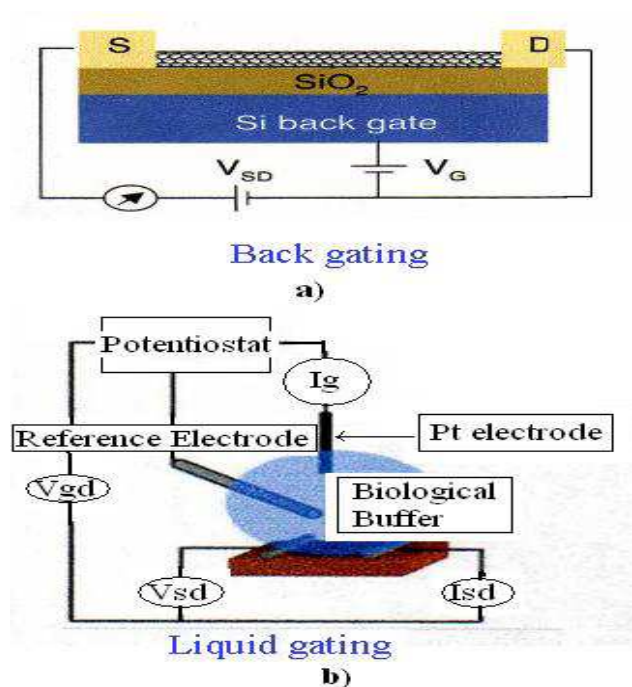


Figure 1.1: FET-type sensors: a) Back-gated, b) Liquid-gated [1] (© Reproduced with permission from Springer Science + Business Media).

their “gating”. One configuration is back gating, where gating is accomplished through a silicon back gate, and the other configuration is liquid gating where gating is accomplished by immersing an electrode in the conducting liquid that surrounds the network and the source and drain electrodes. It has to be noted that in the latter configuration the pH of the biological buffer affects the device characteristics. Both configurations are shown in Figure 1.1.

1.2 Sensing Mechanisms

The main sensing mechanism for the electrode-type sensors is proposed to be the detection of an oxidation-reduction process. For example, as mentioned above, cyclic, differential pulse voltammograms, and amperometric measurements of the oxidation currents are used to detect the oxidation of glucose in the presence of glucose oxidase. An example of the results of such

a measurement is shown in Figure 1.2. The CNTs in this type act as molecular wires to allow electrical communication between the underlying electrode and a redox enzyme to catalyze the redox process [17]. In other words, this type does not exploit changes in the CNT properties due to interaction with the analytes. As for CNTFETs, the mechanism is in general the detection of a change in a device characteristic, most often a change in the I-V characteristics. This change can be induced by either the direct interaction between the target biomolecule and the CNT (as in the case of proteins), or by indirect interaction. An example of the latter is the detection of DNA through hybridization: the nanotube is functionalized by a single-stranded DNA (ssDNA), and when this one hybridizes with its complement to form a double-stranded DNA (dsDNA) a change in the I-V characteristics is observed [18]. Broadly speaking, the I-V characteristics can be altered in two different ways [1]. In one case, the characteristics are totally shifted towards more positive or negative gate voltages indicating electron donation or hole donation, respectively. In other words this shifting indicates charge transfer between the analyte and the nanotube. However, there is some dispute over this explanation. In some works in the literature, it is suggested that the change of the Schottky-barrier height that exists at the interface between the nanotube and metallic electrodes is the correct explanation of this shift [18–20]. Indeed, experiments have been carried out where binding of the target biomolecules was restricted to the source and drain electrodes and showed similar results. These results support the explanation that the modulation of the Schottky-barrier height is the reason behind the changes in the characteristics. Another suggestion is that the biomolecules have an electrostatic gating effect on the nanotube [21–23]. Some experimental results, however, contradict this explanation [20]. The I-V characteristics can be altered in yet another way; the current can be suppressed without being shifted. This may be explained by the introduction of scattering sites by the biomolecule, through either mechanical or electrostatic interactions. The two ways of device-characteristics change are illustrated in Figure 1.3. Another way of biomolecule sensing, though much less frequently mentioned in the literature, is to detect the changes in the optical properties of carbon nanotubes upon adsorption of biomolecules [24].

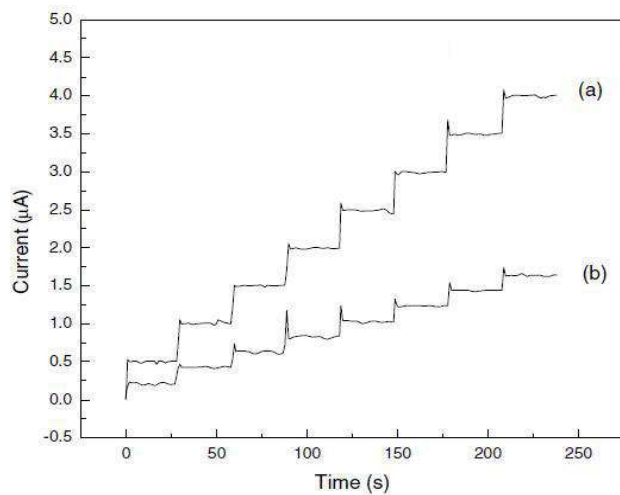


Figure 1.2: Example of amperometric measurements upon successive additions of 2nM of glucose to (a) CNT-based electrode, (b) Glassy carbon electrode [4] (© Reproduced with permission from the Materials Research Society).

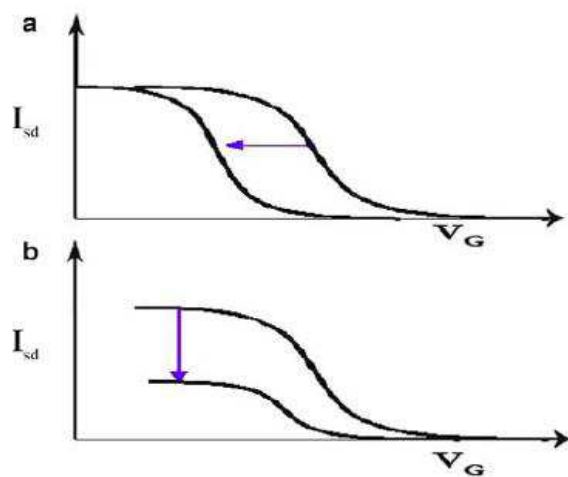


Figure 1.3: (a) Shift of the I-V characteristics (b) Suppression of the drain current [1] (© Reproduced with permission from Springer Science + Business Media).

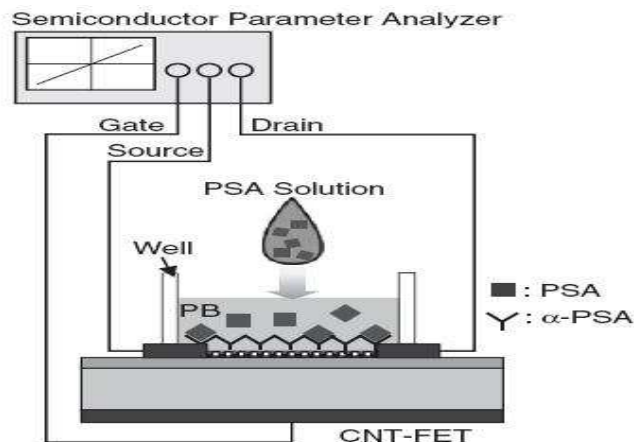


Figure 1.4: Setup used in [20] for the detection of PSA (© Reproduced with permission from The Japan Society of Applied Physics).

1.3 Examples of Previous Experimental Work using Carbon Nanotubes as Biosensors

In this section, two examples will be presented of experimental work in the literature for the use of CNTs as biosensors. As the main focus of this thesis is the detection of proteins and their building blocks, *i.e.*, amino acids, two examples of protein detection will be presented: one using a liquid-gated CNTFET, and the other using a back-gated CNTFET.

In the first example, Kojima *et al.* [20] demonstrated that the pig serum albumin (PSA) could be detected using the setup shown in Figure 1.4. The α -PSA (the antibody of PSA) was immobilized on the nanotube wall and the change in the drain current was monitored as shown. The observed changes in conductance and in the drain current can be seen in Figure 1.5. The authors proposed three possibilities to explain their observations:

- Schottky-barrier height modulation.
- Introduction of scattering sites on the CNT.
- Donation of electrons to the CNT caused by the interaction of the amine groups of the protein and the surface of the CNT.

Similar liquid-gated setups were used in other works to detect bovine serum albumin (BSA) [25], pig serum albumin [26], and prostate-specific antigen [27], to cite a few examples.

1.3. Examples of Previous Experimental Work using Carbon Nanotubes as Biosensors

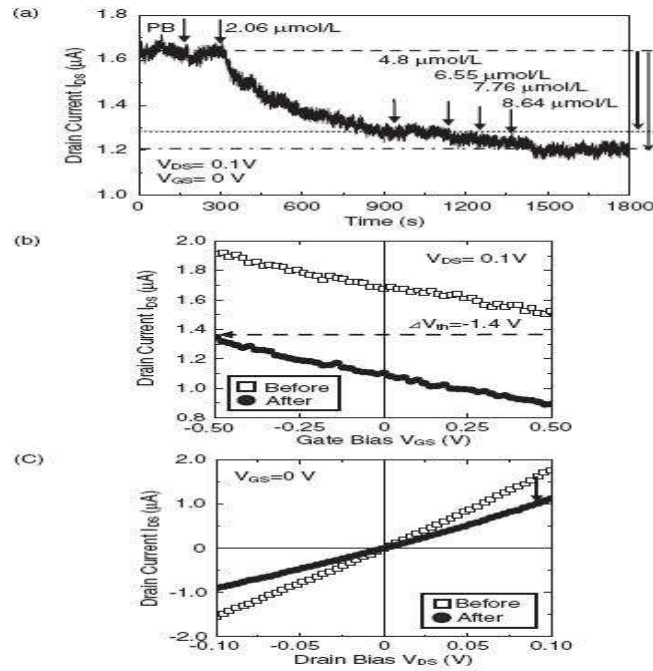


Figure 1.5: Results for the PSA detection a) Time-dependent drain current, b) Drain current vs. gate voltage, c) Drain current vs. drain voltage [20] (© Reproduced with permission from The Japan Society of Applied Physics).

In another work [23], the setup shown in Figure 1.6 was used. The biotin is used to ensure specific binding of streptavidin (the target protein). It is also clear that the sensitivity of the biotin-coated device is enhanced compared to the bare one as shown in Figure 1.7. The authors suggest that the observed change in the I-V characteristics of the bare tube is due to a charge-transfer reaction with streptavidin donating electrons to the nanotube upon nanotube-streptavidin binding [23]. Some other works also support the suggestion of charge transfer between proteins and carbon nanotubes [21, 28–30]. The suppression of the current of the functionalized tube upon streptavidin binding is explained primarily by the occurrence of geometric deformations due to the binding, which introduces scattering sites on the nanotube reducing its conductance. Another possibility suggested by the authors of [23], was the existence of electrostatic interactions leading to the conductance modulation of the nanotube.

Other examples of back-gated CNTFETs used as biosensors include antibody (anti-horseradish peroxidase) and antigen (horseradish peroxidase) binding events detection [31], immunoglobulin-E detection [32], and ruthenium complexes [33], to name a few examples. The same interaction mechanisms mentioned above were also suggested to explain the results in [31] (geometric deformations) and [32] (electrostatic interactions). From the examples above, we see that proteins do affect the conductance of the nanotubes considerably. It is also evident that there is no consensus about the sensing mechanisms, highlighting the lack of a clear understanding of these mechanisms.

1.4 Thesis Objectives

The main objectives of this research are:

- To elucidate the interaction mechanisms between carbon nanotubes and amino acids. Amino acids are chosen as they are the fundamental building blocks of proteins, and because understanding their interaction with CNTs will help to understand how full proteins (which are too complex to be presently simulated by the *ab initio* techniques used in this thesis) interact with CNTs. The simulation approach (as opposed to the experimental approach) offers the ability to calculate the electronic properties of the tube (*e.g.*, local density of states, charge distribution, potential-energy profile, transmission spectrum), offering a better insight into the interaction mechanisms between the tube and the analyte. It also allows the study of structures that are currently

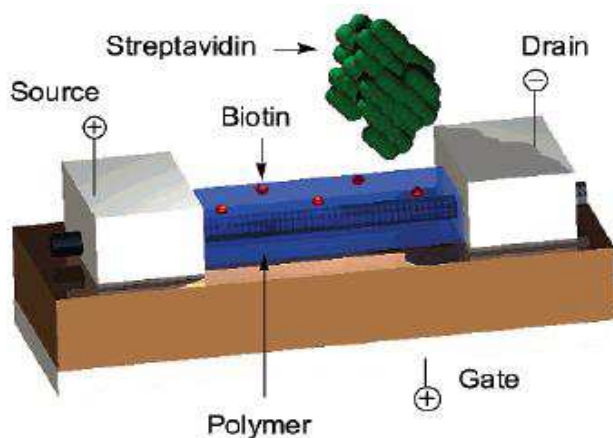


Figure 1.6: Schematic of a biotin-coated CNTFET. Biotin binds tightly to streptavidin molecules and thus sharpens the selectivity towards streptavidin [23] (© Reproduced with permission from the American Chemical Society).

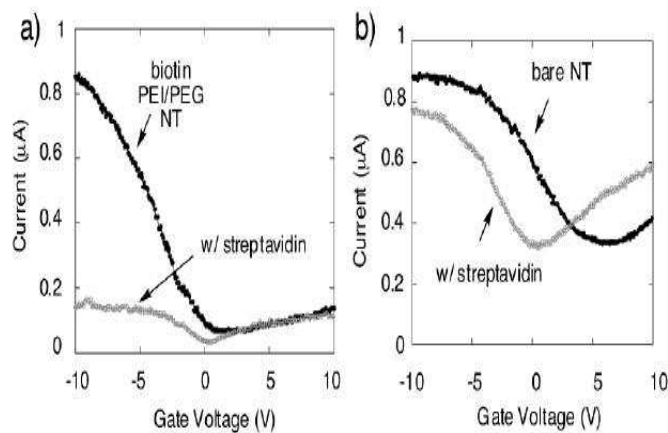


Figure 1.7: Results with and without streptavidin for a) biotin-coated device, b) bare device [23] (© Reproduced with permission from the American Chemical Society).

difficult to fabricate due to technology limitations, but that can be implemented in the future with the advance in technology.

- To use the understanding of the interaction mechanisms to explain the experimental results observed in the literature, and to provide general guidelines for the design of carbon-nanotube-based biosensors.
- To establish rules for the choice of parameters used in the numerical simulations of CNT-biomolecule systems, particularly the basis set used in *ab initio* simulations. This is important since the input parameters of the simulations may lead to non-physical output results that are only artefacts of the poor choice of the input parameters. This will be discussed in detail in Chapter 3, and it will be shown how the lack of such rules has affected previous results in the literature.

1.5 Methodology

To achieve the above-mentioned objectives, molecular dynamics (MD) simulations in combination with *ab initio* density functional theory/non-equilibrium Green's function theory (DFT/NEGF) simulations are used. The MD simulations of the carbon nanotubes and the amino acids in an aqueous medium are conducted to get the positions of the atoms of the carbon nanotubes and those of the amino acids. These positions are then fed to DFT/NEGF simulations to get the effect of the amino-acid adsorption on the electrical conductance of the carbon nanotubes, as well as the relevant physical mechanisms of interaction between the analyte and the nanotube that affect the conductance of the latter. The procedure followed in this research is summarized below:

- Perform classical molecular dynamics (MD) simulations of the CNT with the biomolecules in an aqueous environment to get the coordinates of the atoms of both the tube and the biomolecule in question (*i.e.*, the amino acid).
- Using the coordinates obtained from the MD calculations, simulations based on the DFT/NEGF approach were performed to calculate the changes in the current-voltage characteristics of the tube in a two-terminal configuration, from which the changes in the conductance of the tube can be determined.
- Comparing the bare nanotube properties (local density of states, charge distribution, potential-energy profile, transmission spectrum) to those

of the CNT with the adsorbed biomolecule, the possibility of using carbon nanotubes as molecular-scale sensors can be assessed. The simulations predict which types (metallic, semi-metallic, and semiconducting), and sizes of the tube can be more sensitive, as well as the effect of the position of the adsorption site on the detection of the analyte.

It is worth noting that combining MD and DFT/NEGF simulations for studying CNT-biomolecule interactions has not been performed before to the author's knowledge. The approach allows including the effect of water molecules and van der Waals forces through the molecular dynamics, and also examining the changes in the electronic properties of the tube through the DFT/NEGF simulations. DFT studies have been performed of the interactions between nanotubes and amino acids(*e.g.* [34, 35]), though the effect of water molecules has not been included in these calculations.

1.6 Thesis Overview

The thesis is divided into five chapters. In the first chapter (this chapter), an introduction to the thesis is provided and the general methodology is explained. In Chapter 2, the simulation methods used in the thesis are explained. In Chapter 3, the rules of the choice of the basis set used in DFT/NEGF simulations are presented. In Chapter 4, the results of the simulations are presented and discussed. In Chapter 5, the conclusions and contributions made are summarized.

Chapter 2

Simulation Methods and Models

2.1 Molecular Dynamics

In classical molecular dynamics (MD), atoms are given initial positions and velocities, and then forces on each particle are calculated by considering the influence of each of its neighbours. The Newtonian equations of motion are used to calculate the trajectories by allowing the particles to move under a constant force for a short time interval and then by recalculating a new force to apply for the next short time interval [36]. For a system of N interacting particles

$$m_i \frac{\partial^2 \mathbf{r}_i}{\partial t^2} = \mathbf{F}_i, i = 1, 2, 3, \dots, N, \quad (2.1)$$

where m is the mass of the particle, \mathbf{r}_i its position, \mathbf{F}_i the force acting on the particle, and t is the time.

The force is derived from a potential function (force field) V using

$$\mathbf{F}_i = -\frac{\partial V}{\partial \mathbf{r}_i}. \quad (2.2)$$

The general algorithm to perform MD simulations is as follows:

- Start with input positions and velocities.
- Calculate the forces from the used force field at a given time.
- Calculate the new velocities of the atoms, and deduce their new positions after a small time step (Δt) assuming the forces and velocities are constant over Δt .

2.1.1 Models and Parameters

All the MD simulations in this thesis were performed using the package GROMACS [37]. The main advantage of GROMACS for the purpose of the

work in this thesis is its ability to combine carbon-nanotube systems with biomolecules. In addition, it allows user-defined parameters to be used for the simulations, which is very useful in modeling carbon nanotubes.

Bonds

The bonds in the carbon nanotube were modeled using a Morse potential following the parameters described in [38], and given as

$$U_{bonds} = K_b(\exp(-\gamma(r_{ij} - r_b)) - 1)^2, \quad (2.3)$$

where U_{bonds} is the potential energy associated with the bonds, K_b is a force constant, γ is an empirical parameter, r_{ij} is the instantaneous bond length between atoms i and j , and r_b is the equilibrium bond length. The values of these parameters are summarized in Table 2.1. It is worth noting that, although it can be seen from equation 2.3 that K_b may be regarded as the dissociation energy, *i.e.*, the energy required to break the carbon-carbon bond, the parameter values were actually obtained by fitting to the experimental lattice constants and phonon frequencies of graphite [39]. Therefore, the value of K_b differs from the actual physical dissociation energy of carbon bonds in fullerene systems, which is estimated to be 742.97 kJ/mol [40, 41].

Other force fields that describe carbon nanotubes include the Brenner-Tersoff (BT) model [42, 43], the reactive empirical bond-order (REBO) potential [44, 45], and the adaptive intermolecular reactive empirical bond-order (AIREBO) [46] potential to cite a few examples. The Morse potential (with $r_b = 1.39$ Å) was shown to predict the tensile strength and fracture strain in a closer agreement with the experiments than the results obtained using the REBO potential [47], while the Brenner-Tersoff potential is known to introduce large artificial forces if the bonds are considerably stretched beyond their equilibrium positions [48]. Hence, and since the Morse potential was used during the studies by Werder *et al.* [38, 49, 50] to calibrate the parameters describing the interactions between water molecules and carbon nanotubes (which are important in the case of nanotube-biomolecule studies), this latter potential was chosen to carry out the calculations in this thesis.

Angles

The angles in the carbon nanotubes were maintained through a harmonic cosine potential given as

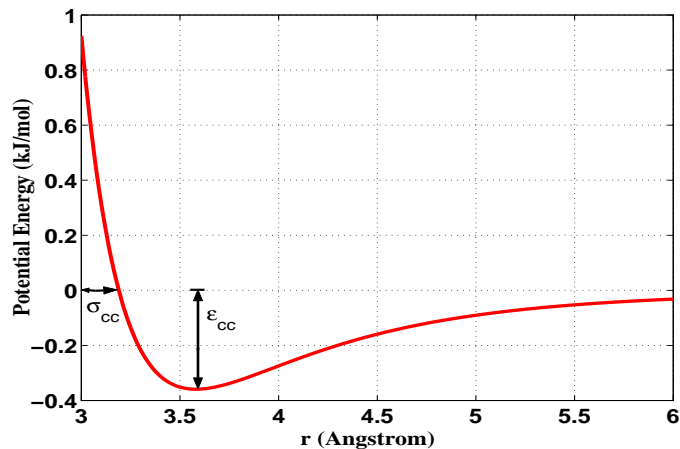


Figure 2.1: Illustration of the Lennard-Jones potential used to describe non-bonded interactions in the MD simulations.

$$U_{angles} = K_{\theta}(\cos(\theta_{ijk}) - \cos(\theta_c))^2, \quad (2.4)$$

where U_{angles} is the potential energy associated with the angles between the atoms, θ_{ijk} is the angle between the line joining atoms i and j , and that joining atoms j and k , K_{θ} is the force constant associated with the force field. θ_c is the equilibrium angle, which is equal to 120° ¹.

Van der Waals Interactions

The van der Waals interactions were modeled through a Lennard-Jones potential as illustrated in Figure 2.1, and formulated as

$$U_{LJ} = 4\epsilon_{cc}\left[\left(\frac{\sigma_{cc}}{r_{ij}}\right)^{12} - \left(\frac{\sigma_{cc}}{r_{ij}}\right)^6\right], \quad (2.5)$$

where ϵ_{cc} represents the depth of the potential well shown in Figure 2.1 and σ_{cc} is the finite distance at which the potential goes to zero.

The biomolecules (amino acids) used were modeled via the AMBER99 port [51] to GROMACS. The AMBER force field and parameters are specifically parametrized for simulating biomolecules in water, and therefore were the most suitable for this work. Since the parametrization of the AMBER99

¹For tubes larger than $\sim 0.9 \text{ nm}$, θ_c is equal to 120° for all angles. For smaller tubes, however, because of warping effects due to the large curvature of the tubes, small deviations from the 120° -value were observed when generating the relaxed-tube coordinates.

Table 2.1: Parameter values used in the MD simulations.

Parameter	Value
K_b	478.9 kJ/mol
r_b	1.42 Å
γ	2.1867 Å ⁻¹
K_θ	562.2 kJ/mol
σ_{cc}	3.431 Å
ϵ_{cc}	0.4396 kJ/mol
σ_{co}	3.19 Å
ϵ_{co}	0.392 kJ/mol

force field was performed in combination with the TIP3P water model [52], this latter was used to describe the water molecules throughout the simulations in this thesis. The TIP3P model is a rigid water model, where the structure of the molecule is fixed throughout the simulation; the bond length between the oxygen and hydrogen atom is 95.84 pm and the $H\hat{O}H$ angle is 104.45°.

The interaction between the carbon nanotube and the water followed a Lennard-Jones potential which has the same form as in equation 2.5:

$$U_{LJ} = 4\epsilon_{co} \left[\left(\frac{\sigma_{co}}{r_{ij}} \right)^{12} - \left(\frac{\sigma_{co}}{r_{ij}} \right)^6 \right], \quad (2.6)$$

with the parameters ϵ_{co} and σ_{co} being taken from [38, 49, 50] and shown in Table 2.1.

Coulomb Interactions

The short-range Coulomb interaction (below a cut-off radius of 1.3 nm in this thesis) between two charged particles i and j is modeled using

$$U_{COUL}(r_{ij}) = \frac{q_i q_j}{4\pi\epsilon r_{ij}}, \quad (2.7)$$

where U_{COUL} is the potential associated with the Coulombic interactions, q_i and q_j are the charges of the two particles, r_{ij} is the distance between the two particles, and ϵ is the permittivity of the medium.

When the long-range interactions are described using Ewald summation [53] or particle-mesh Ewald [54] (used in this thesis), the short-range

interactions are modified to ensure a smooth transition at the cut-off radius, and are expressed as

$$U_{COUL}(r_{ij}) = \frac{\text{erfc}(\beta r_{ij})}{4\pi\epsilon r_{ij}}, \quad (2.8)$$

where β is a constant that determines the relative weight between the direct space sum and the reciprocal space sum used in the Ewald summation schemes.

Run Parameters

Integrator GROMACS uses the leap-frog algorithm [55] to integrate the Newtonian equations of motion. It uses positions \mathbf{r} at a time t and velocities \mathbf{v} at time $(t - \frac{\Delta t}{2})$; it updates positions and velocities using the forces $\mathbf{F}(t)$ determined by the positions at time t using

$$\mathbf{v}(t + \frac{\Delta t}{2}) = \mathbf{v}(t - \frac{\Delta t}{2}) + \frac{\mathbf{F}(t)}{m} \Delta t, \quad (2.9)$$

and

$$\mathbf{r}(t + \Delta t) = \mathbf{r}(t) + \mathbf{v}(t + \frac{\Delta t}{2}) \Delta t. \quad (2.10)$$

The leap-frog scheme is a modification of the Verlet scheme [56]. The error in the positions calculated through the unmodified Verlet scheme is on the order of $(\Delta t)^2$, while the leap-frog scheme results in a global error of the order $(\Delta t)^3$ thus providing more accurate predictions of the positions and velocities of the atoms for the same time step.

Time Step The time step Δt used for integration is of critical importance to the accuracy of MD simulations. A value of Δt that is too large will lead to an unstable system and a drift in the total energy of the system, while a value that is too small will increase the time of the simulation and the size of the output files drastically.

In principle, the time step is governed by the largest oscillation frequency in the system. This is in general associated with the hydrogen atoms in the system. The leap-frog integrator used in GROMACS allows a maximum time step of 3 fs without compromising the accuracy of the simulations [57]. The time step used in the simulations presented in this thesis was 2 fs for all simulations. To ensure the validity of this time step, time steps of smaller values (1 fs, 0.5 fs, and 0.25 fs) were used in pilot simulations and they all resulted in the same (within an change of less than 1%) total, potential,

and kinetic energies as the 2 fs-simulations, as well as the same relative coordinates of the (9,0) and (12,0) tubes and a dimer of the amino acid arginine.

Boundary Conditions The boundary conditions used are periodic boundary conditions (PBC). The advantage of such conditions is to eliminate any artificial boundaries that may arise due to the finite simulation box. The PBC are implemented by positioning the atoms of the system in a space-filling box, which is surrounded by translated copies of itself. The molecules to be simulated (the CNT and the amino acids) were separated from the edge of the simulation box by a distance of 1 nm to minimize the interaction with the nearest image. Slightly larger and slightly smaller separations did not result in any significant change in the MD results, and therefore a separation of 1 nm was adopted for the simulations presented in this thesis.

Temperature Coupling The temperature was kept constant in the MD simulations presented in this thesis through a Berendsen thermostat [58]. The algorithm restores the temperature of the system T to the reference temperature T_0 according to the equation

$$\frac{dT}{dt} = \frac{T - T_0}{\tau}, \quad (2.11)$$

where τ is a time constant. The value of τ should be chosen to be much greater than the integration time step Δt for reliable results. The value of τ used throughout the simulations was 0.1 ps, which is 50 times greater than Δt .

2.2 Density Functional Theory/Non-Equilibrium Green's Function Approach

In this section, the Density functional theory/Non-equilibrium Green's function (DFT/NEGF) approach used in this thesis to simulate the effect of biomolecule adsorption on the nanotubes is described. First the DFT for modeling molecular structures within the Kohn-Sham equations [59] is described, and then the use of the NEGF to solve the DFT equations for a molecular system coupled to external electrodes is explained. This section is largely based on [60].

2.2.1 Density Functional Theory

The purpose of DFT is to calculate the properties of a molecular system based on a description of the positions and species of the individual atoms in the system. The atoms comprise an ionic core surrounded by a cloud of electrons that balance the charge of the ionic core. In the following, \mathbf{R}_μ and Z_μ are used to denote the ionic positions and charges, respectively, where $\mu = 1, 2, 3 \dots N$ and N is the number of ions. The positions of the electrons will be denoted \mathbf{r}_i , where $i = 1, 2, 3 \dots n$ with n being the number of electrons. The nuclei are assumed to be classical stationary particles, and their potential energy $V(\mathbf{R}_1, \dots, \mathbf{R}_N)$ is described according to the following equation:

$$V(\mathbf{R}_1, \dots, \mathbf{R}_N) = E_0 + \frac{1}{2} \sum_{\mu, \mu'=1}^N \frac{Z_\mu Z_{\mu'} e^2}{|\mathbf{R}_\mu - \mathbf{R}_{\mu'}|}, \quad (2.12)$$

where E_0 is the energy of the electronic system. The electrons are described as quantum mechanical particles, and the calculation of their energy E_0 is performed by solving Schrödinger's equation:

$$\hat{H} = - \sum_{i=1}^n \frac{\hbar^2}{2m} \nabla_i^2 - \sum_{i=1}^n \sum_{\mu=1}^N \frac{Z_\mu e^2}{|\mathbf{r}_i - \mathbf{R}_\mu|} + \frac{1}{2} \sum_{i,j=1}^n \frac{+e^2}{|\mathbf{r}_i - \mathbf{r}_j|}, \quad (2.13)$$

where $\hat{H}\Psi(\mathbf{r}_1, \dots, \mathbf{r}_n) = E_0\Psi(\mathbf{r}_1, \dots, \mathbf{r}_n)$ is the Hamiltonian operator and Ψ is the wavefunction of the electrons. The first term on the right-hand side describes the kinetic energy of the electrons, the second term describes the ion-electron electrostatic interaction, and the last one describes the electron-electron electrostatic repulsion. The problem described above is a many-body problem, which is very complicated to solve. The DFT transforms the many-body problem into an effective one-electron equation. The electrons are assumed to be non-interacting particles moving in an effective potential set by the other electrons. The DFT equations are

$$\hat{H}_{1el} = -\frac{\hbar}{2m} \nabla^2 + V_{eff}[n](\mathbf{r}), \quad (2.14)$$

$$\hat{H}_{1el}\psi_\alpha = \varepsilon_\alpha\psi_\alpha, \quad (2.15)$$

and

$$n(\mathbf{r}) = \sum |\psi_\alpha(\mathbf{r})|^2 F(\varepsilon - \mu_F). \quad (2.16)$$

Here, \hat{H}_{1el} is the one-electron Hamiltonian, $V_{eff}[n](\mathbf{r})$ is the effective potential of the electron as a functional of the electron density. The one-electron

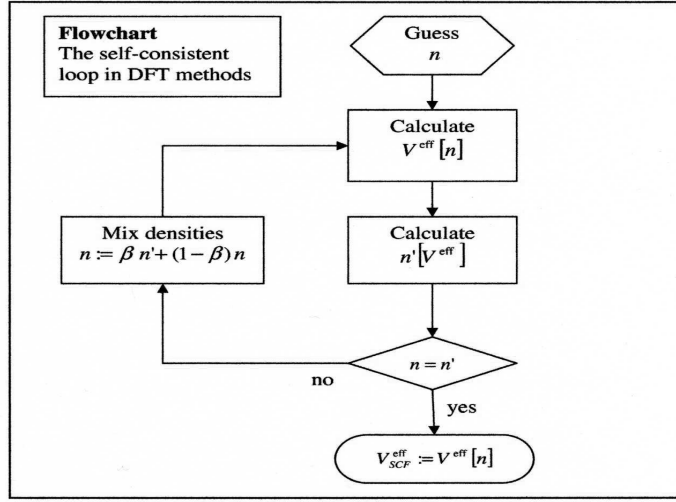


Figure 2.2: Flowchart for the DFT loop [60] (© Reproduced with permission from Springer Science + Business Media).

eigenstates ψ_α can be determined from equation 2.15. The electron density is then calculated through equation 2.16 where μ_F is the chemical potential and $F(\varepsilon - \mu_F)$ is the Fermi distribution function. The DFT loop is summarized in the flow chart shown in Figure 2.2.

The effective potential in DFT is divided into three parts, ionic potential V^{ion} , Hartree potential V^H , and the exchange and correlation potential V^{xc} :

$$V_{eff}[n] = V^{ion} + V^H[n] + V^{xc}[n], \quad (2.17)$$

where

$$V^{ion}(\mathbf{r}) = \sum_{\mu=1}^N \frac{Z_\mu e^2}{|\mathbf{r} - \mathbf{R}_\mu|}, \quad (2.18)$$

$$\nabla^2 V^H[n](\mathbf{r}) = -4\pi n(\mathbf{r}), \quad (2.19)$$

and

$$V^{xc}(\mathbf{r}) = f(n(\mathbf{r}), \nabla n(\mathbf{r}), \nabla^2 n(\mathbf{r})). \quad (2.20)$$

The ionic potential is the electrostatic potential from the ion cores. The Hartree potential is the potential associated with the electronic charge and is calculated from Poisson's equation. The exchange and correlation potential can be qualitatively understood as follows: the exchange part is the

difference in the energy of the system when two electrons swap their coordinates. It means that an electron of a given spin will be surrounded by a region where the density of electrons with the same spin is reduced (Pauli exclusion principle) [61]. As for the correlation part, it is the difference between the energy calculated using the Hartree-Fock approximation [62], and the actual energy of the system. It arises from the fact that, within the Hartree-Fock method, electrons are assumed to move independently; that the probability of finding an electron at a certain position \mathbf{r}_1 is not affected by the probability of finding another electron at another position \mathbf{r}_2 except through the Pauli exclusion principle. In other words, it assumes that electrons are not “correlated”, hence the name “correlation energy”. The correlation energy involves corrections to both the kinetic and potential energies of the electron. There are several functionals used to describe the exchange and correlation potential. In this thesis, the local density approximation (LDA) [63] (V^{xc} is only a functional of the density itself) is used as it has been shown to correctly reproduce the experimental results of the geometry, the bond lengths, energies, and electronic structures of graphitic and sp^2 -like systems [64–71].

2.2.2 Open Systems

The scheme above can be solved for isolated systems (*i.e.*, single molecules), or periodic (bulk) structures. An electronic device is neither a single molecule, nor a periodic structure. However, it can be divided into a molecular region, and two electrodes which can be assumed to be semi-infinite and therefore periodic. The molecular region can exchange particles with the semi-infinite electrodes, hence the system is called an “open system”. The potential in the electrodes is thus assumed to be bulk-like. The interaction region between the two electrodes consists of the molecular device in question in addition to a few layers of the electrodes (screening layer), where all charge non-neutrality and band bending due to the interaction between the molecular device and the electrodes are confined. This is referred to as the “screening approximation”. Each electrode injects traveling states into the central region, where for each energy ε we have a right-to-left traveling wave $\psi_{kRL}(\varepsilon)$ and a left-to-right traveling wave $\psi_{kLR}(\varepsilon)$ each with a crystal momentum $\hbar k$. These states are labeled “scattering states” because, in principle, they exhibit scattering and reflections in the central region. The scattering states can be calculated by determining the Bloch waves for the left and right electrodes, and then using these as matching boundary conditions for the central

region. The electron density is then determined using

$$n(\mathbf{r}) = \sum_{k_L, k_R} [|\psi_{k_{LR}}|^2 F(\varepsilon_{k_L} - \mu_{FL}) + |\psi_{k_{RL}}|^2 F(\varepsilon_{k_R} - \mu_{FR})], \quad (2.21)$$

where μ_{FL} and μ_{FR} are the Fermi levels in the left and right electrodes, respectively.

The wavefunctions $\psi(\mathbf{r})$ are expanded as a linear combination of basis functions ϕ_i : $\psi(\mathbf{r}) = \sum_i a_i \phi_i(\mathbf{r})$ (a more detailed discussion of the basis sets will be provided at the end of this chapter). Therefore, 2.15 is transformed into

$$\sum_j H_{ij} a_j = \varepsilon \sum_j S_{ij} a_j, \quad (2.22)$$

where $H_{ij} = \langle \phi_i | \hat{H}_{1el} | \phi_j \rangle$, and $S_{ij} = \langle \phi_i | \phi_j \rangle$. For a finite Hamiltonian, the solution of the above equations is possible. For an open system, however, the Hamiltonian in general is not finite. This is the reason behind dividing the system into three separate regions as mentioned above. For the finite central interaction region, the Hamiltonian is obviously finite. For the two electrodes, by assuming they are periodic, only one period is needed to be considered, and therefore the Hamiltonian of the electrodes is also finite. The total Hamiltonian of the system \bar{H} is thus expressed in terms of the Hamiltonians of the electrodes and the interaction region as follows:

$$\bar{H} = \begin{pmatrix} \bar{H}_{LL} & \bar{H}_{LI} & 0 \\ \bar{H}_{IL} & \bar{H}_{II} & \bar{H}_{IR} \\ 0 & \bar{H}_{RI} & \bar{H}_{RR} \end{pmatrix}. \quad (2.23)$$

where \bar{H}_{LL} , \bar{H}_{RR} , and \bar{H}_{II} are the matrix elements for the left electrode, right electrode, and the interaction region respectively, and \bar{H}_{LI} , \bar{H}_{RI} , \bar{H}_{IL} and \bar{H}_{IR} are the matrix elements involving the interaction between the central region and the electrodes. The bars indicate that each element is a matrix. The scattering states described above are simply the eigenstates of the Hamiltonian above. In the following subsection, the use of the non-equilibrium Green's function formalism to calculate the electron density is explained.

2.2.3 Non-Equilibrium Green's Function and the Electron Density

The retarded Green's function is defined as

$$\hat{G}(\varepsilon) = \frac{1}{\varepsilon - \hat{H} + i\delta_+}, \quad (2.24)$$

where δ_+ is an infinitesimal positive number. From the theory of complex functions, we have

$$\text{Im} \frac{1}{x + i\delta_+} = -\pi\delta(x). \quad (2.25)$$

Comparing to 2.24, we have

$$\text{Im}(\hat{G}(\varepsilon)) = -\pi\delta(\varepsilon - \hat{H}). \quad (2.26)$$

Now let us consider the electron density. If, for the sake of illustration, we take the set of eigenstates ψ_α as our basis set, then the electron density can be calculated as

$$n(\mathbf{r}) = \sum_{\alpha} |\psi_{\alpha}(\mathbf{r})|^2 F(\varepsilon_{\alpha} - \mu_F), \quad (2.27)$$

$$\implies n(\mathbf{r}) = \sum_{\alpha} \int_{-\infty}^{\infty} |\psi_{\alpha}(\mathbf{r})|^2 \delta(\varepsilon - \varepsilon_{\alpha}) F(\varepsilon - \mu_F) d\varepsilon. \quad (2.28)$$

Since we have $\hat{H}\varepsilon = \psi\varepsilon$, and $|\psi_{\alpha}(\mathbf{r})|^2 = \psi_{\alpha}(\mathbf{r})^* \psi_{\alpha}(\mathbf{r})$, we have

$$n(\mathbf{r}) = \sum_{\alpha} \int_{-\infty}^{\infty} \psi_{\alpha}(\mathbf{r})^* \delta(\varepsilon - \hat{H}) \psi_{\alpha}(\mathbf{r}) F(\varepsilon - \mu_F) d\varepsilon. \quad (2.29)$$

By defining the spectral density operator $\hat{\rho}(\varepsilon)$ as

$$\hat{\rho}(\varepsilon) = \delta(\varepsilon - \hat{H}), \quad (2.30)$$

and the density matrix \hat{D} as

$$\hat{D} = \int_{-\infty}^{\infty} \hat{\rho}(\varepsilon) F(\varepsilon - \mu_F) d\varepsilon, \quad (2.31)$$

we get

$$n(\mathbf{r}) = \text{Tr} \hat{D}. \quad (2.32)$$

From the definition of the spectral density operator, we can see that

$$\hat{\rho} = -\frac{1}{\pi} \text{Im} \hat{G}(\varepsilon). \quad (2.33)$$

By expanding the operators using the basis functions, 2.24, 2.30, 2.31, and 2.33 become

$$\overline{G} = [(\varepsilon + i\delta_+) \overline{S} - \overline{H}]^{-1}, \quad (2.34)$$

$$\overline{\rho}(\varepsilon) = -\frac{1}{\pi} \text{Im} \overline{G}(\varepsilon), \quad (2.35)$$

$$\overline{D} = \int_{-\infty}^{\infty} \overline{\rho}(\varepsilon) F(\varepsilon - \mu_F) d\varepsilon, \quad (2.36)$$

and

$$n(\mathbf{r}) = \sum_{i,j} D_{ij} \phi_i^*(\mathbf{r}) \phi_j(\mathbf{r}). \quad (2.37)$$

The Hamiltonian of each block \overline{H}_{ii} , and the interaction Hamiltonians \overline{H}_{ij} can be calculated from a bulk calculation of the electrode, *i.e.*, the calculation of an infinite, perfectly periodic electrode. Using recursion, we obtain

$$\begin{aligned}\overline{G}_{L_1L_1}^{0[0]} &= [(\varepsilon + i\delta_+)\overline{S}_{L_1L_1} - \overline{H}_{L_1L_1}]^{(-1)}, \\ \overline{G}_{L_1L_1}^{0[1]} &= [(\varepsilon + i\delta_+)\overline{S}_{L_1L_1} - \overline{H}_{L_1L_1} - \overline{H}_{L_1L_2}\overline{G}_{L_2L_2}^{0[0]}\overline{H}_{L_2L_1}]^{(-1)}, \\ \overline{G}_{L_1L_1}^{0[2]} &= [(\varepsilon + i\delta_+)\overline{S}_{L_1L_1} - \overline{H}_{L_1L_1} - \overline{H}_{L_1L_2}\overline{G}_{L_2L_2}^{0[1]}\overline{H}_{L_2L_1}]^{(-1)}, \\ &\vdots \\ &\vdots \\ &\vdots\end{aligned}\quad (2.42)$$

where the superscript $[n]$ refers to the order of the approximation. Now, from equation 2.38, G_I can be obtained, and from that the electron density can be obtained through

$$n(r) = \sum_{i,j} D_{ij} \phi_i(r) \phi_j(j), \quad (2.43)$$

where

$$D_{ij} = \int_{-\infty}^{\mu_F} -\frac{1}{\pi} \text{Im} G_{ij}(\varepsilon) F(\varepsilon - \mu_F) d\varepsilon. \quad (2.44)$$

Finite Bias

Now, let us consider the case where a finite non-zero bias is applied, *i.e.*, the Fermi levels in the two electrodes are no longer the same, and they are related to the applied bias V_b through

$$qV_b = \mu_{FR} - \mu_{FL}. \quad (2.45)$$

The carrier density can be attributed to separate contributions from the left and right electrodes:

$$\hat{\rho} = \hat{\rho}^L(\varepsilon) + \hat{\rho}^R(\varepsilon). \quad (2.46)$$

The density matrix for non-equilibrium is given by

$$\hat{D} = \int_{-\infty}^{\infty} \hat{\rho}^L(\varepsilon) F(\varepsilon - \mu_{FL}) + \hat{\rho}^R(\varepsilon) F(\varepsilon - \mu_{FR}) d\varepsilon. \quad (2.47)$$

The partial spectral densities are calculated as [73]

$$\hat{\rho}^L(\varepsilon) = -\hat{G}(\varepsilon) \text{Im} \hat{\Sigma}^L(\varepsilon) \hat{G}^\dagger(\varepsilon), \quad (2.48)$$

and

$$\hat{\rho}^R(\varepsilon) = -\hat{G}(\varepsilon)\text{Im}\hat{\Sigma}^R(\varepsilon)\hat{G}^\dagger(\varepsilon) \quad (2.49)$$

The density matrix, assuming that $\mu_{FL} < \mu_{FR}$, is thus given by

$$\hat{D} = \int_{-\infty}^{\infty} \hat{\rho}(\varepsilon)F(\varepsilon - \mu_{FL}) + \hat{\rho}^R(\varepsilon)[F(\varepsilon - \mu_{FR}) - F(\varepsilon - \mu_{FL})]d\varepsilon. \quad (2.50)$$

The first term of the integral is nothing other than the equilibrium density matrix, while the second term is the non-equilibrium density matrix due to the applied bias.

Now, knowing the carrier density, the effective potential can be calculated using equations 2.17 through 2.20. The current can then be calculated using the Landauer formula for coherent transport in a two-terminal nanoscale device [60]

$$I = \frac{2e}{h} \int_{-\infty}^{\infty} T(\varepsilon)[F(\varepsilon - \mu_{FL}) - F(\varepsilon - \mu_{FR})]d\varepsilon. \quad (2.51)$$

$T(\varepsilon)$ is the transmission coefficient which is the sum of the net probabilities of electrons traveling from the higher-Fermi-level electrode to the lower-Fermi-level-electrode. It can be calculated from the NEGF theory [74] as

$$T(\varepsilon) = \text{Tr} \left\{ \text{Im}\hat{\Sigma}_L(\varepsilon)\hat{G}^\dagger(\varepsilon)\text{Im}\hat{\Sigma}_R(\varepsilon)\hat{G}(\varepsilon) \right\}. \quad (2.52)$$

The complete loop for the DFT/NEGF scheme is illustrated in Figure 2.3.

Basis Sets

The basis sets (ϕ_i above) are one of the most important parameters in DFT calculations. The basis sets used in the two-terminal calculations described above need to be localized (as opposed to plane-wave basis sets) in order to ensure reasonable time and memory requirements, specially for large systems (\sim hundreds of atoms), as the CNT-biomolecule systems studied in this thesis. The minimal representation of orbitals uses only one basis function for each atomic orbital up to and including the valence orbitals. These minimal basis sets are called “single-zeta (SZ)” basis sets. The reason for this nomenclature is historical as the first basis set used in such calculations were Slater-type orbitals (STO) [75] which have the form

$$\phi^{STO} = Nr^{n-1}\exp[-\zeta r]Y_{lm}. \quad (2.53)$$

Here, N is a constant, n, l , and m are the principal, azimuthal, and magnetic quantum numbers, respectively, Y_{lm} are the spherical harmonics describing the angular part of the function, and ζ is the orbital exponent,

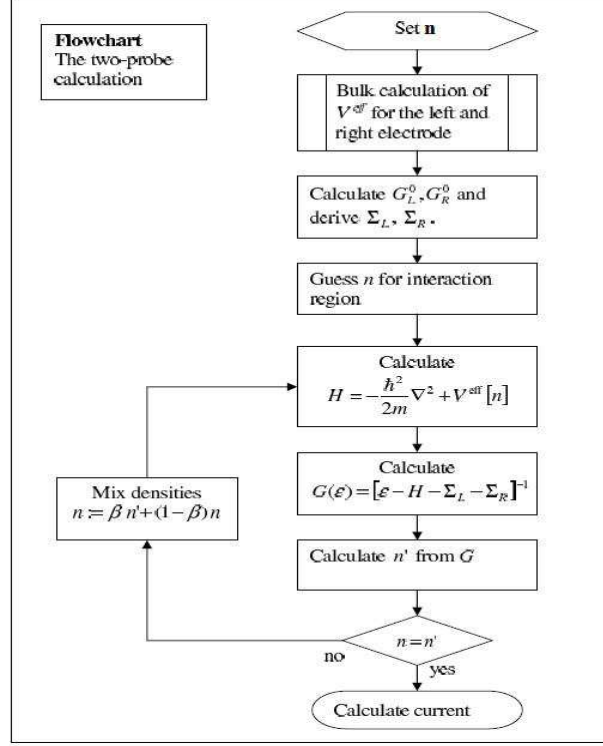


Figure 2.3: Flowchart for the DFT-NEGF loop [60] (© Reproduced with permission from Springer Science + Business Media).

hence the nomenclature. A more complete description of the basis set adds one more function to describe each orbital, and therefore the basis sets are called “double-zeta (DZ)” basis sets. Another addition to the basis sets involves adding *polarization*, *i.e.*, describing the first non-occupied orbital in the atom (*d*-orbitals in carbon atoms for instance). This allows the non-symmetry (*i.e.*, *polarization*) of the orbitals around the atoms to better describe the bonds in a molecule, as opposed to the symmetric orbitals in an isolated atom. The STO basis sets yield difficult overlap integrals. Therefore, Gaussian-type orbitals (GTO) are currently the common basis-set type used in practice. The GTO’s are given as

$$\phi^{GTO} = N x^i y^j z^k \exp[-\alpha r^2], \quad (2.54)$$

where α is the orbital exponent controlling the width of the GTO, and i , j , and k are non-negative integers that dictate the nature of the orbital in

a Cartesian sense. When all three of these indices are zero, the GTO has spherical symmetry, and is called an s-type GTO. When exactly one of the indices is one, the function has axial symmetry about a single Cartesian axis and is called a p-type GTO, and when the sum of the indices is equal to two, the orbital is called a d-type GTO [76]. The STO's, however, are a closer representation of the actual atomic orbitals. To both use the GTO's for their mathematical convenience and get a physically correct orbital, several GTO's are combined together to form a *contracted Gaussian function* (CGF) that is closer to an STO than a single primitive GTO:

$$\phi_{\tau}^{CGF} = \sum_a^A d_{a\tau} \phi_a^{GTO}. \quad (2.55)$$

Usually 3 to 6 primitive GTO's are taken ($A = 3 - 6$). The contraction coefficients $d_{a\tau}$ are chosen so that the contracted Gaussian functional resembles as much as possible a single STO function.

Considering the fact that only the valence electrons can contribute to the electrical current, the calculations can be simplified by using pseudopotentials to describe the core electrons. The pseudopotentials are described following [77]. The basis sets used in the DFT/NEGF simulator used in this thesis (Atomistix [78]) are described in [79]. The SZ basis set is calculated as the eigenfunctions of the atom in a spherical box, where the radius of the box may be different for different orbitals. The basis functions in this case are the numerical eigenfunctions $\phi_l(\mathbf{r})$ of the atomic potential $V_l(\mathbf{r})$, for an energy $\varepsilon + \delta\varepsilon$ chosen such that the first node occurs at a cut-off radius r_{lc} ($\phi_l(\mathbf{r}_{lc}) = 0$):

$$\left(-\frac{1}{2r} \frac{d^2}{dr^2} r + \frac{l(l+1)}{2r^2} + V_l(\mathbf{r})\right) \phi_l(\mathbf{r}) = (\varepsilon_l + \delta\varepsilon_l) \phi_l(\mathbf{r}). \quad (2.56)$$

For DZ basis sets, the first- ζ basis orbitals are usually CGF's, while the second one is the slowest-decaying GTO of those CGF's. Following the same spirit, the second- ζ orbitals $\phi_l^{2\zeta}(\mathbf{r})$ in Atomistix have the same tail as the first- ζ orbitals $\phi_l^{1\zeta}(\mathbf{r})$ outside a chosen "split-radius" (r_l^s), while they are given by a simple polynomial inside r_l^s :

$$\phi_l^{2\zeta}(\mathbf{r}) = \begin{cases} r^l(a_l - b_l r^2) & r < r_l^s \\ \phi_l^{1\zeta}(\mathbf{r}) & r \geq r_l^s \end{cases} \quad (2.57)$$

The constants a_l and b_l are determined from the continuity of the wavefunction and its derivative, and r^l is the orbital radius.

2.2. *Density Functional Theory/Non-Equilibrium Green's Function Approach*

Finally, the inclusion of polarization is achieved by applying a small electric field in the z-direction and applying the first-order perturbation theory. The complete details can be found in [79].

Chapter 3

Basis-Set Choice for DFT/NEGF Simulations of Carbon Nanotubes

In this chapter, some general rules that were established during this research for the choice of the basis set of DFT/NEGF simulations of carbon nanotubes [80] are presented. The effect of the basis set on the results of *ab initio* calculations of the bandgap and near-zero-bias conductance of carbon nanotubes is discussed. The near-zero-bias conductance is used to assess the accuracy of the basis sets for the simulation of metallic nanotubes which have a zero-bandgap; and the bandgap is used to assess the accuracy of the basis sets for semiconducting tubes which have a very small near-zero-bias conductance (\sim pS - nS). Firstly, several ideal nanotubes with different chiralities are studied. The effect of small displacements in the atomic positions on the choice of the basis set is then studied. Finally, the effect of the addition of an adsorbed biomolecule on the choice of the basis set is examined. The simulations were performed using the DFT/NEGF approach, within the local density approximation (LDA) [63], employing the Atomistix [78] package described in [60].

3.1 Simulated Structures

The simulations are divided into three different sets. The first set (SET I) is for perfect nanotubes of different chiralities. The second set (SET II) is for a (10,0) tube with the positions of its atoms having been displaced due to immersion in water. The coordinates of the atoms are determined from a molecular dynamics (MD) simulation of the nanotube in water using the package GROMACS. The third set of simulations (SET III) is for a (10,0) nanotube with an adsorbed dimer of the aromatic amino acid tyrosine, with the coordinates of the tube and tyrosine also determined from MD simulations in water. Tyrosine was used due to the previous knowledge that

it does adsorb on the surface of nanotubes [34], and a dimer configuration was chosen to simulate the existence of a peptide bond as expected in full proteins.

For SET I, the simulated structures consisted of a central region of four periods (eight layers of atoms) of each of the armchair tubes: (2,2), (3,3), (4,4), and (5,5); and two periods (also eight layers of atoms) of the zigzag tubes: (4,0), (8,0), (10,0), (11,0), (13,0), (14,0), (16,0), (17,0), (19,0), and (20,0). The central region was sandwiched between two carbon nanotube electrodes of the same chirality as the central region. For the (n,n) armchair tubes the electrodes consisted each of two periods of the tube (0.4926 nm). For the $(n,0)$ zigzag tubes the electrodes consisted of only one period of the tube (0.4266 nm). In DFT/NEGF simulations, each unit cell of the electrodes is assumed to interact only with its nearest neighbours as explained in Chapter 2. The length of the electrodes was thus chosen to be sufficiently long to ensure that this is indeed the case. The simulation box itself is also repeated in the directions transverse to the transport. The transverse dimensions of the different simulation boxes were gradually increased until no significant change in the results was observed. The basis sets used were the single-zeta (SZ), the single-zeta polarized (SZP), the double-zeta (DZ), and the double-zeta polarized (DZP) [75, 76]. The results using the DZP basis set were taken as the reference against which all the other results were compared: the DZP is the most complete basis set used here, and, therefore the one that best predicts the ground state of the system [76]. To further ensure the validity of the DZP basis set as a reference, the simulations for the (2,2), (3,3), (4,4), (5,5), (4,0), (8,0), (10,0) and (11,0) perfect tubes were repeated with the double-zeta double-polarized (DZDP) basis set. For the armchair tubes and the (4,0) metallic tube the maximum difference in calculating the near-zero-bias conductance was 0.1%. For the semiconducting zigzag tubes (8,0), (10,0) and (11,0), the difference between the bandgap calculated from the DZP and the DZDP basis sets was only about 1-2 meV (although both valence and conduction band edges shifted in the same direction by a few meV's relative to the Fermi level in all cases). This assures that no further improvement to the accuracy of the results is likely to be achieved for these tubes by using basis sets more complex than the DZP set. Larger systems could not be simulated with the DZDP basis set due to memory limitations. For Set II, five periods of a (10,0) tube were sandwiched between two nanotube electrodes, each consisting of one period of the tube. The coordinates of the central region were calculated from a 2 ns MD simulation of the central region immersed in water. The basis sets used in the subsequent DFT/NEGF simulations were the same as in SET I. For

SET III, again five periods of a (10,0) tube were sandwiched between two nanotube electrodes, each consisting of one period of the tube, with the addition of a dimer of the amino acid tyrosine adsorbed on the surface of the central region to simulate the effect of an analyte in a carbon-nanotube-sensor application. The coordinates of the atoms of the central region and the atoms of the dimer were taken from an MD simulation of duration 2 ns. The length of the central region was increased compared to SET I in order to accommodate the adsorbed molecule. The length in SET II was chosen to be equal to that in SET III to allow for meaningful comparisons.

3.2 SET I

The energy-dependent transmission coefficient $T(E)$ of the (2,2) tube is shown in Figure 3.1 for the different basis sets used. $T(E)$ gives the fraction of the electron wave which is transmitted from one electrode to the other [60]. The zero-reference of energy is the Fermi level. The SZ basis set predicts a semiconducting tube with an energy gap of 0.68 eV, the DZ basis set predicts an energy gap of 0.1 eV, while both the SZP and the DZP basis sets give almost identical results, clearly showing a metallic behaviour of the same tube. This result demonstrates that the inclusion of polarization for such a small-diameter tube (0.2716 nm) is essential in order to obtain acceptable results. This stems from the fact that polarization models the mixing of different orbitals such as p and d orbitals in carbon [76], a mixing which becomes more apparent as the tube diameter gets smaller. Figure 3.2 shows contour plots for the first transmission eigenstate at an energy of 0.05 eV above the Fermi level of the (2,2) tube, as calculated using both the DZ and the DZP basis sets on a plane passing through the tube axis with its normal in the x -direction (with the transport direction being the z -direction). It is clear that the magnitude and shape of the eigenstate is different for the DZP and DZ cases, indicating a significant influence of the mixing of d orbitals with the p orbitals.

In addition to the mixing of p and d orbitals, it is also worth noting that Figure 3.2 shows that the transmission eigenstate of the (2,2) tube is asymmetric around the carbon atoms: it consists of one lobe pointing to the exterior of the tube, in addition to a smaller lobe pointing to the interior of the tube. In other words, the transmission eigenstate of the (2,2) tube shows a strong ‘blend’ of σ orbitals. This is in contrast with the transmission purely due to the π orbitals predicted by the tight-binding models, and which applies for tubes with a diameter larger than 0.7 nm [81]. This suggests that

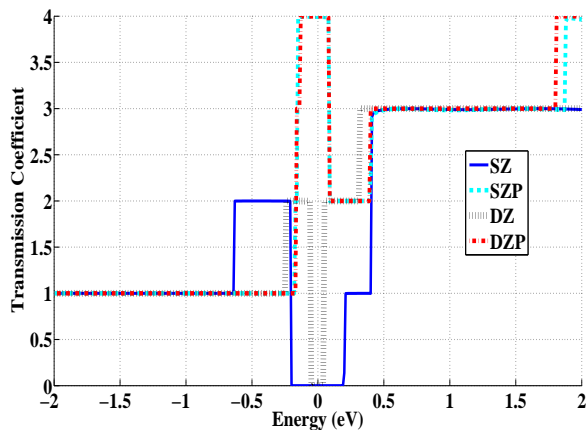


Figure 3.1: Transmission coefficient vs. energy for the (2,2) tube with different basis sets.

in addition to the p - and d -orbitals mixing, a hybridization between the σ and π orbitals also occurs in the (2,2) tube.

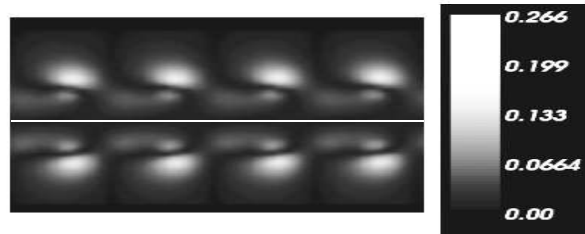
The calculated transmission coefficients for the (3,3), (4,4), (5,5), (4,0), (8,0), (10,0), (11,0), (13,0), and the (14,0) tubes are shown in Figure 3.3 through Figure 3.11. The results for the (16,0), (17,0), (19,0), and the (20,0) tubes are summarized in Figure 3.12 and Figure 3.13 alongside the other semiconducting zigzag tubes.

For the (3,3) tube, the DZ basis set shows a small dip in $T(E)$ at the Fermi level that is not evident with the other basis sets. Though the SZ basis set gives a result closer to the polarized sets than the DZ set, it poorly predicts the transmission coefficient at higher energies, which, for low bias levels should not contribute to the current. The near-zero-bias conductance G is calculated according to the equation²:

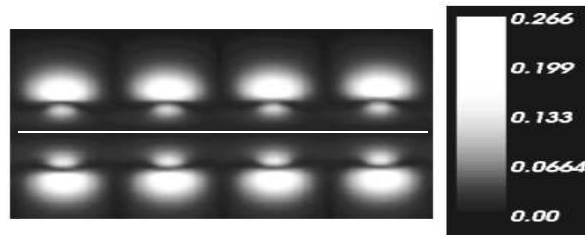
$$G = \frac{2q^2}{h} \int_{-\infty}^{\infty} \left(-\frac{\partial F}{\partial E}\right) T(E) dE, \quad (3.1)$$

where q is the electronic charge, F is the Fermi-Dirac distribution function, and E is the energy. For near zero-bias calculations, μ is taken to be zero, and $T(E)$ is assumed not to vary considerably from the calculations at equilibrium. The values of G are shown in Table 3.1.

²It has to be noted that the lower limit of the integral in [80] was incorrectly set to the Fermi level of the contact with the higher potential. The conclusions in [80], however, are not affected.



(a)



(b)

Figure 3.2: The first transmission eigenstate calculated for the (2,2) tube in units of $\text{\AA}^{-3/2}$ at an energy 0.05 eV above the Fermi level, (a) using the DZ basis set, (b) using the DZP basis set. The horizontal white line in the middle denotes the axis of the tube.

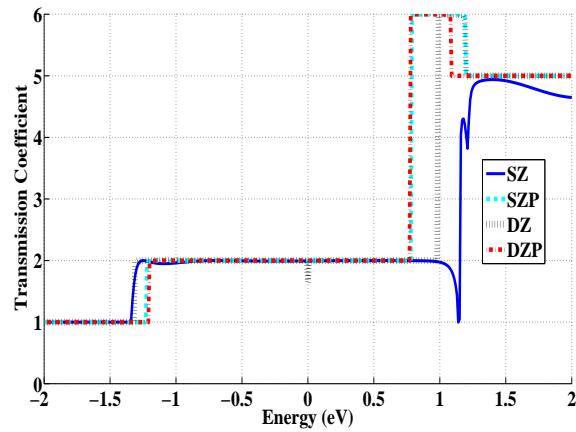


Figure 3.3: Transmission coefficient vs. energy for the (3,3) tube with different basis sets.

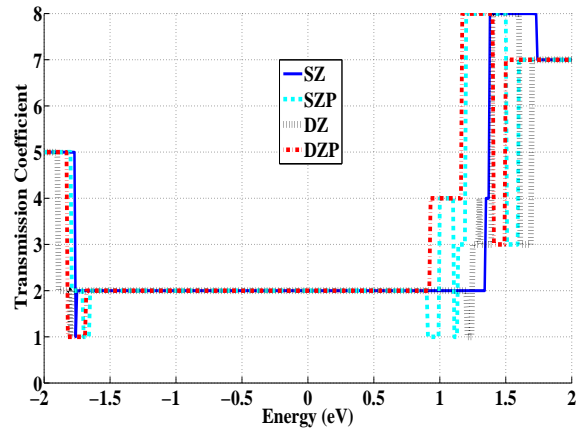


Figure 3.4: Transmission coefficient vs. energy for the (4,4) tube with different basis sets.

It can be seen from Table 3.1 that for the armchair tubes, with the exception of the (2,2) tube, all the basis sets give almost identical values of G . From the corresponding transmission coefficient figures, we can see that all the basis sets predict a metallic (zero-gap) tube except for the (2,2) tube. For the (2,2) tube, the SZP and DZP give the same value of G which is much higher than those predicted from the SZ and DZ calculations. This suggests that the use of even a minimal SZ basis can be adequate for the simulations

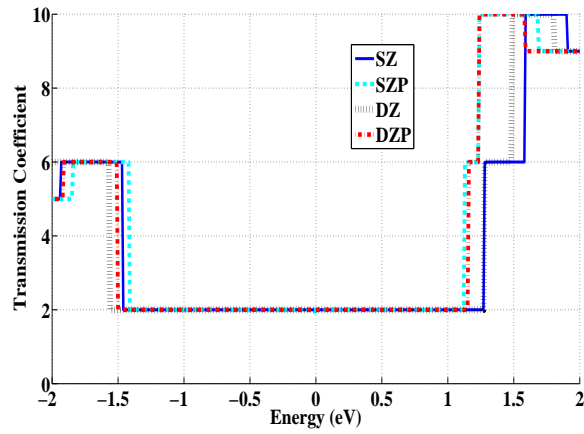


Figure 3.5: Transmission coefficient vs. energy for the (5,5) tube with different basis sets.

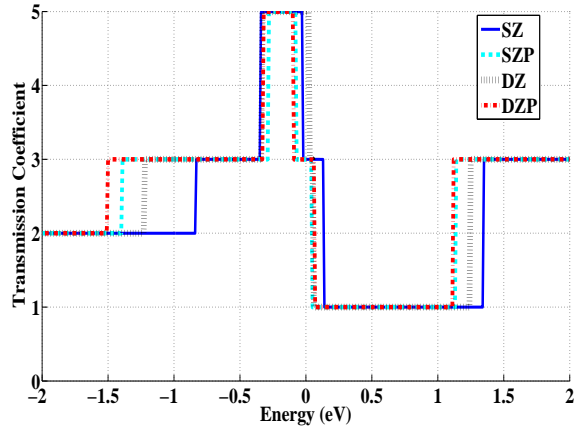


Figure 3.6: Transmission coefficient vs. energy for the (4,0) tube with different basis sets.

of armchair tubes with the exception of the (2,2) tube. Table 3.2 shows the computational resources required for the simulations of the (4,4) tube (160 atoms).

It can be seen that the DZP requires considerably longer time, more memory size, and a much larger amount of disk storage than the other basis sets. These requirements can be very problematic, and even prohibitive, for longer, and/or larger-diameter armchair tubes.

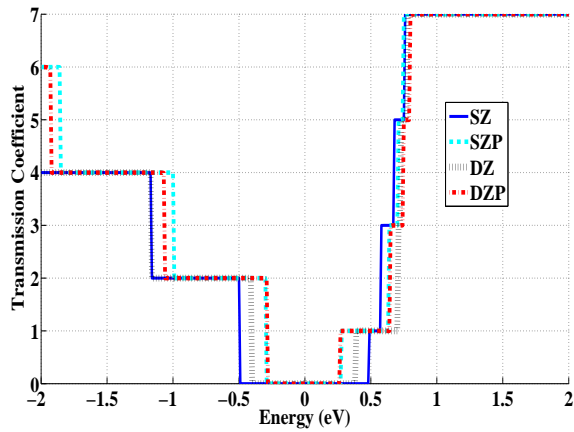


Figure 3.7: Transmission coefficient vs. energy for the (8,0) tube with different basis sets.

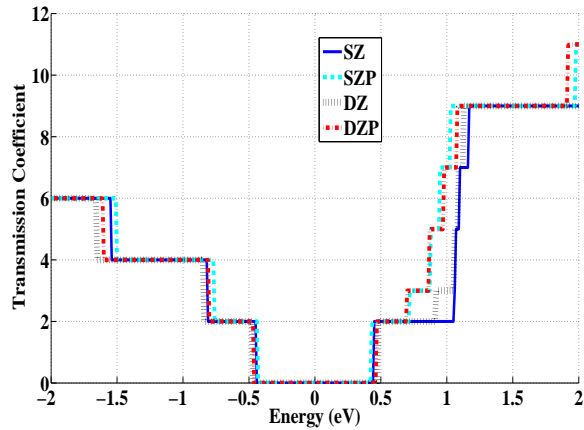


Figure 3.8: Transmission coefficient vs. energy for the (10,0) tube with different basis sets.

For the (4,0) tube, the value of $T(E)$ at and near the Fermi level with the non-polarized basis sets is significantly different from its value with the polarized ones. For example, at the Fermi level, $T(E)$ is equal to 5 with the DZ basis set, compared to 3 with the polarized basis sets. The same problem occurs with the SZ basis set at an energy just 20 meV below the Fermi level. Since the conduction in such a metallic tube is due to the electrons with energies within a few kT 's of the Fermi level (where kT is the thermal energy),

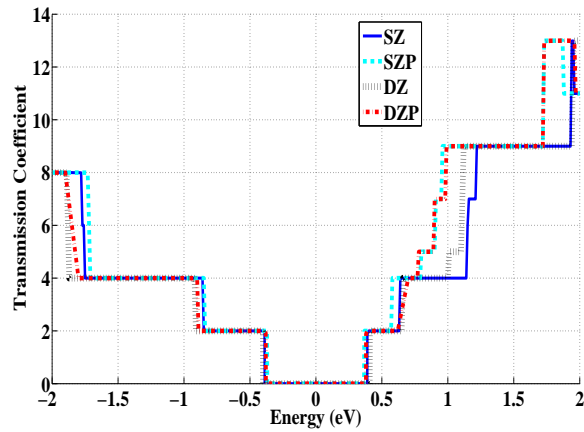


Figure 3.9: Transmission coefficient vs. energy for the (11,0) tube with different basis sets.

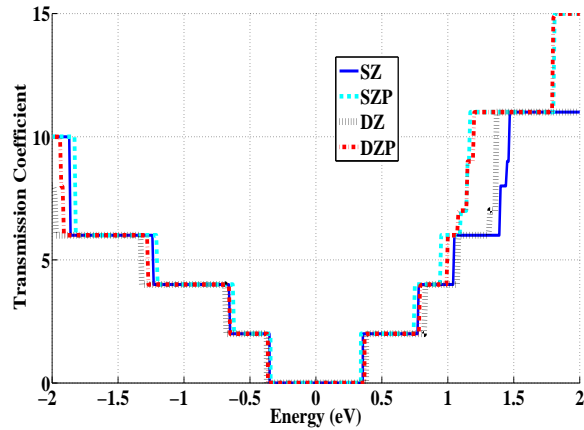


Figure 3.10: Transmission coefficient vs. energy for the (13,0) tube with different basis sets.

this difference in the value of the transmission coefficient is not acceptable, and the inclusion of polarization in the basis set is necessary. Even the SZP basis set predicts a near-zero-bias conductance that is about 11% less than that calculated using the DZP basis set. Therefore, a minimum of a DZP basis set is required to accurately describe the near-zero-bias conductance of the (4,0) tube.

It has to be noted that the metallic behaviour exhibited by the (4,0)

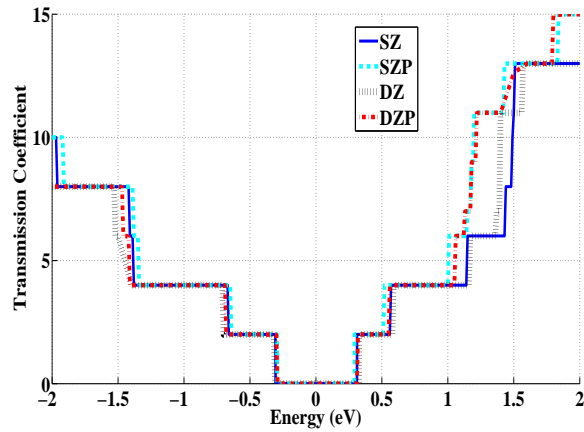


Figure 3.11: Transmission coefficient vs. energy for the (14,0) tube with different basis sets.

Table 3.1: Near-zero-bias conductance for the metallic tubes in units of Siemens. The subscript of G designates the corresponding tube.

	$G_{(2,2)}$	$G_{(3,3)}$	$G_{(4,4)}$	$G_{(5,5)}$	$G_{(4,0)}$
SZ	8.62e-8	15.46e-5	15.52e-5	15.52e-5	2.75e-4
SZP	3.04e-4	15.50e-5	15.52e-5	15.42e-5	2.18e-4
DZ	3.96e-5	15.24e-5	15.52e-5	15.52e-5	3.28e-4
DZP	3.04e-4	15.50e-5	15.52e-5	15.52e-5	2.25e-4

Table 3.2: Computational resources for both the DZ and DZP basis sets used for computing the data in Figure 3.4. Parallel calculations were conducted on a 64-bit, 8-processor (Intel(R), Xeon(TM), 2.66 GHz CPU each) Dell machine.

	Total Memory (GB)	CPU time (h)	Output file size (MB)
SZ	2.0	0.46	4.3
SZP	2.7	1.8	18.4
DZ	2.6	1.48	14.7
DZP	4.0	4.9	37.5

tube is in contradiction to the semiconducting behaviour predicted by simple tight-binding models. This is due to the hybridization of the σ and π orbitals (which was also observed for the (2,2) tube as discussed above). This hybridization becomes significant in small-radius tubes [81], and can lead to the observed metallic behaviour of the (4,0) tube [82]. It is important to emphasize that this hybridization is not the same as the mixing of the p and d orbitals mentioned above since the σ and π orbitals arise from the hybridization of the s and p orbitals in carbon. In general, tight-binding π -bond models have been previously shown to fail for tubes with a diameter smaller than that of the (10,0) tube [81, 83].

The $T(E)$ of the (8,0) tube shows an energy gap indicating a semiconducting tube. The SZP overestimates the bandgap by 31 meV compared to the bandgap predicted by the DZP basis set. The DZ and SZ basis sets give values for the gap of 786 meV and 987 meV compared to the 543 meV calculated by the DZP set. The results again suggest the necessity of using the DZP basis set, and the importance of the mixing of p and d orbitals in this tube.

For the semiconducting zigzag tubes larger than the (8,0) tube, the calculated bandgap is shown in Figure 3.12. The corresponding difference in the calculated bandgap (ΔE_G) with respect to that calculated from the DZP basis set ($E_{G_{DZP}}$) is shown in Figure 3.13. This difference depends on the exact chirality of the tube and not only on its diameter. For tubes with $n = 3p + 1$, where p is an integer, the DZ basis set overestimates the gap by about 20 meV for all tubes, while the SZ basis set underestimates the gap by about 40 meV for the (10,0) tube and then the difference decreases gradually with increasing the tube diameter to reach ~ 20 meV for the (19,0) tube. We also notice that the rate of decrease of ΔE_G with respect to n decreases with increasing n .

The SZP basis set shows a similar behaviour to the SZ basis set, though the difference in the bandgap with respect to $E_{G_{DZP}}$ is systematically larger than the that for the SZ basis set. For tubes with $n = 3p + 2$, the DZ basis set overestimates the gap compared to $E_{G_{DZP}}$ by 51 meV for the (11,0) tube and the difference decreases gradually to reach 26 meV for the (20,0) tube. The SZ basis set, on the other hand, overestimates the gap by about 20 meV for the (11,0) tube and then the difference decreases rapidly to about 2 meV for (17,0) and (20,0) tubes. Again the SZP set shows a similar behaviour to the SZ set and the difference in the bandgap is larger in the case of the SZP basis set. A similar phenomenon has been observed in [83] when comparing the bandgap calculated using the π -bond model and using DFT simulations with a minimal basis set. It is noteworthy from the transmission

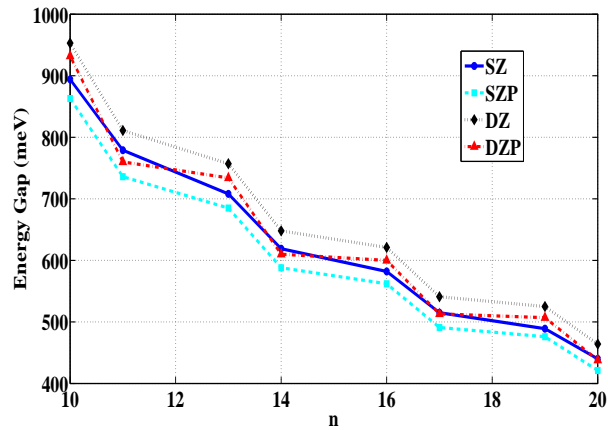


Figure 3.12: Bandgap for the semiconducting $(n,0)$ tubes as calculated using different basis sets vs. the chirality index n .

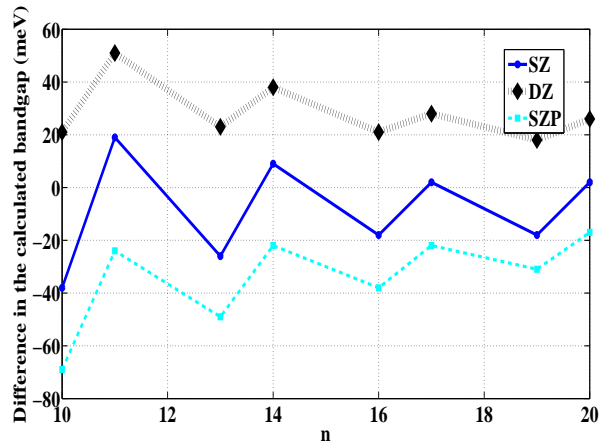


Figure 3.13: Difference in the calculated bandgap using the SZ, DZ, and SZP basis sets, and that calculated using the DZP basis set for the semiconducting $(n,0)$ tubes vs. the chirality index n .

coefficient graphs that, at energies higher than 750 meV, the non-polarized basis sets always deviate considerably from the DZP basis set, and that at such energies the SZP basis set produces results that most closely match those of the DZP basis set. Therefore, if these energies are of a particular interest, the use of a polarized basis set appears necessary.

The carbon nanotube band structure can be obtained from that of graphene according to the zone-folding scheme [81]. Therefore, to explain why the results of the $(n,0)$ tubes depend on whether $n = 3p + 1$ or $n = 3p + 2$ as mentioned above, the band structure of graphene was calculated using the SZ, DZ, SZP, and DZP basis sets. The lowest conduction subband and the top valence subband are shown in Figure 3.14. The difference between the lowest conduction subband and the top valence subband (ΔE) was then calculated at different k -points. The difference at the high-symmetry K point was zero as expected. According to the zone folding (ZF) scheme, only certain values of the \mathbf{K} vector are allowed, as illustrated by the vertical lines in Figure 3.14 for the (10,0), (11,0), (19,0), and (20,0) tubes. The bandgap of tubes with $n = 3p + 1$ is obtained from the lines to the right of the K -point, whereas the bandgap of tubes with $n = 3p + 2$ is obtained from the lines to the left of the K -point. The bandgap corresponding to the different semiconducting zigzag tubes mentioned above was then calculated using different basis sets, and applying the ZF scheme. The difference between the bandgap calculated according to the ZF scheme using the SZ, DZ, and SZP basis sets, and that calculated using the DZP basis set ($\Delta E_{G_{ZF}}$) is shown in Figure 3.15. It can be seen from Figure 3.15 that $\Delta E_{G_{ZF}}$ still exhibits a non-monotonic trend with respect to the chirality index n similar to that shown in Figure 3.13, though the exact values are different. Thus, it is suggested here that the trend in bandgap differences between the various basis sets has its origin in the zone-folding scheme used to calculate the band structure of nanotubes from that of graphene.

From the results of SET I, we conclude that for bandgap and near-zero-bias conductance calculations of perfect carbon nanotubes, the choice of the basis set depends on the chirality and the diameter of the tube. For zigzag tubes smaller than the (14,0) tube, a DZP basis set is in general necessary for accurate DFT/NEGF simulations. For the (14,0) tube and larger zigzag tubes, if $n = 3p + 1$, a DZP basis set may still be necessary for DFT/NEGF simulations, whereas if $n = 3p + 2$, the SZ basis set can be sufficient to get an estimation of the bandgap of the tube. For the armchair tubes, a minimal basis set may be sufficient for an accurate estimation of the near-zero-bias conductance, and for a correct qualitative description of the metallic behaviour of these tubes. The exception is the (2,2) tube, which requires a polarized basis set to account for the mixing of p and d orbitals, which appears to play an important role in the properties of the (2,2) tube.

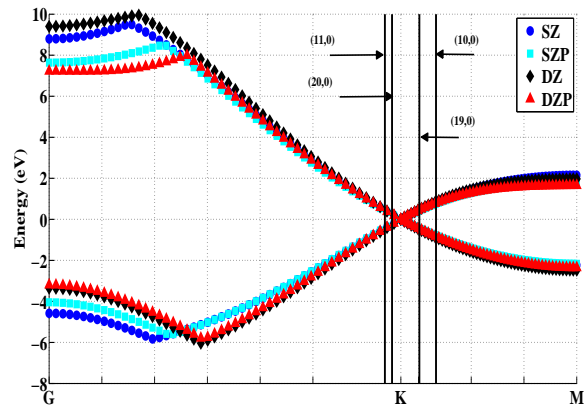


Figure 3.14: The lowest conduction subband and the top valence subband of the E-k band diagram of graphene calculated using different basis sets. The G, K, and M points are the high-symmetry points Γ , K , and M , respectively. The vertical lines are the cut-lines at which the bandgap of the (10,0), (11,0), (19,0), and (20,0) tubes is calculated according to the zone-folding scheme. Lines to the left of the K point correspond to $(n,0)$ tubes with $n = 3p+2$, and lines to the right of the K point correspond to $(n,0)$ tubes with $n = 3p + 1$.

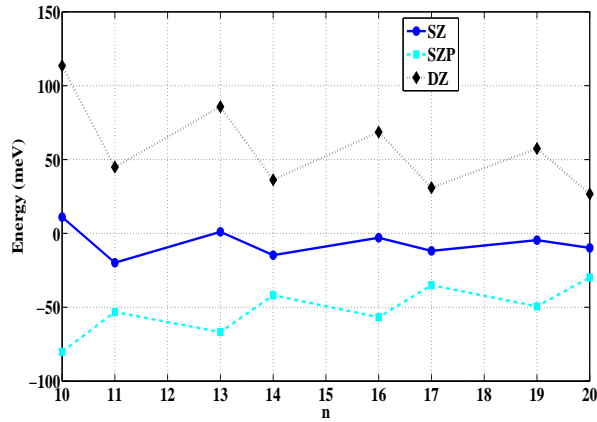


Figure 3.15: Difference in the calculated bandgap for the same zigzag tubes shown in Figure 3.13 using the SZ, DZ, and SZP basis sets, and that calculated using the DZP basis set, according to the zone-folding scheme.

3.3 SET II

The calculated transmission coefficient of a (10,0) tube with atom coordinates determined from an MD simulation of the tube in water is shown in Figure 3.16. The maximum displacement of carbon atoms with respect to the ideal case was about 0.3 Å. First, we notice that unlike the perfect tubes, the transmission coefficient does not show a step-like behaviour. This is due to the lack of perfect periodicity in the structure, and therefore quantum mechanical reflections may occur at the electrode/central region interface, and within the central region itself.

The calculated bandgap for the DZP, DZ, and SZ basis sets was exactly the same as calculated for the perfect (10,0) tube in SET I. The bandgap calculated by the SZP basis set was 3 meV lower than its counterpart in SET I.

Therefore, we conclude that small displacements in the carbon atom positions need not influence the choice of the basis set, and, in general, a DZP basis set would be recommended for such a simulation unless the system is too large (*e.g.*, a longer tube), in which case memory limitations and/or time requirements may dictate the using of a lower basis set according to the rules and observations described for SET I.

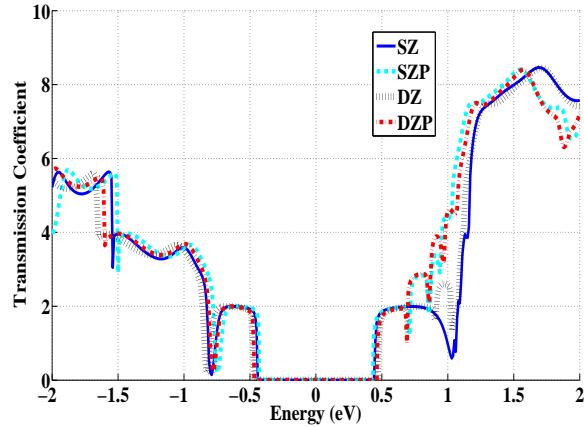


Figure 3.16: Transmission coefficient vs. energy for the (10,0) tube after an MD simulation, and with different basis sets.

3.4 SET III

In this set, the effect of the existence of a physisorbed molecule on the nanotube surface on the choice of the basis set is investigated. A 2 ns MD simulation of a (10,0) tube and a dimer of the amino acid tyrosine in water showed that the dimer/nanotube-surface separation was 0.265 nm. It was also found that the aromatic rings stack over the hexagonal rings of the nanotube. The configuration at the end of the MD simulation is shown in Figure 3.17. The MD simulations are necessary to obtain the relative coordinates of the biomolecule and the nanotube since DFT optimization alone does not account for van der Waals forces [84–88], which are important in nanotube/biomolecule interactions [34, 89]. The maximum displacement of the atoms of the tube with respect to the ideal case was about 0.3 Å as in SET II. The transmission coefficient resulting from the subsequent DFT/NEGF simulations is shown in Figure 3.18. The results are very similar to those of SET II in the sense that the DZ and DZP sets exhibit a rather good agreement in the range of energies within a few kT 's above the edge of the lowest conduction subband (E_C), and that at higher energies the DZ and DZP results deviate from each other. At these energies the SZP is in better agreement with the DZP basis set, indicating a more significant effect of the polarization. The calculated bandgap was 898 meV for the SZ basis set, 867 meV for the SZP basis set, 954 meV for the DZ basis set, and 932 meV for the DZP basis set. Comparing these results with the results shown in Figure 3.12, it is clear that the physisorbed biomolecule did not have a significant effect on the calculated bandgap for all basis sets. However, one important parameter that can be quite sensitive to the basis set is the Mulliken population [90], from which the electron density is calculated. Set III is particularly prone to such a sensitivity due to the presence of an adsorbed molecule and the possible orbital overlap between the nanotube and the biomolecule. The charge transfer between the tube and the biomolecule is an important factor in the nanotube/biomolecule interaction. The charge transferred from the amino acid to the tube was calculated to be $0.3057q$ in the case of the DZP basis set (Q_{DZP}), $0.3306q$ in the case of the DZ basis set (Q_{DZ}), $0.702q$ in the case of the SZP basis set (Q_{SZP}), and $0.8474q$ in the case of the SZ basis set (Q_{SZ}). The difference between Q_{DZ} and Q_{DZP} is only $0.0249q$ compared to $0.3963q$ for the difference between Q_{SZP} and Q_{DZP} , and $0.5417q$ for the difference between Q_{SZ} and Q_{DZP} . The Mulliken population calculated for each carbon atom on the tube showed a maximum difference of less than 1% for the DZ set compared to the DZP basis set. The SZ and SZP basis sets show higher

relative difference compared to the DZ basis set, especially for the dimer atoms. Although the DZ basis set also shows relatively large differences in the Mulliken population for the dimer atoms (especially in hydrogen atoms where a relative difference of around 20% was observed), these differences did not have a significant impact on the total electronic charge of the amino acid, or on the electronic density in the tube, or the transmission coefficient of the tube. In general, a DZP basis set is required for such a simulation, and the SZ or the SZP basis sets would not accurately predict the Mulliken population. The resources required to perform such a simulation using the DZP basis set and the DZ basis set are shown in Table 3.3. It is clear that the DZP basis set requires a significantly larger amount of time and memory resources, which may not be available. In such a case, a DZ basis set may be adequate for the simulation. Another solution could be to use different basis sets for different atoms, *i.e.*, use a polarized basis set to describe the atoms of the biomolecule and a lower basis set to describe the atoms of the carbon nanotube. However, this should be done very carefully since using different basis sets for different atoms can introduce the so-called ‘basis set superposition error’ [91, 92].

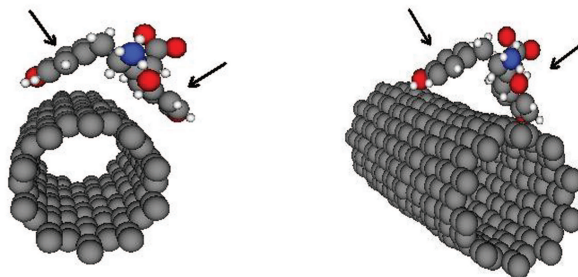


Figure 3.17: Different views for the configuration of the central region of the structure simulated in Set III following a 2 ns MD simulation. The arrows indicate the aromatic rings of the tyrosine dimer.

3.5 Effect of the Electrode Length

In the discussion above, it was briefly mentioned that the electrodes should be long enough so that each unit cell of the electrode interacts only with its nearest-neighbour image (as the electrode cell is assumed to be repeated

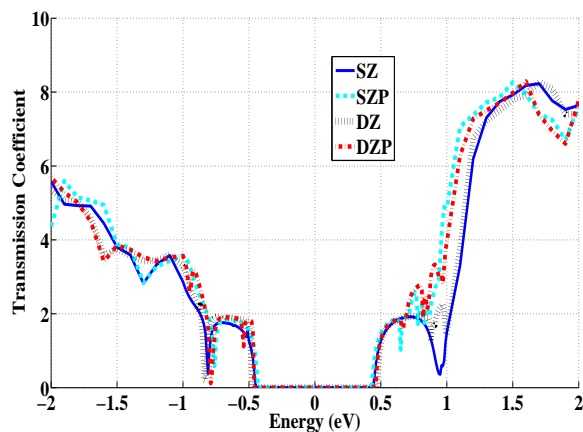


Figure 3.18: Transmission coefficient vs. energy for the (10,0) tube with an adsorbed tyrosine dimer after an MD simulation, and with different basis sets.

Table 3.3: Computational resources for both the DZ and DZP basis sets used for computing the data in Figure 3.18. Parallel calculations were conducted on a 64-bit, 8-processor (Intel(R) Xeon(TM) 2.66 GHz CPU each) Dell machine.

Basis set	Total Memory (GB)	CPU time (h)	Output file size (MB)
DZ	16	132.97	22
DZP	24	259.02	56

infinitely to form a semi-infinite electrode as explained in Chapter 2). In this section, the effect of the length of the electrode on the results of DFT/NEGF simulations is illustrated, and how this may affect the choice of the basis set is explained.

The simulations of the (5,5) tubes were repeated with an electrode length of one unit cell (two layers of atoms), as compared to two unit cells (four layers of atoms) in the simulations in SET I above. For each electrode length, the simulations were repeated using the SZ basis set, and the DZ basis set. Figure 3.19 shows the transmission coefficient for the various sets of simulations described above. It can be seen that with the DZ basis set, the short electrode resulted in an erroneous transmission coefficient.

Similar results were previously attributed to the effect of the curvature of the tube [93], while, in fact, they were artefacts of the short electrode length that permitted the interaction between non-neighbouring electrode cells, thus violating the assumptions detailed in Chapter 2.

The SZ basis, on the other hand, does not exhibit the same problem. This is explained by the fact that the SZ basis set has a smaller spatial extent than the DZ basis set. Therefore, the short length of the electrode, in the case of SZ-basis-set simulations, was sufficient to prevent any significant interaction between non-neighbouring electrode cells, in contrast with the DZ-basis-set simulations.

In general, we suggest that the electrode length should be gradually increased until no significant change in the results is observed to avoid non-physical artefacts resulting from a poor choice of the electrode length.

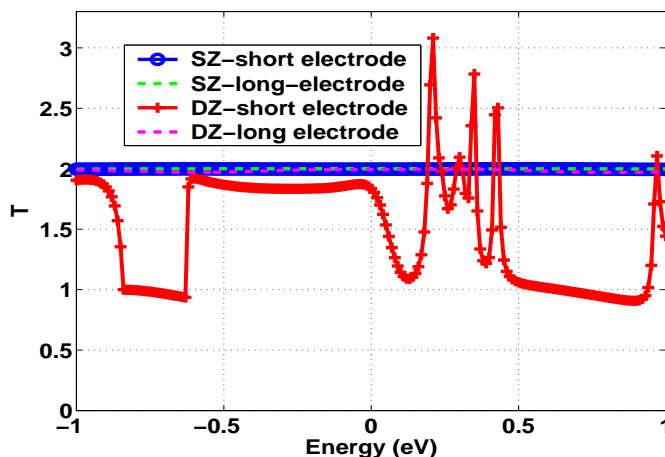


Figure 3.19: Transmission coefficient vs. energy for the (5,5) tube with different electrode lengths, and with different basis sets.

3.6 Overcompleteness

One problem that may occur with the choice of basis sets, is to choose an overcomplete basis set. Overcompleteness means that the basis functions become linearly dependent, *i.e.*, one (or more) of the basis functions can be written as a linear combination of the others [94]. To ensure the proper choice of the basis set, the total energy of the system should be checked. Barring overcompleteness in the basis set, the total energy of the system

should decrease using a more complete basis set, *i.e.*, the total energy is variational with the number of basis functions [95]. Therefore, if the total energy of the system is found to increase with increasing the completeness of the basis set, that indicates the overcompleteness of the basis set in question. A less complete basis set is generally recommended in this case. It is worth noting that this check was performed for the simulations described in this chapter, and the total energy was found to be variational with the basis set up to the DZP basis set. The DZDP basis set was also found to be undercomplete with the exception of the (2,2) tube simulations, where the DZDP basis set was overcomplete.

3.7 Conclusion

To sum up the results of this chapter, the effect of the basis set choice in *ab initio* DFT/NEGF simulations on the transmission coefficient, near-zero-bias conductance, and bandgap of various carbon nanotubes were performed. The results show that for armchair tubes, a minimal basis set can be sufficient to get an accurate estimation of the near-zero-bias conductance, with the exception of the (2,2) tube, for which polarization should be included to get the near-zero-bias conductance and to capture the metallic behaviour of this tube. For zigzag tubes, it was found that the choice of the basis set depends on both the diameter and the chirality of the tube. It was found that small displacements in the atomic positions do not affect the choice of the basis set, and that for systems containing both a nanotube and a physisorbed biomolecule, a double-zeta polarized basis set is recommended for an accurate Mulliken population analysis, though a double-zeta basis set predicts the total charge in both the nanotube and the biomolecule accurately. It was also shown that the (2,2) tube is a fully metallic tube (in contrast with previous predictions in the literature [93, 96]), and it was demonstrated that this is due to the hybridization between the carbon *p*- and *d*-orbitals. It was also shown that the electrode length is closely connected to the basis-set choice. In general, longer lengths of the electrodes are likely to be needed for simulations using more complete basis sets.

Chapter 4

Simulation Results

4.1 Driving Forces for the Adsorption Process

This chapter begins with discussing the relevance of hydrophobic interactions and van der Waals forces in the adsorption process of amino acids on carbon nanotubes. The adsorption mechanisms are not well understood [97], and an important suggested mechanism of adsorption is the hydrophobic interactions [98, 99]. It is therefore important to investigate the role of such interactions in the adsorption process.

4.1.1 Simulation Flow

MD simulations for carbon nanotubes with amino acids have been carried out using GROMACS. Both large-diameter tubes (chirality of (12,11)) and small-diameter tubes (chirality of (10,0)) were used, with the length of the tubes being 8 nm in all cases. The amino acids isoleucine (ILE) (which has a strongly hydrophobic neutral side-chain), and asparagine (ASN) (which has a strongly hydrophilic neutral side-chain), were investigated in separate simulations. In each case, forty dimers of the relevant amino acid were positioned along the length of the tube at a radial distance of 1 nm from the surface of the tube. Each dimer consisted of two residues, where the residue is the form taken by amino acids when they constitute a chain of peptides, or comprise parts of proteins [100]. As an example, the initial positions of the ASN dimers around a (12,11) tube are shown in Figure 4.1. A reaction duration of 6 ns was simulated, under conditions of constant pressure (1 atm) and temperature (300 K) using Parrinello-Rahman- and Berendsen-coupling, respectively. The simulation was performed in an aqueous medium. The AMBER99 force field port in GROMACS was used, and the TIP3P water model was implemented.

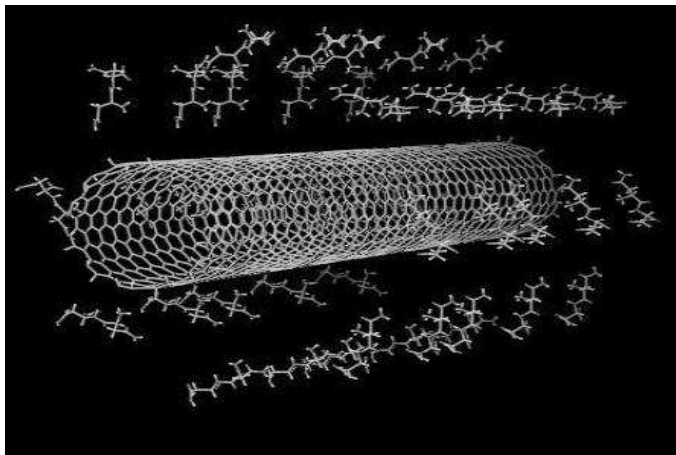
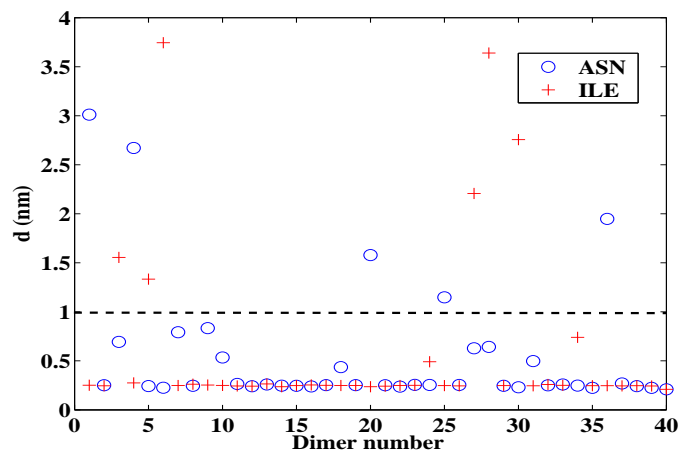


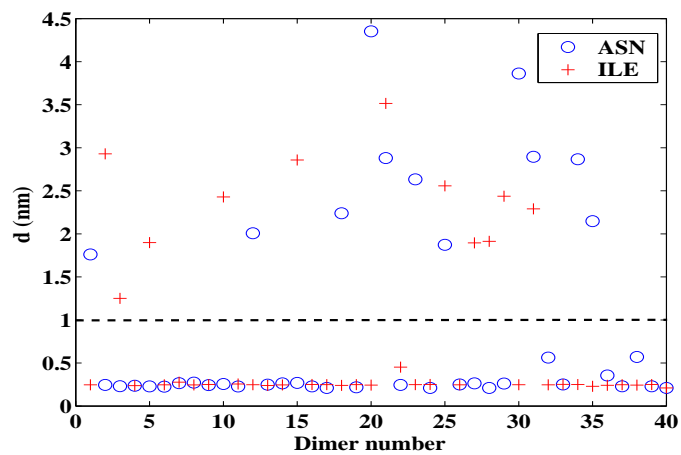
Figure 4.1: Initial configuration of ASN dimers surrounding a (12,11) CNT at a radial distance of 1 nm from the CNT surface. The water molecules in which the dimers and CNT are immersed are omitted for clarity.

4.1.2 Results

The final radial positions of the dimers in each case are shown in Figure 4.2, as calculated from GROMACS. It is clear that there is significant adsorption of both the hydrophilic (ASN) and hydrophobic (ILE) dimers. This indicates that some force, other than that merely related to the dimer-water interaction, is operative. Evidence that this force is the van der Waals (VDW) force comes from Figure 4.3, which shows an increase, and then a tendency towards saturation, of the magnitude of the VDW energy as the reactions proceed and then stabilize. In the hydrophobic case the VDW potentials settle faster than in the hydrophilic case, from which it can be inferred that, while hydrophobicity speeds up the adsorption process, it is not essential for its occurrence [89]. This is in agreement with previous works [101], which have considered peptide encapsulation within nanotubes, rather than adsorption on the outer surface. This suggests that, in principle, all proteins will have a tendency to be adsorbed on the surface of the nanotube.

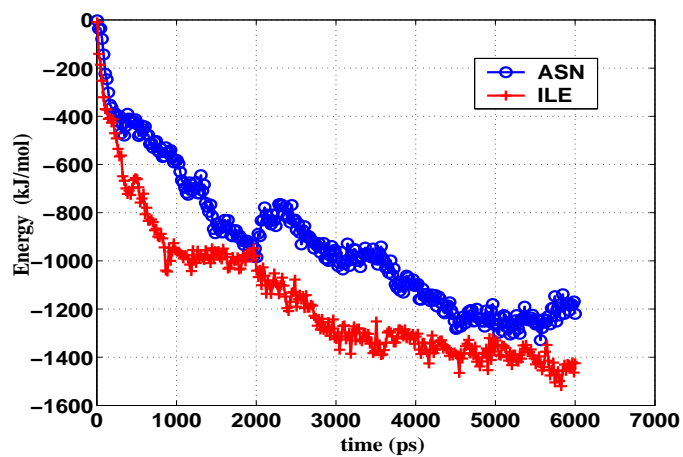


(a)

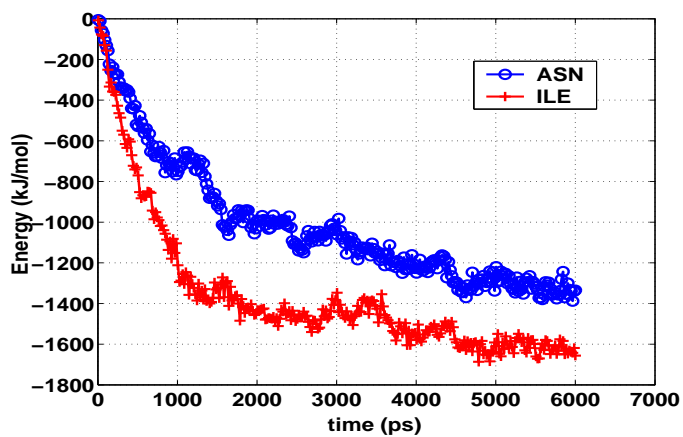


(b)

Figure 4.2: Final radial distances between the dimers and the nanotube surface after a 6 ns simulation. (a) (10,0) CNT. (b) (12,11) CNT. The dashed line indicates the initial radial position of the dimers.



(a)



(b)

Figure 4.3: Evolution of the VDW-associated potential energies vs. time for ASN and ILE at an initial position of 1.0 nm distance from the tube. (a) (10,0) CNT, (b) (12,11) CNT.

4.2 Metallic Tubes

4.2.1 Armchair Tubes

The effect of amino-acid adsorption on several armchair tubes was tested. The simulated structures consisted of 10 periods (2.2 nm) of the armchair tubes (4,4), and (5,5). The electrode cells consisted each of two periods of the corresponding nanotube to avoid second-neighbour-cell interactions. The basis set used for the (4,4) tube was the DZP basis set while that for the (5,5) tube it was the DZ basis set according to the rules described in Chapter 3.

The results show that the fully-metallic armchair tubes are insensitive to amino-acid adsorption. The I-V characteristics of these tubes did not show any significant response to the adsorption of aromatic neutral amino acids (tyrosine, phenylalanine, and tryptophan), or the charged amino acid arginine. The negatively-charged amino acid glutamate could not be adsorbed on the surface of the nanotubes.

4.2.2 Small-Radius Zigzag Tubes

Small-radius tubes (<0.5 nm) are metallic regardless of their chirality [102]. The (4,0) and (5,0) tubes were studied to investigate their potential as amino-acid sensors. The simulated tubes consisted of 5 periods (2.2 nm) of each of the tubes immersed in water. The MD simulations spanned 2 ns for each simulation. The tubes were simulated both in the absence and in the presence of a dimer of each of the amino acids arginine, tyrosine, phenylalanine and glutamate. Glutamate failed to adsorb on the tubes (ending at a distance of more than 2 nm from the surface of the tube) and was discarded for further *ab initio* simulations. The other amino acids were adsorbed on the tubes and were included into subsequent DFT/NEGF simulations. The DFT/NEGF simulations showed that these tubes are sensitive to the vibration of their atoms in the aqueous medium. This is likely because the metallic nature of these tubes arises from the hybridization between the *p*- and *d*-orbitals, which is expected to be sensitive to local changes in the radius of the tubes. Therefore, the vibration of the carbon atoms, which changes the instantaneous local radius of the tube, will affect the *p-d* hybridization thus decreasing the transmission probability around the Fermi level, as shown in Figure 4.4 for the (4,0) tube. The (5,0) tube, with a radius larger than that of the (4,0) tube, does not exhibit the same behaviour for the same length. However, as the length of the tube is doubled, the same problem arises. This is because the larger the radius of the tube, the longer

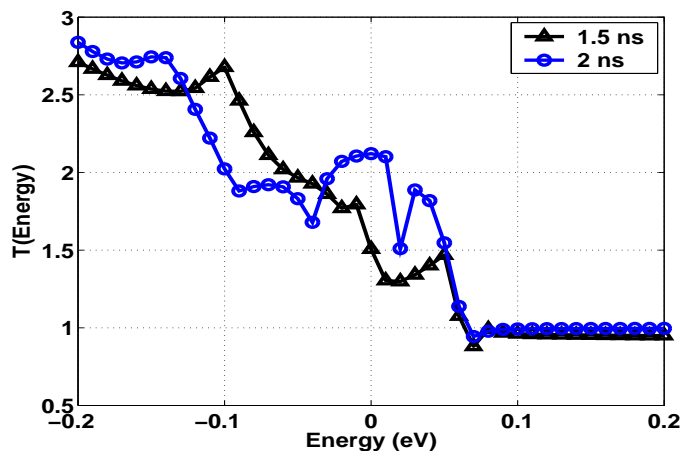
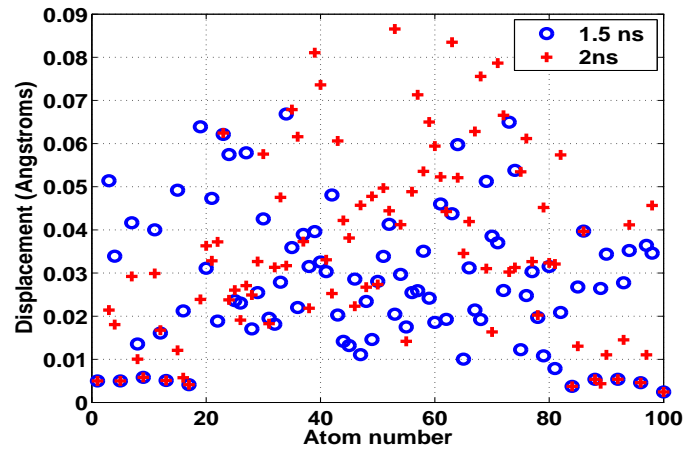


Figure 4.4: Transmission coefficient for the 2.2 nm (4,0) tube at two different times of the MD simulation.

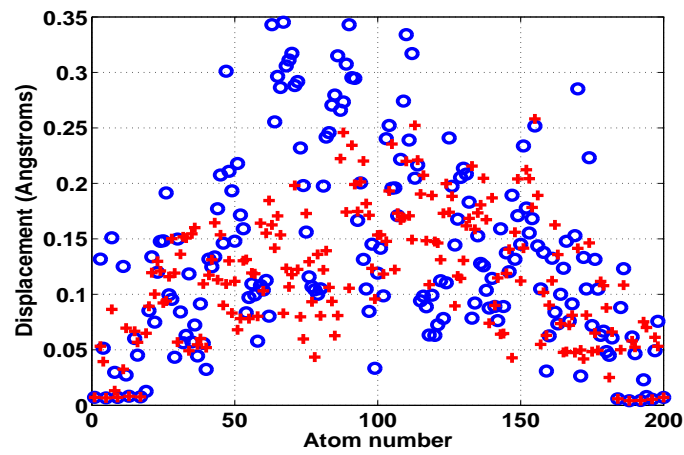
it must be to exhibit large oscillations in the atomic coordinates. The displacement of the atoms of the (5,0) tube are shown in Figure 4.5 for both lengths. It is clear that the displacements for the longer tube are larger, and that they differ significantly over time. We can see from Figure 4.6 that, although the 2.2 nm tube shows a clear response to the adsorption of arginine, tyrosine, tryptophan, and phenylalanine, the 4.4 nm tube is as sensitive to immersion in water as it is to the amino-acid adsorption. Therefore, the detected response for such tubes cannot be conclusively attributed to the analyte. We conclude that the small-radius tubes are not good candidates for sensing in aqueous media. For larger-radius tubes, this problem is much less exaggerated, as will be discussed in the next sections.

4.3 Semi-Metallic Nanotubes

In this section, the effect of amino-acid adsorption on the conductance of single-walled carbon nanotubes in a two-probe configuration is studied [103]. Semi-metallic tubes (tubes with very small bandgaps) are chosen as they have a higher possibility of conductance modulation in such a two-probe configuration than either metallic tubes with zero gaps, where no change in the current is expected, or semiconducting tubes which need a much higher bias to cause any appreciable current at all. Amino acids are chosen as they are the building blocks of proteins, and because understanding their

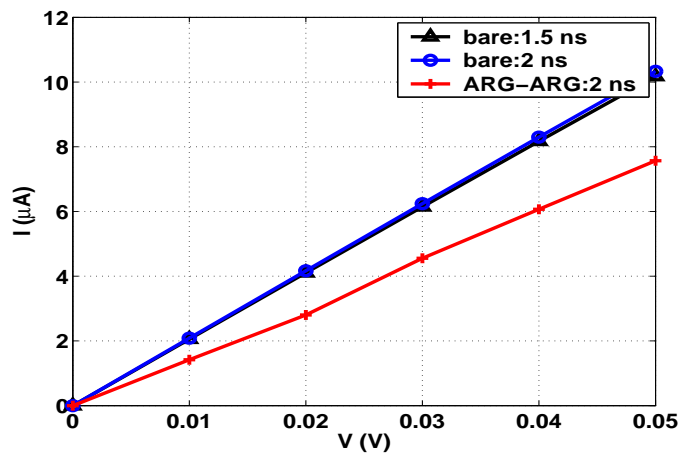


(a)

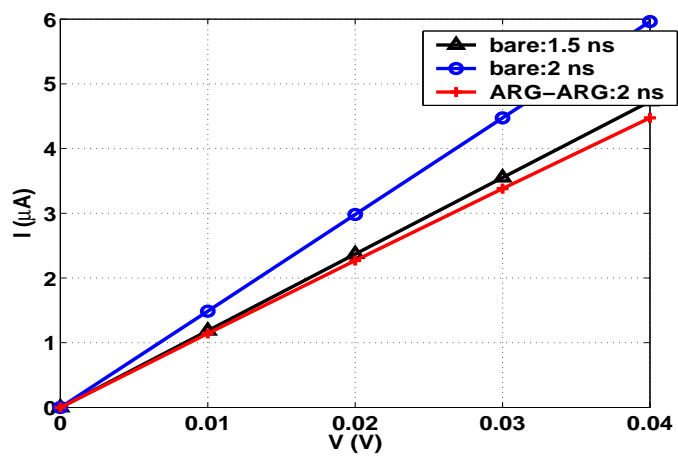


(b)

Figure 4.5: Displacement of the (5,0)-nanotube atoms for (a) 2.2 nm tube (b) 4.4 nm tube. The displacements in (b) are significantly larger than in (a) and also the differences between the displacements at 1.5 ns and 2 ns in (b) are larger than in (a), indicating larger oscillations.



(a)



(b)

Figure 4.6: I-V characteristics of the (5,0) tube both bare and with an adsorbed dimer of arginine for (a) 2.2 nm tube, (b) 4.4 nm tube.

interaction with CNTs will help to understand how full proteins (which are too complex to be presently simulated by the state-of-the-art *ab initio* techniques used here) interact with CNTs as explained in Chapter 1.

Molecular dynamics (MD) simulations are used to get the relative coordinates of the CNT and the adsorbed biomolecule. The results are then used in *ab initio* density functional theory/non-equilibrium Green's function (DFT/NEGF) simulations [60] within the local density approximation (LDA) [63]. The study considers the semi-metallic (9,0), (12,0), (15,0), and (18,0) tubes. For the amino acids, the study covers a range of amino acids of different charge types. Dimers of the neutral aromatic amino acids tyrosine (TYR), tryptophan (TRP), and phenylalanine (PHE) were used, as well as dimers of the positively charged amino acid arginine (ARG), the negatively-charged amino acids glutamate (GLU) and aspartate (ASP), and the two neutral non-aromatic amino acids asparagine (ASN), and isoleucine (ILE).

4.3.1 Simulated Structures

The simulation flow was as follows: MD simulations of five periods (~ 2.2 nm) of each of the nanotubes in water, with and without the amino-acid dimers, were first performed using the package GROMACS. The AMBER99 port [51] and the TIP3P model [52] were used for the amino acids and the water, respectively, and simulations were run for 2 ns to get the relative coordinates of the atoms of the nanotubes and the dimers. The pressure was held at 1 atm using Parrinello-Rahman coupling [104], and the temperature was maintained at 300 K using Berendsen coupling. A Morse potential was used to describe the bonds of the CNT and a cosine potential was used to describe the angles as explained in Chapter 2. These parameters were previously used in MD simulations of carbon nanotubes in the presence of biomolecules [105], and were found to reproduce experimental results successfully, in terms of the relative positions of the nanotube and the biomolecule, where the difference between the experimental results and the simulation results was comparable to the uncertainty in the experimental measurement [105, 106]. Counterions were included with the charged amino acids to neutralize the net charge (sodium ions with glutamate and aspartate, and chlorine ions with arginine). The coordinates were then fed to the DFT/NEGF simulator Atomistix (ATK). In ATK, two-probe simulations were performed where the coordinates of the central region were those calculated from the MD simulations as explained above. The central region was sandwiched between two semi-infinite CNT electrodes of the same chirality as the nanotube in the central region.

The basis set used in the *ab initio* simulations can significantly affect the results, even qualitatively, as it was previously demonstrated in Chapter 3 and in [80, 107]. Therefore, a test with the (9,0) tube was first made, where the bare-tube simulations and the simulations with arginine were repeated using the double-zeta (DZ), double-zeta polarized (DZP), and single-zeta-polarized (SZP) basis sets. It was found that the DZP basis set predicts the largest relative current change due to the adsorption of the ARG dimer, and that the difference between the relative current changes predicted by the DZ and the SZP basis sets is not significant in the range of bias used. In addition, the DZ basis set predicts the total charge on the tube and the amino acid in excellent agreement with that predicted with the DZP basis set, whereas the predictions obtained using the SZP basis set are significantly different, as was previously demonstrated [80]. An accurate prediction of the total charge is particularly important for this study since charged species are being inspected as well as neutral ones. Hence, and since larger-radius tubes could not be simulated using the DZP basis set due to memory limitations, the DZ basis set was used throughout the simulations described hereunder even though this may underestimate the effect of the amino acid.

In addition, ATK uses periodic boundary conditions in the directions transverse to the transport direction, meaning that the simulation box is repeated indefinitely in the transverse directions. To assure that no significant interaction occurs between the actual simulation box and its repeated images, as was previously pointed out [108], the transverse dimensions of the simulation box were increased for each simulation until no significant change ($\sim 1\%$) in the calculated current was observed.

Finally, a screening region is introduced in ATK to isolate the central region from the electrodes to assure charge neutrality in the electrodes. This is because the electrodes are assumed to be extended infinitely in the transport direction, and the repeated images of the electrode are assumed to have the same charge distribution as the electrode cell in the actual simulation box. The screening-region length (SRL) was chosen as one period (four layers of atoms) of the tube between the central region and each of the electrodes. Then, the SRL was doubled for the (9,0) bare tube and the (9,0) tube with the adsorbed arginine; and no observable change in the electron density in the electrodes was found. In fact, the electron density in the electrodes in both cases was almost identical to an infinitely-long bare tube of the same chirality. Also, there was no significant change in the current/voltage characteristics as will be shown in the results below. Using a longer SRL for the larger tubes (especially the (15,0) and the (18,0) tubes) was not possible even with the DZ basis set due to memory limitations.

Therefore all simulations presented here were performed using a four-layer SRL.

4.3.2 Results and Discussion

From the MD simulations, each of the dimers was adsorbed on all the different nanotubes, except for those of glutamate and aspartate, which failed to be adsorbed on any of the tubes, and therefore were not considered in the DFT/NEGF simulations. The other amino acids settled at a distance of 0.25 nm to 0.29 nm from the surface of the tubes. The counterions settled at a distance more than 1.5 nm away from the surface of all the tubes and therefore were neglected in the DFT/NEGF simulations. It is worth noting that the MD simulations showed that the amino acid lay on the edge of the water shell around the nanotube in all cases where adsorption occurred. For hydrophobic amino acids, this is expected since both the amino acid and the tube are hydrophobic and will tend to aggregate together through hydrophobic interactions. For the hydrophilic amino acids, the results suggest that when the amino acid is close enough to the surface of the tube, the hydrophobic repulsion between the tube and the water molecules, combined with the attraction forces between the tube and the amino acid disrupts the solvation shell surrounding the amino acid.

The current (I)-voltage (V) characteristics of the (9,0) tube are shown in Figure 4.7 for the bare tube and for the same tube with an adsorbed dimer of each of the aromatic amino acids used. It is clear that in all the cases the current increases with bias, then virtually saturates until V exceeds E_G/q , where q is the electronic charge and E_G is the bandgap of the tube. When V exceeds E_G/q , the current starts to increase again with the applied bias. This indicates the onset of a new carrier transport mechanism (namely, band-to-band tunneling), as will be explained below in the transport mechanisms discussion. It is also clear that these adsorbed aromatic amino acids do not have any significant effect on the conductance of the tube. It is interesting to note that our results for the interaction between aromatic amino acids and semiconducting tubes (not shown here) demonstrate a clear change in the transmission coefficient of semiconducting tubes upon amino-acid adsorption. A similar change had been observed experimentally with other aromatic molecules [29], and had been attributed to charge transfer between the tube and the aromatic molecules. Although our calculations show that a similar charge transfer occurs between the aromatic amino acids and the semi-metallic tubes, it does not have the same effect as it has with the semiconducting ones. A further study is needed to explain

the reason behind this difference in response between the two types of tube.

Figure 4.8 shows the I-V characteristics of the (9,0) tube, both bare and with an adsorbed dimer of each of the neutral non-aromatic amino acids isoleucine and asparagine, as well as with an adsorbed dimer of arginine. Again, with the non-aromatic neutral amino acids, and the positively charged amino acid arginine, we observe the same trend of the current with increasing bias as mentioned above. We also notice that the effect of the adsorbed amino acid on the current is bias-dependent. ASN and ILE adsorption results in a small reduction in current when $V < E_G/q$, while it has no effect for higher bias levels. ARG induces a larger decrease in the current for $V < E_G/q$, but also causes a clear increase in the current when V exceeds E_G/q . The I-V characteristics of the (18,0) tube were also calculated in the presence of neutral amino acids (results not shown here), and again, no significant change in the current was observed. As for ARG, Figure 4.9 shows the I-V characteristics of the various tubes with and without an adsorbed dimer of this positively charged amino acid. It is evident that for all the tubes, the conductance ($G = I/V$) decreases upon the adsorption of the arginine dimer compared to the corresponding bare-tube current for $V < E_G/q$. When V exceeds E_G/q , the observed suppression of the current upon ARG adsorption starts to decrease, and eventually the current with the adsorbed amino acid becomes larger than the bare-tube current, indicat-

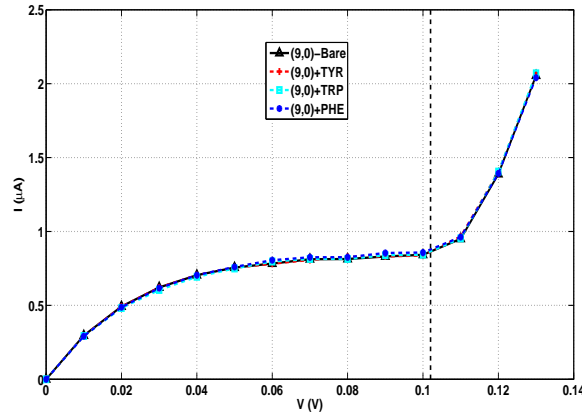


Figure 4.7: I-V characteristics for the bare (9,0) tube and the same tube with an adsorbed dimer of each of the aromatic amino acids TYR, TRP, and PHE. The vertical line indicates the bias value at which $V = E_G/q$.

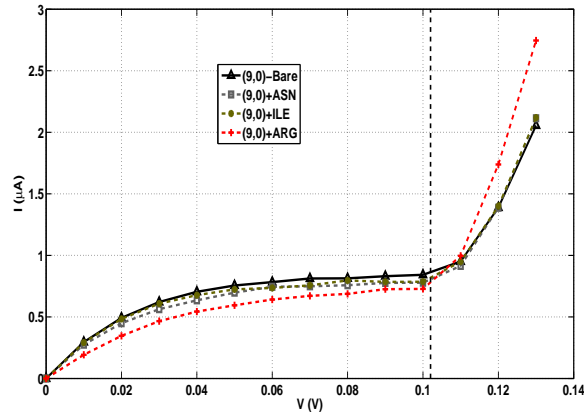


Figure 4.8: I-V characteristics for the bare (9,0) tube and the same tube with an adsorbed dimer of each of the neutral non-aromatic amino acids ASN and ILE, and the positively-charged amino acid ARG. The vertical line indicates the bias value at which $V = E_G/q$.

ing an increase in G . It is worth emphasizing here that increasing the SRL, discussed above in section 4.3.1, had no effect on the current of the bare tube in both bias ranges. For the tube with the adsorbed arginine, increasing the SRL had no significant effect in the first bias range ($V < E_G/q$), while in the second bias range ($V > E_G/q$), there was a small increase in the current when the SRL was increased compared to the shorter-SRL case, as can be seen in the bottom set of curves in Figure 4.9. Taking into account that in this range the current for the short-SRL case is already greater than that of the bare tube, we can see that using the shorter SRL in the simulations gives a slightly lower estimation of the change in the current upon arginine adsorption. We conclude that using the short SRL does not compromise the conclusions, while permitting the study of the larger tubes as explained in section 4.3.1.

The effect of ARG adsorption on the conductance of the various tubes is summarized in Figure 4.10. It is clear that the change in the current relative to the bare-tube case decreases with the increasing radius of the tube. This may be explained by the fact that the background current (*i.e.*, the current of the bare tube) is larger (at the same bias) for larger-radius tubes due to their smaller bandgap and, therefore, higher intrinsic carrier density. Therefore, among the semi-metallic tubes, which are expected to have a higher possibility for conductance modulation than their semicon-

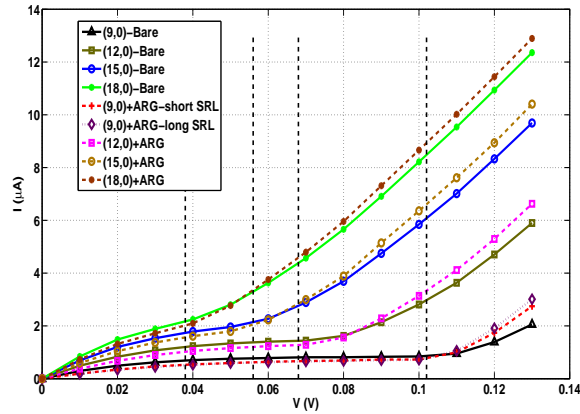


Figure 4.9: I-V characteristics for the bare tubes and for the tubes with an adsorbed dimer of arginine. From left to right, the vertical lines denote the bias value at which $V = E_G/q$ for the (18,0), (15,0), (12,0), and the (9,0) tubes, respectively.

ducting and metallic counterparts, those with smaller radii are expected to exhibit the larger responses to amino-acid adsorption.

Transport Mechanisms

Here, Figure 4.11 is introduced to offer an explanation for the features of the I-V characteristics. When the bias (in volts) is numerically lower than the bandgap (in electron volts), electrons can move from the conduction band in the left electrode to free states in the conduction band in the right electrode creating a left-to-right current (I_{LR}). Similarly, electrons in the conduction band of the right electrode can move to free states in the left electrode creating a right-to-left current (I_{RL}). I_{RL} , however, will be smaller than I_{LR} due to the energy barrier (qV) that the electrons moving from the right electrode to the left electrode encounter. The net flow of electrons creates what will be referred to as the intraband current (I_{IB}). As the bias increases, the energy barrier increases and therefore I_{RL} decreases until it vanishes, leading to the eventual saturation of the net current I_{IB} . As long as the bias is numerically less than the bandgap, electrons in the valence band of the left electrode cannot tunnel through to the right electrode as there are no available states at the corresponding energies on the right electrode. When the bias numerically exceeds the bandgap, however, free states in the conduc-

tion band of the right electrode become available for electrons in the valence band of the left electrode to tunnel into and contribute to a band-to-band-tunneling current (I_{BTB}). This tunneling current is the reason behind the sudden increase in the current when $V > E_G/q$. This is further confirmed in Figure 4.12, which depicts the transmission coefficient as a function of energy ($T(E)$) of the (9,0) tube at different bias points in the two bias regions described above. When the bias is 0.01 V (much less than E_G/q), there is no transmission probability for energies within the bandgap, which results in a zero transmission coefficient. When the bias exceeds E_G/q , on the other hand, we can see a sizeable transmission coefficient within the bandgap, which is associated with I_{BTB} as explained above. The same phenomenon is also observed for the (12,0), (15,0), and the (18,0) tubes, (the corresponding transmission coefficients are not shown here). This tunneling current may also explain the unexpectedly high current levels that were observed previously in similar simulations [109]. It is remarked here that although a first glance at Figure 4.12 may appear to indicate that the bandgap widens with increasing the bias, this is not actually the case. $T(E)$ represents the sum of the probabilities of transmission between the two electrodes for different eigenchannels. Since in the absence of tunneling no transmission can occur in the energy window between the quasi-Fermi levels of the electrodes,

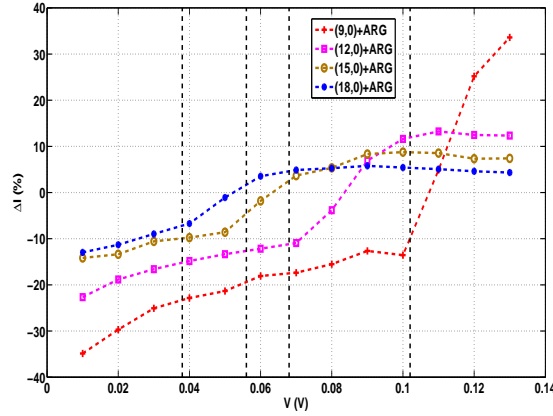


Figure 4.10: Relative change in the current compared to the current of the bare tubes upon ARG adsorption. From left to right, the vertical lines denote the bias value at which $V = E_G/q$ for the (18,0), (15,0), (12,0), and the (9,0) tubes, respectively.

the transmission coefficient in this window is essentially zero except for the energy values at which band-to-band tunneling is possible. It is worth noting that, in practice, fabrication of intrinsic CNTs with the Fermi level in the middle of the gap as shown in Figure 4.11 can be achieved through the dry-contact-transfer method [110]. For cases where the Fermi level lies inside the conduction band, the intraband current of the bare tube is expected to increase because of the larger number of carriers available in the conduction band. This may lead to a decrease in the relative change caused by the analyte before the onset of the tunneling. If the Fermi level lies inside the valence band, the opposite is expected to occur: the bare-tube intraband current is expected to decrease, and the effect of the analyte, in relative terms, should be greater. The tunneling current should not be affected in either case.

Mechanisms of Conductance Change

The changes in the current upon ARG adsorption are discussed here. When the bias is numerically less than the bandgap of the tube, the proximity of the charged amino acid to the nanotube disturbs the electrostatic potential in the central region. The irregularity of the potential causes quantum mechanical reflections that reduce the transmission probability between the two electrodes and therefore I_{IB} decreases.

For the range where $V > E_G/q$, the observed increase in the current can be understood from Figure 4.13. The charged amino acid increases the field locally, thus decreasing the effective width through which electrons should tunnel, as schematically shown in Figure 4.13, resulting in an increase in the tunneling probability and hence in I_{BTB} .

To justify the explanation above, the total current (I_{tot}) and I_{IB} were calculated for the various tubes with and without ARG, as well as the I_{BTB} component of the total current. The results are shown in Table 4.1 for the (9,0) and (12,0) tubes. Table 4.1 shows that the presence of ARG suppresses I_{IB} while enhancing I_{BTB} . A similar behaviour was also observed for the (15,0) and (18,0) tubes.

To further corroborate the suggested explanation, the electrostatic potential V_{ES} in the central region for the simulation with the bare (9,0) tube (CNT-bare) and the same tube with the adsorbed arginine (CNT-ARG) were calculated. A third simulation (CNT-ARG-bare) was also performed with the coordinates of the CNT atoms being identical to those in CNT-ARG, but with the atoms of the amino acid being omitted in the DFT/NEGF simulation. In other words, the amino acid atoms were included in the MD

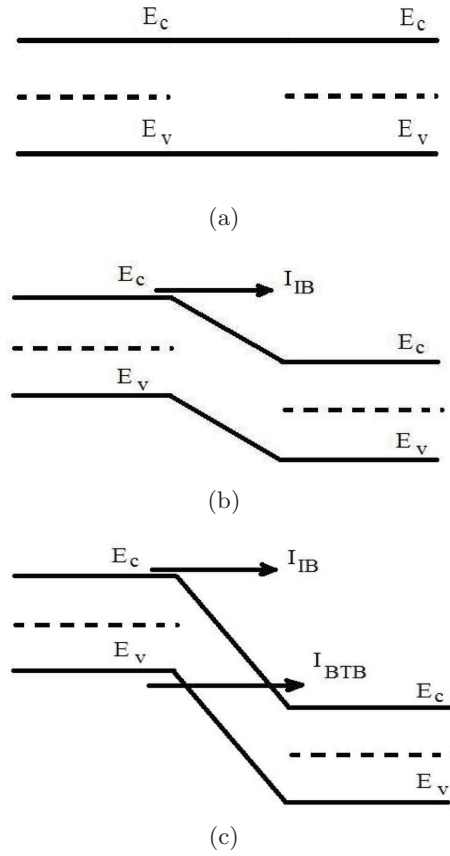


Figure 4.11: Schematic band diagram for the bare tube for (a) $V = 0$, (b) $0 < V < E_G/q$, and (c) $V > E_G/q$. The dashed lines depict the Fermi level or quasi-Fermi level in each of the contacts.

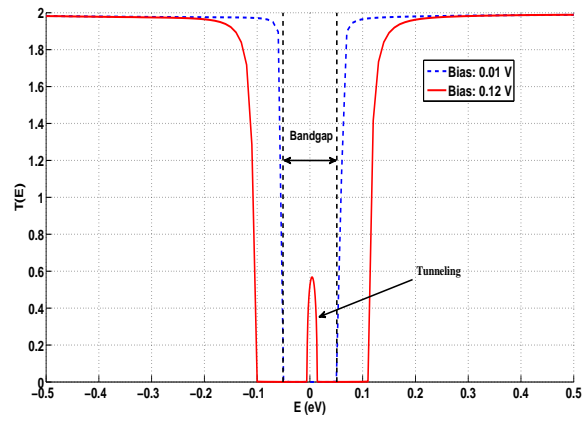


Figure 4.12: Transmission coefficient of the bare (9,0) at two bias points: 0.01 V and 0.12 V.

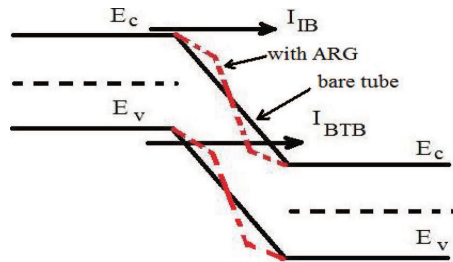


Figure 4.13: Schematic band diagram illustrating the effect of the adsorption of ARG on the electrostatic potential energy in the CNT for $V > E_G/q$.

simulations but not in the subsequent DFT/NEGF simulations for CNT-ARG-bare. The purpose is to examine whether the suggested irregularities in the potential are a result of the tube deformation due to van der Waals interaction forces with the amino acid, or whether electrostatic interactions are the actual reason for those irregularities. Figure 4.14(b) shows the difference in V_{ES} (ΔV_{ES}) between CNT-ARG and CNT-bare as well as between CNT-ARG-bare and CNT-bare along the line directly under the adsorbed dimer as illustrated in Figure 4.14(a). We can see that for both CNT-ARG and CNT-ARG-bare, there is a change in the electrostatic potential. The change in the case of CNT-ARG, however, is significantly greater near the two extremities of the central region, and decreases near the middle of the central region to become almost identical to that associated with CNT-ARG-bare. This can be explained as follows: the charge on the dimer resides on the guanidino groups on each of the arginine residues [100] as confirmed by Mulliken population analysis at the end of the DFT/NEGF simulation. The

Table 4.1: Different components of the current for the (9,0) and (12,0) tubes with and without the adsorbed dimer of arginine, and at the two bias points 0.01 V and 0.12 V. Currents less than 1 nA were considered to be exactly zero.

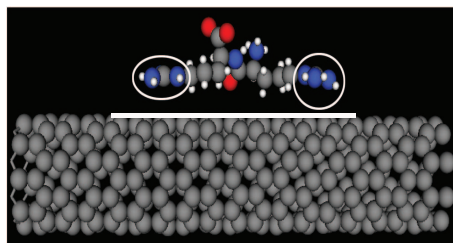
Structure	I_{IB} (nA)	I_{BTB} (nA)	I_{tot} (nA)	$\frac{I_{BTB}}{I_{tot}}$ (%)
(9,0)-bare: 0.01 V	295.77	0.00	295.77	0.00
(9,0)-ARG: 0.01 V	202.30	0.00	202.30	0.00
(9,0)-bare: 0.12 V	922.80	465.90	1388.70	33.55
(9,0)-ARG: 0.12 V	823.25	826.25	1649.50	50.09
(12,0)-bare: 0.01 V	492.48	0.00	492.48	0.00
(12,0)-ARG: 0.01 V	380.90	0.00	380.90	0.00
(12,0)-bare: 0.12 V	1540.90	3165.60	4706.50	67.26
(12,0)-ARG: 0.12 V	1428.30	3865.20	5293.50	73.02

guanidino groups stretch over the tube near the two extremities of the central regions as shown in Figure 4.14(a). Therefore, the effect of the charge is more pronounced near the guanidino groups and decays as we move towards the middle of the central region. A similar calculation was conducted along a line at the bottom of the tube (on the opposite side of the adsorption site of the dimer), and ΔV_{ES} was identical for both CNT-ARG and CNT-ARG-bare along that latter line. The results show that both the change in the coordinates of the tube due to van der Waals forces, and the electrostatic interactions due to the charge on the amino acids contribute to ΔV_{ES} , and result in local disturbances in the electrostatic potential. The similarity in the general shape of the two curves in Figure 4.14(b) indicates that this general shape is caused by the change in the coordinates, not by the electrostatic interactions. The electrostatic interactions, however, induce a significant local increase in ΔV_{ES} , leading to further local disturbances in the electrostatic potential. The local potential disturbances result in quantum mechanical reflections, thus decreasing the transmission probability between the two electrodes, and consequently decreasing the conductance of the tube.

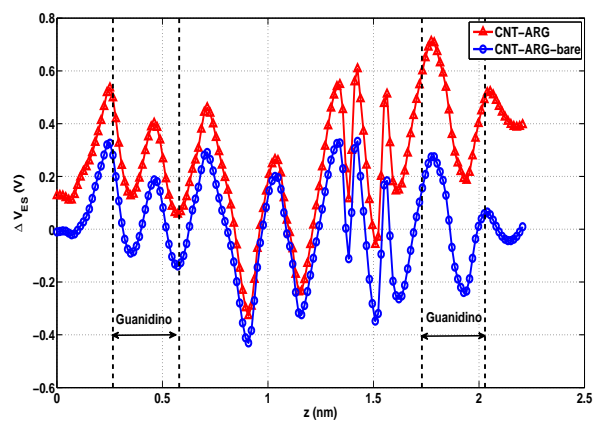
For the increase in the tunneling, the local density of states (LDOS) is shown at an energy of 0.0 eV (same reference energy as in Figure 4.12), and a bias of 0.12 V, on a cut-plane perpendicular to the transport direction as shown in Figure 4.15. We can see a clear increase in the LDOS upon ARG adsorption in comparison with the bare tube. An increase in the LDOS was observed all along the tube, but the LDOS closer to the amino acid (upper part of Figure 4.15(c)) was higher than away from the adsorbed amino acid. It is noted that the maximum value of the LDOS is $0.03006 \text{ \AA}^{-3} \text{ eV}^{-1}$ for the bare tube compared to $0.1236 \text{ \AA}^{-3} \text{ eV}^{-1}$ with ARG. The increase in the LDOS is in agreement with the lowering of the potential energy and the consequent increase in the tunneling probability suggested above.

It is to be noted that at such a short length of the device, high electric fields may arise and there may be a possibility of breakdown, specially in the band-to-band-tunneling operation region described above. It is demonstrated here that this possibility is not of serious concern for the simulated structures described above. The breakdown of carbon nanotubes has been attributed to heating associated with phonon-electron scattering [111, 112]. Due to ballistic transport in the short tubes presented in this work, and to the fact that they are shorter than the phonon mean-free path [113, 114], such a scattering is impossible. Also, a value of the field close to that reported here was reported in [113], and no breakdown was observed. Therefore, the possibility of breakdown is excluded.

Two further simulations similar to CNT-ARG-bare described above were

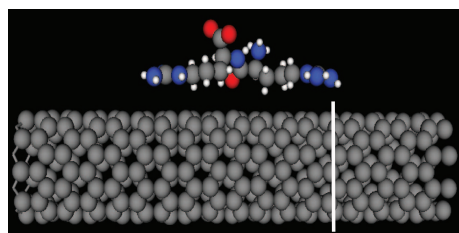


(a)

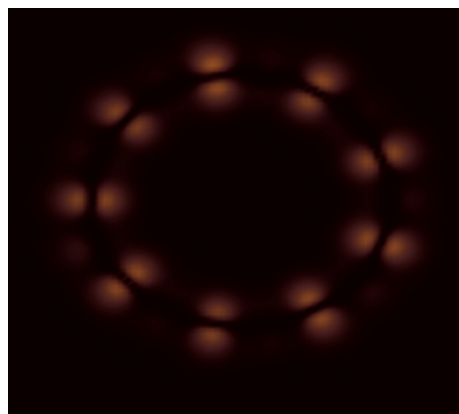


(b)

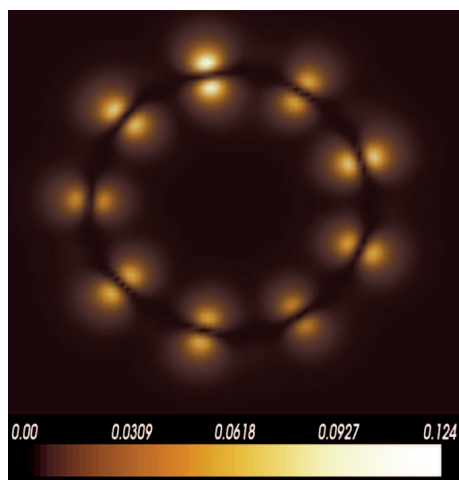
Figure 4.14: Difference in the electrostatic potential in the central region between CNT-ARG and CNT-ARG-bare on one hand, and CNT-bare on the other hand. The difference is shown in (b) along the line shown in (a). The ellipses in (a) denote the guanidino groups.



(a)



(b)



(c)

Figure 4.15: LDOS at an energy of 0.0 eV, and a bias of 0.12 V, in units of $\text{\AA}^{-3} \text{eV}^{-1}$ on a cut-plane perpendicular to the transport direction at the line shown in (a) for (b) bare tube, (c) tube with adsorbed arginine.

performed, but with ASN and ILE instead of ARG, as these amino acids resulted in a visible (though small) effect on the I-V characteristics of the (9,0) tube. These simulations will be referred to as CNT-ASN-bare and CNT-ILE-bare. The purpose is again to examine if the change in the current is due to changes in the coordinates of the CNT atoms resulting from van der Waals forces between the tube and the amino acid, or if other effects (*e.g.*, Coulombic interactions) are more important in changing the current. The results are shown in Figure 4.16 together with the results for CNT-bare, CNT-ARG, and CNT-ARG-bare for comparison. The simulations that include the atoms of ASN and ILE in both MD and DFT/NEGF simulations will be referred to as CNT-ASN and CNT-ILE, respectively. The results for CNT-ARG-bare compared to CNT-bare show that the current still changes, although the changes observed with CNT-ARG are clearly much more pronounced. This suggests that the potential disturbances due to the electrostatic interactions discussed above are the main reason behind the changes in the current, and that those disturbances caused by the change in the coordinates of the tube atoms play only a minor role. For the neutral amino acids ASN and ILE, the results of CNT-ASN-bare and CNT-ILE-bare are very close to CNT-ASN and CNT-ILE. This shows that the van der Waals interaction forces between the amino acids and the tube, and the resulting coordinate changes of the tube atoms, are the reason for the observed small conductance changes in this case. The aromatic amino acids had virtually no effect at all on the conductance of the tube. This is because of two reasons: the first one is that they are neutral and therefore have no Coulombic interactions, and the second one is that aromatic amino acids adsorb on the nanotubes through π -stacking, *i.e.*, the aromatic ring stacks over the rings already present in the tube. Therefore, the changes in the coordinates of the tubes are minimal and do not cause any significant effect on the conductance of the tube.

4.3.3 Effect of Amino-Acid Vibration in Water

The simulations above describe the interaction of the different amino acids with the CNTs after 2 ns of MD simulations in water. In this section, the above simulations were repeated at different times to assess the extent of the fluctuations in the results due to the vibration of the amino acid in water. The amino acid arginine was chosen as it was the one that resulted in the largest effect on the conductance of the nanotubes. The simulations of arginine with the (12,0) tube were extended to 3 ns, and then the DFT/NEGF simulations were repeated at 1.5 ns, 2.5 ns, and 3 ns. The results are shown

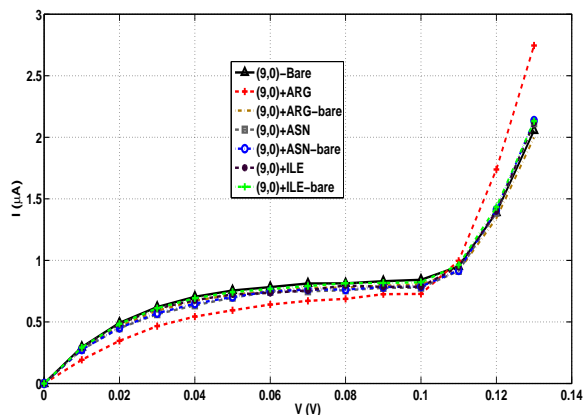


Figure 4.16: I-V characteristics for CNT-ARG-bare, CNT-ASN-bare, CNT-ILE-bare. The results for CNT-ARG, CNT-ASN, CNT-ILE, and CNT-bare are also included for comparison.

in Figure 4.17, and the changes in the current compared to the bare-tube case are shown in Figure 4.18. The current of the bare tube remained essentially unchanged at different times and therefore only one set of data of the bare tube is shown. For the tube with the adsorbed amino acid, and in the bias region where transport is dominated by the intraband current, the differences in the current at different times are small, and they are all clearly lower than the bare-tube current. In the tunneling-dominated region, however, there are significantly larger fluctuations in the current, though it is at all times clearly distinguishable from the current of the bare tube. This is consistent with the discussion above, since the tunneling current is sensitive to the tunneling width, which is influenced by the proximity of arginine as explained above. Therefore, small variation in the position of the arginine dimer that result in corresponding changes in the effective tunneling width will eventually have a noticeable effect on the tunneling current.

4.3.4 Repeatability of the Results

The results of MD simulations may differ from one run to another. The reason is that the initial velocities are chosen randomly, and also in GROMACS the exact Fast Fourier Transform algorithm employed in GROMACS is chosen depending on the load on the processor where the calculation is carried out, which may differ from run to run. In addition, the initial separation be-

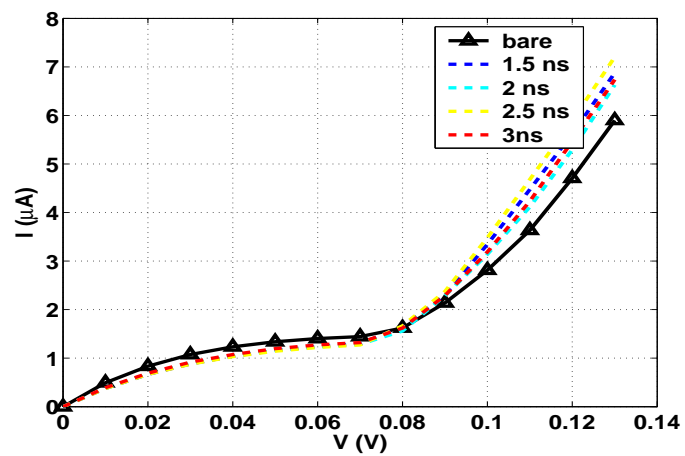


Figure 4.17: I-V characteristics for (12,0) tube with an adsorbed dimer of arginine at different times of the MD simulation.

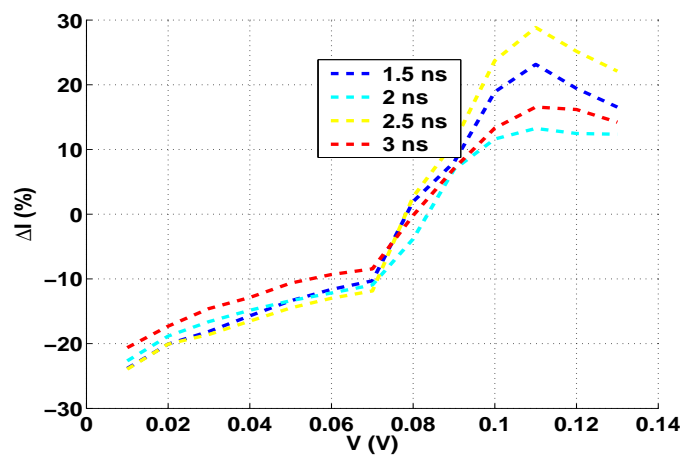


Figure 4.18: The relative change in the current for the (12,0) tube with an adsorbed dimer of arginine at different times of the MD simulation, compared to the bare-tube current.

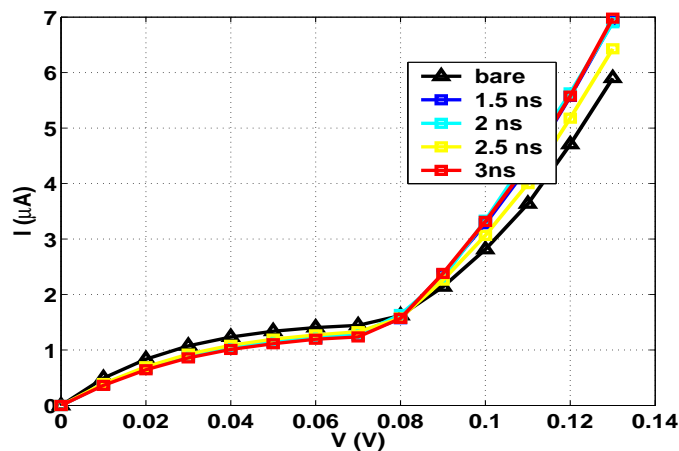


Figure 4.19: I-V characteristics for (12,0) tube with an adsorbed dimer of arginine at different times of the MD simulation with an initial separation of 0.7 nm between the dimer and the surface of the tube.

tween the amino acid and the tube may have been fortunate enough for the adsorption to occur. Therefore, to ensure the repeatability of the results, the whole flow of simulations was repeated with the same initial conditions of MD, and with the initial separation between the ARG dimer and the (12,0) tube (Δd) increased to 0.7 nm. The results for the repeated simulations with exactly the same initial conditions were very close to those presented above for all time points. The results for the simulations with $\Delta d = 0.7$ nm are shown in Figure 4.19. It can be seen that the current values fall in the same range as those in Figure 4.17. Δd was increased to 0.9 nm and 1.3 nm. The orientation and relative positions of the amino acid atoms and the CNT atoms were very close to those observed with $\Delta d = 0.5$ nm and $\Delta d = 0.7$ nm for times greater than 1.5 ns (between 2.5 Å and 3 Å in all cases). The calculations above give an indication of the repeatability of the results. The relative changes in the current are shown in Figure 4.20. Comparing these results to those shown in Figure 4.18, it can be seen that the relative changes in both cases are in the same range, and clearly distinguishable from the bare-tube current.

4.3.5 Effect of the Length of the Nanotube

To assess the effect of the length of the nanotube on the results, the simulations above were repeated for 8.8 nm (9,0) and (12,0) tubes, each with

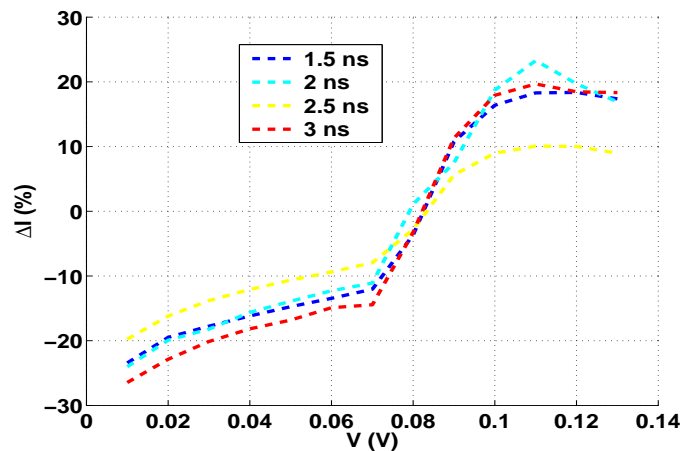


Figure 4.20: The relative change in the current for the (12,0) tube with an adsorbed dimer of arginine at different times of the MD simulation, and with an initial separation of 0.7 nm between the dimer and the surface of the tube, compared to the bare-tube current.

a dimer of arginine. The results for the (12,0) tube are illustrated in Figure 4.21 and the corresponding relative changes in the current are shown in Figure 4.22. The results exhibit the same behaviour observed for the shorter tubes discussed above. The bare-(9,0) current illustrated in Figure 4.23, on the other hand, shows significant fluctuations with time that were not observed in the shorter-tube results shown. This is due to the higher possibility of the suspended tube atoms oscillating (*i.e.*, their coordinates change significantly over time) as the tube grows longer, as explained in section 4.2.2. This is confirmed by calculating the displacements of the different atoms of the nanotube as compared to their initial unperturbed positions for both the 2.2 nm tube and the 8.8 nm tube. The mean displacement for the former (compared to the initial positions) is 0.09 nm compared to 0.13 nm for the latter. Larger tubes of the same length could not be simulated due to excessive memory requirements. The larger displacements themselves cause larger quantum mechanical reflections than for the shorter tubes. However, we would expect larger-radius tubes to be less susceptible to the oscillations explained above, which is supported by the I-V characteristics of the (12,0) tube shown in Figure 4.21. Also, in the case of a larger number of adsorbed molecules or larger molecules, the effect of the adsorbed analyte would still be noticeable.

It is worth mentioning that the shortest carbon nanotubes that have been

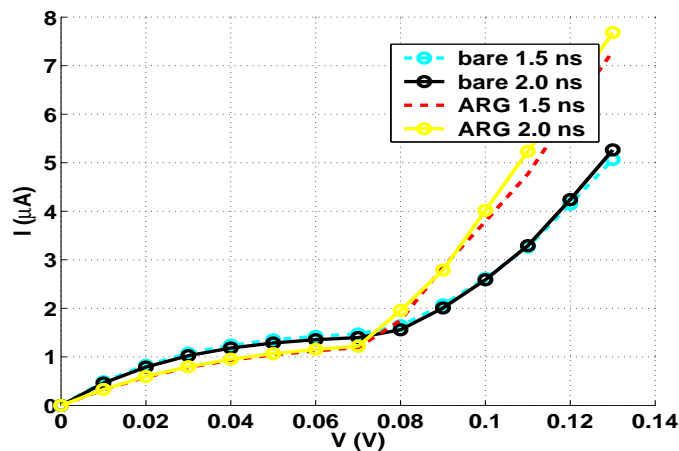


Figure 4.21: I-V characteristics for the 8.8 nm (12,0) tube with an adsorbed dimer of arginine at different times of the MD simulation with an initial separation of 0.5 nm between the dimer and the surface of the tube.

synthesized consisted of a single armchair carbon “nanohoop” [115]. This suggests that, in principle, the tube lengths studied here can be synthesized.

4.3.6 Effect of the Position of the Adsorption Site

The discussion above corresponds to an adsorption site near one of the electrodes of the (9,0) tube as shown in Figure 4.24(a). The simulations were repeated after translating the arginine dimer to the middle of the nanotube as shown in Figure 4.24(b). The results in Figure 4.25 show a clear current increase in the tunneling-dominated region. This is because when the arginine is adsorbed near the middle of the tube, the tunneling width would be smaller than that when the dimer is adsorbed nearer to one of the electrodes as illustrated in Figure 4.26.

For the bias region before the onset of the band-to-band tunneling, things are more complicated. We notice that the change in the current for the adsorption near the middle of the tube is negligible. This can be explained by inspecting Figure 4.27. The difference between the energy of the carrier and the potential energy disturbances depends on the position of the adsorption site. Since the transmission probability when the carrier energy exceeds that of the barrier/well oscillates with energy, we would expect the current to oscillate as the position of the adsorption site changes, including full transmission (unless when the carrier energy is significantly smaller than that of

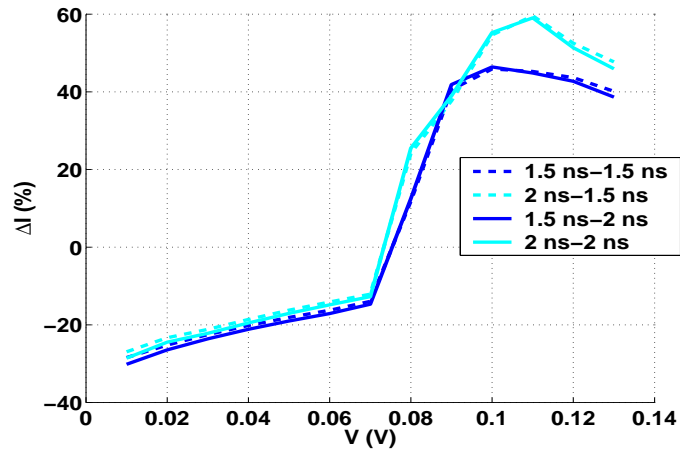


Figure 4.22: The relative change in the current for the 8.8 nm (12,0) tube with an adsorbed dimer of arginine at different times of the MD simulation with an initial separation of 0.5 nm between the dimer and the surface of the tube. The dotted line show the relative difference compared to the bare-tube current at 1.5 ns, while the continuous lines show the relative difference compared to the bare-tube current at 2 ns

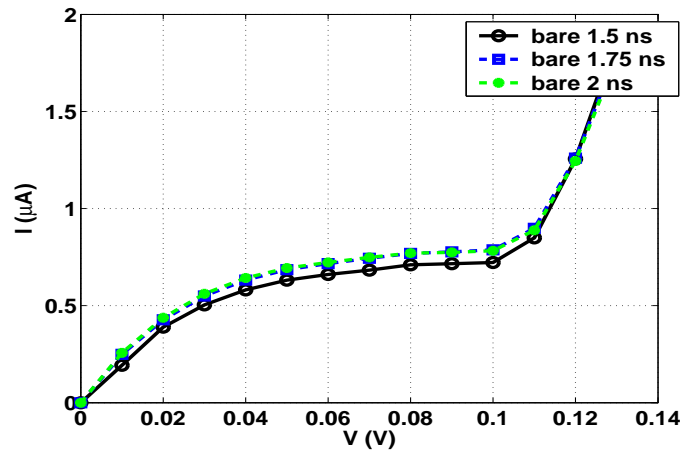


Figure 4.23: I-V characteristics for the 8.8 nm (9,0) bare tube at different times showing larger fluctuations than with the shorter tube.

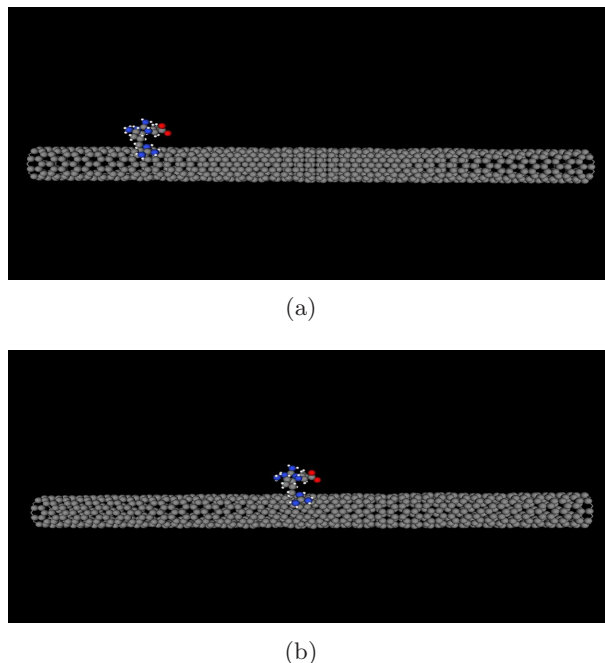


Figure 4.24: 8.8 nm (9,0) tube with an arginine dimer adsorbed (a) near one of the electrodes, (b) near the middle of the tube.

the barrier, where a significant suppression is expected). Therefore, for this region, we conclude that the position of the adsorption site has an important effect on the response of the tubes to the adsorption of biomolecules, and that a specific study for each target analyte is needed to assess which position sites would result in a significant conductance modulation.

4.3.7 Connection with Experimental Results and Previously Suggested Sensing Mechanisms in the Literature

In this section, the results and conclusions presented in this chapter are used to explain the experimental results summarized in Chapter 1. As explained in section 4.3.2, a charge transfer has been observed between the nanotube and the amino acids. This charge transfer may explain the results of [23] for the bare tube where a shift in the current characteristics is observed, and it conforms to the explanation suggested by the authors. When the nanotube is coated with biotin, however, our results rule out the geometric deforma-

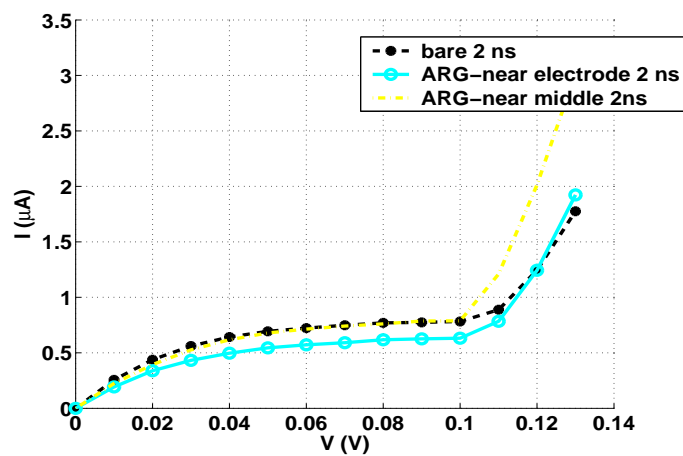


Figure 4.25: I-V characteristics corresponding to the simulated structures shown in Figure 4.24.

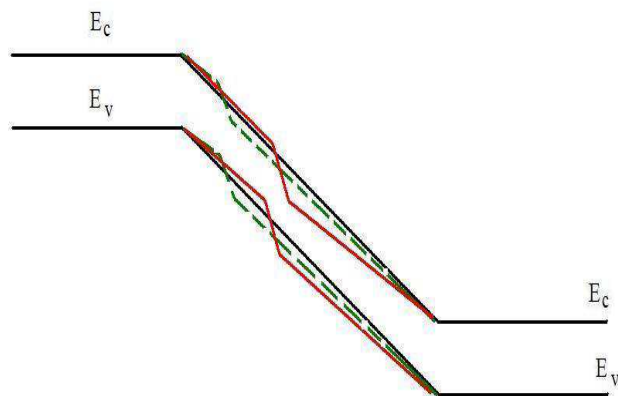


Figure 4.26: Band diagram illustrating the cases of adsorption near the electrode (green dotted line) and near the middle of the tube (red line). The black line shows the case for the bare tube.

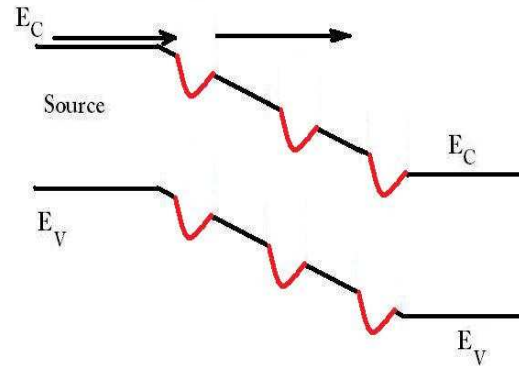


Figure 4.27: Band diagram illustrating the effect of the position of the adsorption site on the response of the nanotube in the region before the onset of the tunneling current. The red lines show the disturbance in potential energy due to the presence of a charged species near the surface of the tube.

tions as an important source of the current suppression upon streptavidin-biotin binding. We suggest that a change in the local charge distribution in the streptavidin-biotin system may have been the actual reason behind the observed decrease in the conductance of the tube. It is not quite clear whether the change in the charge of streptavidin upon binding to biotin is due to charge exchange with biotin or to conformational changes in streptavidin [116, 117]. It is known, however, that the binding process results in localized charged centres in the biotin-streptavidin system [118, 119]. We suggest the possibility that these localized centres affect the tube in such a way that the energy disturbances are similar to those shown in Figure 4.28, *i.e.*, the valence band edge decreases significantly, and no large increases in the conduction-band edge occur. CNTFETs with metallic contacts exhibit ambipolar conduction where holes dominate the conduction for gate voltages (V_G) less than half the drain voltage (V_D), while electrons dominate the conduction when $V_G > V_D/2$ [120]. Since the energy of at least some of the injected holes is less than the barrier induced by the potential energy disturbances caused by the biotin-streptavidin binding, the transmission of these holes will be quite significantly reduced, leading to the observed decrease in the current in the hole-dominated bias region. On the other hand, the energy of electrons is higher than the disturbed potential energy. Therefore, although the changes in the potential energy still result in quantum

mechanical reflections, these reflections are smaller than if the energy of the carrier is less than that of the barrier, and the transmission of electrons is not significantly changed in comparison to that of holes. This may explain the small change in the current in the electron-dominated region of bias, compared to that in the hole-dominated region. We suggest that the same mechanism (electrostatic interactions) is responsible for the detection of albumins, which have a high content of charged amino acids, and a low content of neutral ones [121]. It is worth noting that in the discussion above, a general explanation of the results is provided. For the particular situation shown as an example in Figure 1.6 [23], consideration should also be given to the effects on the nanotube of streptavidin-biotin binding and the presence of a polymer coating.

4.3.8 Conclusion

In this section, it was demonstrated that short semi-metallic carbon nanotubes show a clear change in conductance in response to adsorption of the positively charged amino acid arginine, while neutral aromatic and non-aromatic amino acids have little effect on the conductance of such tubes. It was also shown that these tubes exhibit two different transport mechanisms depending on the applied bias: tunneling current becomes a significant component of the total current when the applied bias (in volts) numerically exceeds the bandgap of the tubes (in electron volts). The effect of arginine on the conductance of the tubes is also dependent on the applied bias. When the bias is numerically lower than the bandgap of the tube, an amino-acid-induced disturbance of the electrostatic potential causes quantum mechanical reflections that decrease the conductance of the tube, while at higher bias levels, the tunneling probability increases due to the presence of arginine. The results demonstrate that short semi-metallic tubes show a high selectivity towards charged species, and that they may be useful as biosensors.

The interaction mechanisms between the amino acids and the nanotubes were thus elucidated. The results rule out the geometric deformations as a major source of conductance modulation in carbon nanotubes, and reveal the electrostatic interactions with the tube as the primary cause behind the conductance suppression observed upon analyte adsorption.

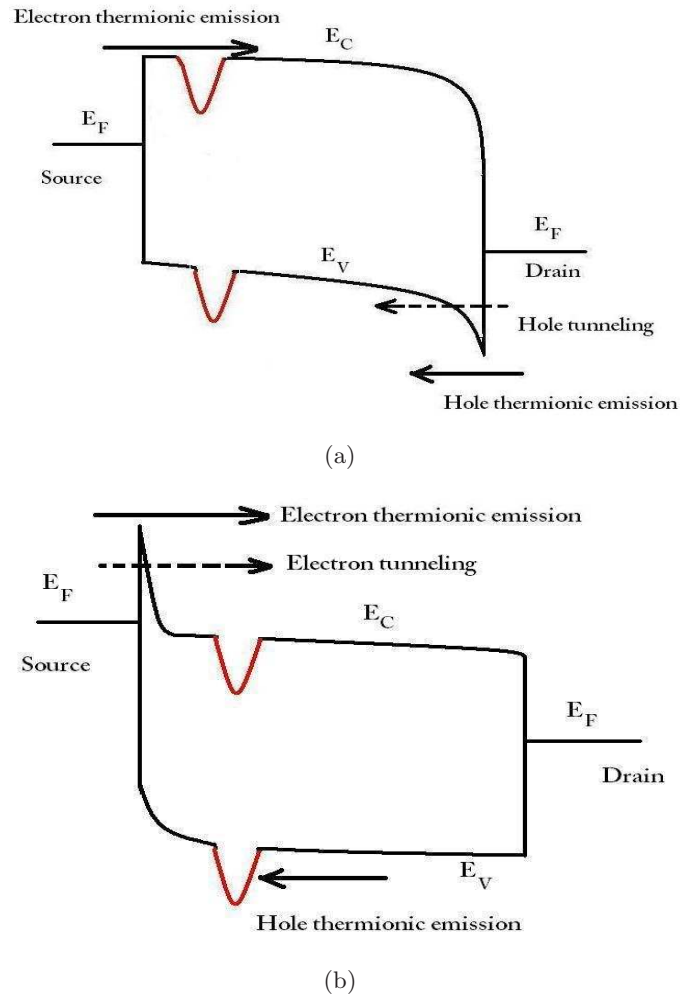


Figure 4.28: Band diagram showing the effect of the presence of a localized charge centre near the surface of a nanotube acting as a CNTFET channel, (a) $V_G < V_D/2$, (b) $V_G > V_D/2$. The red lines show the disturbance in potential energy due to the localized charge centre.

4.4 Metal-Induced Gap States and the Adsorption near Metallic Electrodes

In this section, the effect of the adsorption of biomolecules on the nanotube in the proximity of metallic electrodes is discussed [108].

4.4.1 Simulation Flow

The basic simulation procedure is summarized below, and the specific simulated structures in this section are described. First, classical molecular dynamics (MD) simulations were performed for a (10,0) CNT in an aqueous environment (pH 7.0) containing 40 dimers of each of two amino acids: isoleucine (ILE) (a neutral amino acid with a hydrophobic side-chain) and asparagine (ASN) (a neutral amino acid with a hydrophilic side-chain). The MD simulations were carried out using the package GROMACS with the AMBER port. Forty dimers were used to increase the probability of adsorption. The simulation time was 6 ns. The minimum distance between the dimers and the nanotube was calculated using GROMACS to be about 0.25 nm for each amino acid. One of the nearest dimers was then chosen from each of the ASN and ILE cases for use in the DFT/NEGF simulations. To improve the time to convergence, the simulation space was reduced by considering only the residue nearer to the tube of each dimer, *i.e.*, the one that should have the more significant effect on the tube. The residue was properly terminated to simulate a molecule of the corresponding amino acid. The DFT/NEGF simulations were carried out using the Atomistix package within the local density approximation (LDA). A single-zeta basis set was used because of the excessive memory required by the metallic aluminium electrodes. The simulated systems consisted of a (10,0) CNT forming a sensing region of a length of 0.85 nm, which was sandwiched between two semi-infinite aluminum electrodes. Each of the adsorbed amino acids was positioned as shown in Figure 4.29.

4.4.2 Results

Figure 4.30 shows the calculated transmission coefficient (T) for the simulations described above. The energy reference is at the Fermi energy. It is clear that the tube exhibits a rather metallic behaviour: there is no bandgap, even though (10,0) nanotubes are semiconductors with a sizeable gap (~ 1 eV). Evidently, the evanescent states associated with electron injection from the contacts persist throughout this short length of tube. Transmis-

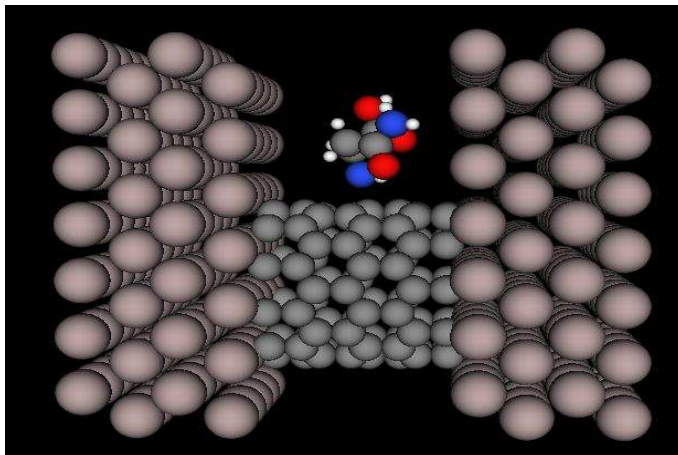


Figure 4.29: Simulated structure showing a molecule of asparagine.

sion in such a short tube is attributed primarily to these metal induced gap states (MIGS) [122, 123]. The Fermi level lies at the mid-gap, and the states contributing to the conduction (contributing states) have a range of energy of about $\pm 8kT$ (where kT is the thermal energy), which corresponds to ± 0.2 eV in our case (room temperature). This indeed is inside the region of the MIGS as can be seen from Figure 4.30. The I-V characteristics are also illustrated in Figure 4.31. The results of ILE and ASN are almost identical, and only those of ILE are shown for clarity. It is worth noting here that the effect of the box size can indeed have a significant impact on the results. To show that, the simulations were repeated for a smaller electrode cell as shown in Figure 4.32. Although the results of ILE are not much affected, the results of ASN differ significantly as shown in Figure 4.33. The observed increase in the current is attributed to interaction with the image simulation cells imposed by the periodic boundary conditions as explained in Chapter 2.

4.4.3 Conclusion

In this section, it was shown that metallic electrodes can inject midgap-induced states rendering tubes that are otherwise non-zero-bandgap tubes fully metallic. This suggests that adsorption near the metallic electrodes may go undetected by the nanotube.

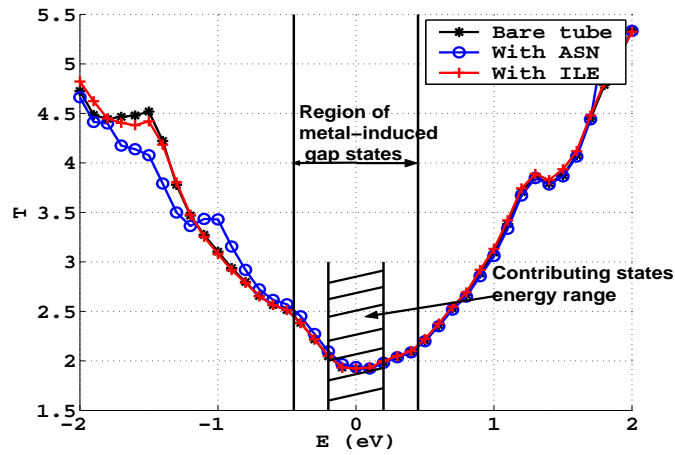


Figure 4.30: Transmission coefficient (T) as a function of energy (E) at equilibrium.

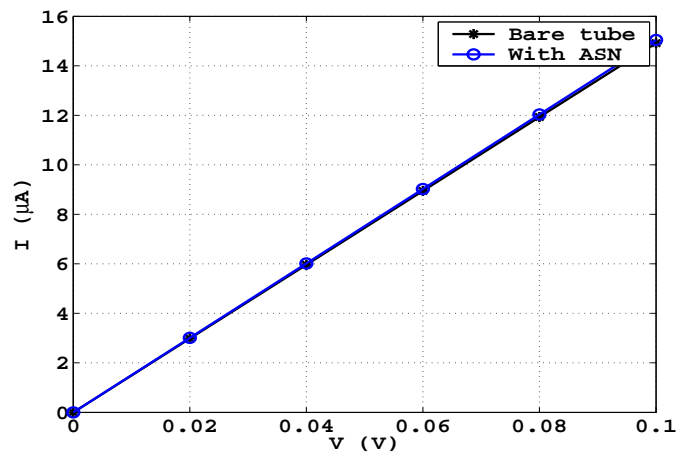


Figure 4.31: I-V characteristics for the simulated structures. The results for ILE were very close to the bare-tube case and were omitted for clarity.

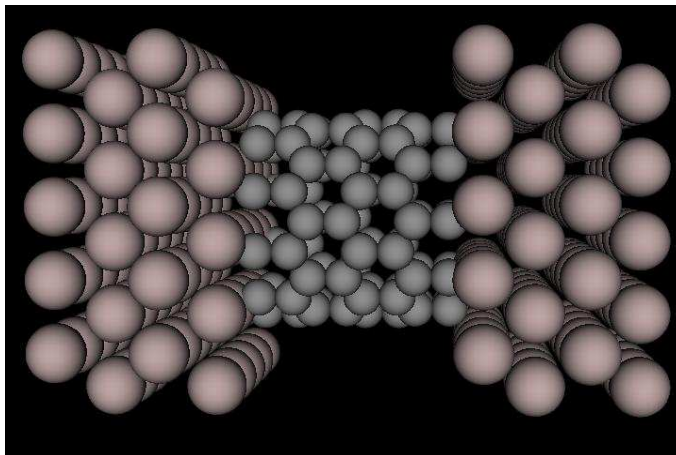


Figure 4.32: Simulation box with smaller dimensions.

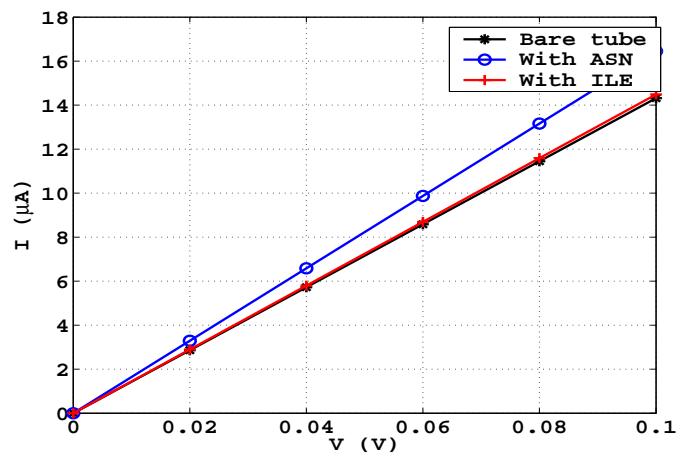


Figure 4.33: I-V characteristics for the simulated structures using a small simulation box. Erroneous results of asparagine are obtained showing the importance of the proper choice of the simulation box dimensions.

Chapter 5

Conclusions

In this thesis, the interaction between different amino acids and carbon nanotubes was studied using molecular dynamics and density functional theory/non-equilibrium Green's function simulations. Different amino acids were investigated, representing charged amino acids, neutral aromatic amino acids, and neutral non-aromatic amino acids. Both amino acids with hydrophobic side chains and amino-acids with hydrophilic side chains were included in the study.

General guidelines for the choice of the different parameters for these simulations have been established, in particular the choice of the basis set in the DFT/NEGF simulations. The mechanisms of interaction between carbon nanotubes and amino acids were elucidated. The interaction mechanisms can explain the experimental results observed in the literature, and some of the previously suggested sensing mechanisms could be ruled out. The interaction mechanisms were used to provide general guidelines for the design of carbon-nanotube-based biosensors. Finally, the effect of amino-acid adsorption on the electrical conductance of carbon nanotubes in a two-terminal configuration was studied. It was demonstrated that semi-metallic carbon nanotubes in particular have a high potential to be used as biosensors in such a configuration. The effect of the length and chirality of the tubes on their response to amino-acid adsorption was examined. Also, the effect of the electrodes and the adsorption site was investigated.

5.1 Contributions

The following contributions were made:

1. Establishment of rules for the choice of the basis sets for DFT/NEGF simulations of carbon nanotubes. It was shown that a polarized basis set is necessary for simulations of very-small-radius non-armchair nanotubes (≤ 0.6 nm). A non-polarized basis set was demonstrated to lead to qualitatively and quantitatively erroneous conclusions. A single-zeta basis set was found to be adequate for low-bias simulations

of armchair tubes, with the exception of the (2,2) tube, for which polarization should be included to get the near-zero-bias conductance and to capture the metallic behaviour of this tube. For zigzag tubes, it was found that the choice of the basis set depends on both the diameter and the chirality of the tube. It was also shown that the basis-set choice is closely interconnected with the length of the electrode-cell used, where a more complete basis set is more likely to necessitate a longer electrode to prevent interactions between non-neighbouring electrode cells. It was demonstrated that a poor choice of the electrode length can lead to erroneous conclusions regarding the bandgap and the transmission coefficient of the tube.

2. Demonstration of the fact that the (2,2) armchair tubes are metallic (in contradiction to previous calculations in the literature) and that the hybridization of the p - and d -orbitals in these tubes (and other very-small-radius tubes) plays an important role in determining their metallicity.
3. Demonstration of the fact that van der Waals forces are the main forces responsible for the adsorption. Hydrophobic interactions were shown to accelerate the adsorption process, though they are not necessary for it to occur. This is in line with the observed non-specific binding of proteins to carbon nanotubes, and emphasizes the need for functionalization to ensure specific binding.
4. Armchair tubes were shown to be highly insensitive to the adsorbed analytes.
5. Very-small-radius carbon nanotubes were shown to be inadequate as sensors in an aqueous environment. This was explained by the noticeable fluctuations in their conductance as a response to the motion of the atoms following immersion in water. These fluctuations were found to be comparable to the conductance changes induced by the analytes, and therefore the effect of analyte adsorption cannot be distinguished from that of the vibration in water.
6. The mechanisms of interaction between the semi-metallic tubes and amino acids were elucidated. The conductance change was found to be bias-dependent. In the short semi-metallic tubes studied in this thesis, and for the bias range where the bias (in V) is numerically less than the bandgap (in eV), the conductance change is caused by quantum mechanical reflections due to local disturbances of the electronic

charge. When the bias numerically exceeds the bandgap, the band-to-band tunneling current becomes an important component of the total current. In this bias range, the change in conductance is primarily through tunneling-width modulation. The results show that the changes in the atomic coordinates of the nanotubes upon amino-acid adsorption play a minor role in the sensing process, and that electrostatic interactions are the key factor controlling the conductance changes of the tube. In addition, it was demonstrated that the position of the adsorption site can affect the response of the tube to analyte adsorption. This was explained to be the result of a higher tunneling-width modulation for adsorption sites near the middle of the tube as compared to adsorption sites closer to the electrodes. For the bias region before the onset of band-to-band tunneling, however, there is no general rule relating the position of the adsorption site to the change in conductance due to analyte adsorption. The nanotube response in the tunneling-dominated region is generally larger than in the region before the onset of tunneling. Therefore, it is suggested that, to benefit from the tunneling-width modulation large response to the analytes in short tubes, regions of the tube close to the electrodes be covered (*e.g.*, by Poly(methyl methacrylate) (PMMA)) in order to ensure the adsorption close to the middle of the tube. For tubes much longer than those simulated in this thesis, suspended tubes may be susceptible to atoms oscillating, which may cause fluctuations in the current larger than those reported in this thesis, especially in the bias range where the bias is numerically less than the bandgap. To avoid this, the tube may be fabricated on a supporting substrate. Also, larger-radius tubes would be recommended as they are less prone to the oscillation problem. For the bias region where band-to-band tunneling becomes important, and as long as the length of the tube allows this type of tunneling to occur, a large conductance change is still expected to be observed. It is worth noting that carbon nanotubes as short as carbon nanohoops have been successfully synthesized, showing that the lengths of the tubes where the band-to-band tunneling can be observed are possible in practice.

7. It was shown that the metal-induced gap states injected from metal electrodes into the tube cause the adsorption near metallic electrodes to have negligible effect on the conductance of the tube.
8. It is suggested that semi-metallic carbon nanotubes have the potential

to be used to selectively detect charged analytes. It was found that these tubes show little change in the electrical conductance upon adsorption of non-charged analytes, while, for charged ones, a noticeable change in the conductance was observed. Since the tubes exhibit non-specific binding, it is suggested that functionalization is required to enhance the selectivity of the tube towards a specific analyte. Bearing in mind the results explained above, it is recommended to use a functionalization that ensures a charge transfer between the functional group and the analyte in order to exploit the sensitivity of the semi-metallic tubes towards charged species.

5.2 Future Work

One obvious extension to this work is to investigate other possible analytes. Based on the findings above, it is suggested that focus should be given to charged analytes. Charged DNA strands are obvious candidates.

Furthermore, including the effects of phonon scattering is needed to extend the study to much longer tubes ($\sim \mu\text{m}$).

It is also suggested that experimental setups should be devised to verify the results presented in this thesis. The most challenging part is the difficulty to pick semi-metallic tubes among other types of tubes. One possible way to overcome this is to use percolation to eliminate semiconducting tubes and fully-metallic tubes. The scheme has already been used to select semiconducting tubes for the fabrication of carbon-nanotube field-effect-transistors [124]. The basic idea is that using the difference in the concentration of the different types of tubes (metallic, semi-metallic, and semiconducting), setting the concentration of the nanotubes such that it is between the percolation thresholds of the different types of the tubes, one type will percolate (*i.e.*, form an uninterrupted path between two electrodes) and the other will not. A precise study is needed to specify the ratio of the semi-metallic tubes to the fully-metallic ones, and hence determine the concentration required to achieve a semi-metallic device.

Bibliography

- [1] G. Grüner, “Carbon Nanotube Transistors for Biosensing Applications”, *Analytical and Bioanalytical Chemistry*, Vol. 384, 322-335, 2006.
- [2] N. Sinha and T. John, and W. Yeow, “Carbon Nanotubes for Biomedical Applications”, *IEEE Transactions on Nanobioscience*, Vol. 4, 180-195, 2005.
- [3] K. Balasubramanian and M. Burghard, *Biosensors Based on Carbon Nanotubes*, *Analytical and Bioanalytical Chemistry*, Vol. 385, 452-468, 2006.
- [4] S. G. Wang, Q. Zhang, R. Wang, D. J. Yang, S. F. Yoon, and R. Zhang, “Low Potential Stable Glucose Detection at Carbon Nanotube Modified Gold Electrodes”, *Proceedings of the Materials Research Society*, Vol. 788, L3.46.1-L3.46.6, 2004.
- [5] G. L. Luque, N. F. Ferreyra, and G. A. Riva, “Glucose Biosensor Based on the Use of a Carbon Nanotube Paste Electrode Modified with Metallic Particles”, *Microchimica Acta*, Vol. 152, 277-283, 2006.
- [6] X. Luo, A. J. Killard, M. R. Smyth, “Reagentless Glucose Biosensor Based on the Direct Electrochemistry of Glucose Oxidase on Carbon Nanotube-Modified Electrodes”, *Electroanalysis*, Vol. 18, 1131-1134, 2006.
- [7] D. Pan, J. Chen, S. Yao, W. Tao, and L. Nie, “An Amperometric Glucose Biosensor Based on Glucose Oxidase Immobilized in Electropolymerized Poly(o-aminophenol) and Carbon Nanotubes Composite Film on a Gold Electrode”, *Analytical Sciences*, Vol. 21, 367-371, 2005.
- [8] J. Wang and M. Musameh, “Enzyme-Dispersed Carbon-Nanotube Electrodes: A Needle Microsensor for Monitoring Glucose”, *The Analyst*, Vol. 128, 1382-1385, 2003.

- [9] Y.D. Zhao, W.D. Zhang, H. Chen, and Q. Luo, "Direct Electron Transfer of Glucose Oxidase Molecules Adsorbed onto Carbon Nanotube Powder Microelectrode", *Analytical Sciences*, Vol. 18, 939-941, 2002.
- [10] J. Wang, M. Li, Z. Shi, N. Li, and Z. Gao, "Electrochemistry of DNA at Single-Wall Carbon Nanotubes", *Electroanalysis*, Vol. 16, 140-144, 2004.
- [11] K. Kerman, Y. Morita, Y. Takamura, M. Ozsoz, and E. Tamiya, "DNA-Directed Attachment of Carbon Nanotubes for Enhanced Label-Free Electrochemical Detection of DNA Hybridization", *Electroanalysis*, Vol. 16, 1667-1672, 2003.
- [12] S. Hrapovic, Y. Liu, K. B. Male, and J. H. T. Luong, "Electrochemical Biosensing Platforms Using Platinum Nanoparticles and Carbon Nanotubes", *Analytical Chemistry*, Vol. 76, 1083-1088, 2004.
- [13] X. Pang, D. He, S. Luo, and Q. Cai, "An amperometric glucose biosensor fabricated with Pt nanoparticle-decorated carbon nanotubes/TiO₂ nanotube arrays composite", *Sensors and Actuators B*, Vol. 137, 134-138, 2009.
- [14] X. Chu, B. Wu, C. Xiao, X. Zhang, and J. Chen, "A new amperometric glucose biosensor based on platinum nanoparticles/polymerized ionic liquid-carbon nanotubes nanocomposites", *Electrochimica Acta*, Vol. 55, 2848-2852, 2010.
- [15] K. Male, S. Hrapovic, Y. Liu, and J. Luong, "Electrochemical Detection of Carbohydrates using Copper Nanoparticles and Carbon Nanotubes", *Analytical Chimica Acta*, Vol. 516, 35-41, 2004.
- [16] T. S. Cho, "An Energy Efficient CMOS Interface to Carbon Nanotube Sensor Arrays", Ph.D. thesis, Massachusetts Institute of Technology, 20, 2007.
- [17] J. Wang, "Carbon-Nanotube Based Electrochemical Biosensors: A Review", *Electroanalysis*, Vol. 17, 7-14, 2005.
- [18] X. Tang, S. Bansaruntip, N. Nakayama, E. Yenilmez, Y. Chang, and Q. Wang, "Carbon nanotube DNA Sensor and Sensing Mechanism", *Nano Letters*, Vol. 6, 1632-1636, 2006.

- [19] R. J. Chen, H. Cheul Choi, S. Bangsaruntip, E. Yenilmez, X. Tang, Q. Wang, Y. Chang, and H. Dai, "An Investigation of the Mechanisms of Electronic Sensing of Protein Adsorption on Carbon Nanotube Devices", *Journal of American Chemical Society (JACS)*, Vol. 126, 1563-1568, 2004.
- [20] A. Kojima, C. Hyon, T. Kamimura, M. Maeda, and K. Matsumoto, "Protein Sensor Using Carbon Nanotube Field Effect Transistor", *Japanese Journal of Applied Physics*, Vol. 44, 1596-1598, 2005.
- [21] J. Kong and Hongjie Dai, "Full and Modulated Chemical Gating of Individual Carbon Nanotubes by Organic Amine Compounds", *Journal of Physical Chemistry B*, Vol. 105, 2890-2893, 2001.
- [22] R. Chen *et al.*, "Noncovalent Functionalization of Carbon Nanotubes for Highly Specific Electronic biosensors", *Proceedings of the National Academy of Science of the United States of America*, Vol. 100, 4984-4989, 2003.
- [23] A. Star, J. Gabriel, K. Bradley, and G. Grüner, "Electronic Detection of Specific Protein Binding Using Nanotube FET Devices", *Nano Letters*, Vol. 3, 459-463, 2003.
- [24] P. Barone, S. Baik, D. Heller, and M. Strano, "Near-Infrared Optical Sensors Based on Single-Walled Carbon Nanotubes", *Nature Materials*, Vol. 4, 86-92, 2005.
- [25] Y. Yamamoto, K. Maehashi, Y. Ohno, and K. Matsumoto, "Electrical Detection of Negatively Charged Proteins Using n-Type Carbon Nanotube Field-Effect Transistor Biosensors", *Japanese Journal of Applied Physics*, Vol. 49, 02BD10, 2010.
- [26] A. Palaniappan *et al.*, "Aligned carbon nanotubes on quartz substrate for liquid gated biosensing", *Biosensors and Bioelectronics*, Vol. 25, 1989-1993, 2010.
- [27] J. Kim, B. Lee, J. Lee, S. Hong, and S. Sim, "Enhancement of sensitivity and specificity by surface modification of carbon nanotubes in diagnosis of prostate cancer based on carbon nanotube field effect transistors", *Biosensors and Bioelectronics*, Vol. 24, 33723378, 2009.
- [28] K. Bradley, M. Briman, A. Star, and G. Grüner, "Charge Transfer from Adsorbed Proteins", *Nano Letters*, Vol. 4, 253-256, 2003.

- [29] A. Star, T. Han, J. P. Gabriel, K. Bradley, and G. Grüner, "Interaction of Aromatic Compounds with Carbon Nanotubes: Correlation to the Hammett Parameter of the Substituent and Measured Carbon Nanotube FET Response", *Nano Letters*, Vol. 3, 1421-1423, 2003.
- [30] H. Chang, J. Lee, S. Lee, and Y. Lee, "Adsorption of NH_3 and NO_2 Molecules on Carbon Nanotubes", *Applied Physics Letters*, Vol. 79, 3863-3865, 2001.
- [31] S. Mao, G. Lu, K. Yu, and J. Chen, "Specific biosensing using carbon nanotubes functionalized with gold nanoparticle-antibody conjugates", *Carbon*, Vol. 48, 479-486, 2010.
- [32] K. Maehashi, K. Matsumoto, Y. Takamura, and E. Tamiya, "Aptamer-Based Label-Free Immunosensors Using Carbon Nanotube Field-Effect Transistors", *Electroanalysis*, Vol. 21, 1285-1290, 2009.
- [33] Y. Zhao and F. Stoddart, "Noncovalent Functionalization of Single-Walled Carbon Nanotubes", *Accounts of Chemical Research*, Vol. 42, 1161-1171, 2009.
- [34] C. Roman, F. Ciontu, and B. Courtois, "Aromatic amino acids physisorbed on graphene: electronic properties and Hamiltonian reduction", *Proceedings of the European Micro and Nano Systems 2004 (EMN04)*, 273-278, Paris, France, 2004.
- [35] C. Rajesh, C. Majumder, H. Mizuseki, and Y. Kawazoe, "A theoretical study on the interaction of aromatic amino acids with graphene and single walled carbon nanotube", *The Journal of Chemical Physics*, Vol. 130, 124911, 2009.
- [36] B. J. Alder and T. E. Wainwright, "Studies in Molecular Dynamics. I. General Method", *The Journal of Chemical Physics*, Vol. 31, 459-466, 1959.
- [37] E. Lindahl, B. Hess, and D. van der Spoel, "GROMACS 3.0: a package for molecular simulation and trajectory analysis", *Journal of Molecular Modeling*, Vol. 7, 306-317, 2001.
- [38] T. U. Werder, "Multiscale Simulations of Carbon Nanotubes in Aqueous Environments", *Doctoral Thesis*, Swiss Federal Institute of Technology, Zurich, 2005.

-
- [39] Y. Guo, N. Karasawa, and W. Goddard III, "Prediction of fullerene packing in C_{60} and C_{70} crystals", *Nature*, Vol. 351, 464-467, 1991.
- [40] C. Li and T. Chou, "An Atomistic Modeling of Carbon Nanotube Tensile Strength", Proceedings of the 43rd AIAA/ASME/ASCE/AHS Structures, Structural Dynamics, and Materials Conference, AIAA-2002-1520, Denver, Colorado, 2002.
- [41] X. Hua, T. Çağın, J. Che, and W. Goddard III, "QM(DFT) and MD studies on formation mechanisms of C_{60} fullerenes", *Nanotechnology*, Vol. 11, 85-88, 2000.
- [42] J. Tersoff, "New empirical model for the structural properties of silicon", *Physical Review Letters*, Vol. 56, 632-635, 1986.
- [43] D. Brenner, "Empirical potential for hydrocarbons for use in simulating the chemical vapor deposition of diamond films", *Physical Review B*, Vol. 42, 9458-9471, 1990.
- [44] D. Brenner *et al.*, "A second-generation reactive empirical bond order (REBO) potential energy expression for hydrocarbons", *Journal of Physics: Condensed Matter*, Vol. 14, 703-802, 2002.
- [45] B. Ni, K. Lee, and S. Sinnott, "A reactive empirical bond order (REBO) potential for hydrocarbonoxygen interactions", *Journal of Physics: Condensed Matter*, Vol. 16, 7261-7275, 2004.
- [46] S. Stuart, A. Tutein, and J. Harrison, "A reactive potential for hydrocarbons with intermolecular interactions", *Journal of Chemical Physics*, Vol. 112, 6472-6486, 2000.
- [47] W.H. Duan, Q. Wang, K.M. Liew, and X.Q. He, "Molecular mechanics modeling of carbon nanotube fracture", *Carbon*, Vol. 45, 1769-1776, 2007.
- [48] N. Chen, M. Lusk, A.C.T. van Duin, W. Goddard III, "Mechanical properties of connected carbon nanorings via molecular dynamics simulation", *Physical Review B*, Vol. 72, 085416, 2005.
- [49] T. Werder, J. H. Walther, R. L. Jaffe, and P. Koumoutsakos, "Water-Carbon Interactions: Potential Energy Calibration Using Experimental Data", *Nanotechnology*, Vol. 3, 546-548, 2003.

- [50] T. Werder, J. H. Walther, R. L. Jaffe, T. Halicioglu, F. Noca, and P. Koumoutsakos, “Molecular Dynamics Simulation of Contact Angles of Water Droplets in Carbon Nanotubes”, *Nano Letters*, Vol. 1, 697-702, 2001.
- [51] E.J. Sorin and V.S. Pande, “Exploring the Helix-Coil Transition via All-Atom Equilibrium Ensemble Simulations”, *Journal of Biophysics*, Vol. 88, 2472-2493, 2005.
- [52] W. Jorgensen, J. Chandrasekhar, and J.D. Madura, “Comparison of simple potential functions for simulating liquid water”, *Journal of Chemical Physics*, Vol. 79, 926-935, 1983.
- [53] P. Ewald, “Die Berechnung optischer und elektrostatischer Gitterpotentiale”, *Annals of Physics*, Vol. 64, 253-287, 1921.
- [54] T. Darden, D. York, L. Pedersen, “Particle mesh Ewald: An $N \log(N)$ method for Ewald sums in large systems”, *Journal of Chemical Physics*, Vol. 98, 10089-10092, 1993.
- [55] R. W. Hockney, S. P. Goel, J. Eastwood, “Quiet high-resolution computer models of a plasma”, *Journal of Computational Physics*, Vol. 14, 148-158, 1974.
- [56] L. Verlet, “Computer “Experiments” on Classical Fluids. I. Thermodynamical Properties of Lennard-Jones Molecules”, *Physical Review*, Vol. 159, 98-103, 1967.
- [57] GROMACS v3.3 Manual, <http://www.gromacs.org>.
- [58] H. J. C. Berendsen, J.P.M. Postma, A. DiNola, and J.R. Haak, “Molecular dynamics with coupling to an external bath”, *Journal of Chemical Physics*, Vol. 81, 3684-3690, 1984.
- [59] W. Kahn and L. Sham, “Self-Consistent Equations Including Exchange and Correlation Effects”, *Physical Review*, Vol. 140, A1133-A1138, 1965.
- [60] K. Stokbro, J. Taylor, M. Brandbyge, and H. Guo, “Ab-initio Non-Equilibrium Green’s Function Formalism for Calculating Electron Transport in Molecular Devices”, in “Introducing Molecular Electronics (lecture Notes in Physics)”, Eds. G. Cuniberti, G. Fagas and K. Richter, (Springer: Berlin/Heidelberg), 117-152, 2005.

- [61] R.O. Jones, "Introduction to Density Functional Theory and Exchange-Correlation Energy Functionals", in "Computational Nanoscience: Do It Yourself! (Lecture Notes)", Eds. J. Grotendorst, S. Blügel, and D. Marx, John von Neumann Institute for Computing, Jülich, NIC Series, Vol. 31, 45-70, 2006.
- [62] <http://www.chemistry.mcmaster.ca/~ayers/chem770/Notes5.pdf>.
- [63] J. P. Perdew and A. Zunger, "Self-interaction correction to density-functional approximations for many-electron systems", Physical Review B, Vol. 23, 5048-5079, 1981.
- [64] G. Canto, E. Martínez-Guerra, and N. Takeuchi, "Theoretical study of acetylene adsorption on armchair nanotubes", Computational Materials Science, Vol. 42, 322-328, 2008.
- [65] E. Yu, D. Stewart, and S. Tiwari, "*Ab initio* study of polarizability and induced charge densities in multilayer graphene films", Physical Review B, Vol. 77, 195406, 2008.
- [66] J.C. Charlier, X. Gonze, and J.P. Michenaud, "Graphite Interplanar Bonding: Electronic Delocalization and van der Waals Interaction", Europhysics Letters, Vol. 28, 403, 1994.
- [67] L.A. Girifalco and M. Hodak, "Van der Waals binding energies in graphitic structures", Physical Review B, Vol. 65, 125404, 2002.
- [68] F. Tournus and J.C. Charlier, "*Ab initio* study of benzene adsorption on carbon nanotubes", Physical Review B, Vol. 71, 165421, 2005.
- [69] M. Hasegawa and K. Nishidate, "Semiempirical approach to the energetics of interlayer binding in graphite", Physical Review B, Vol. 70, 205431, 2004.
- [70] F. Tournus, J.C. Charlier, P. Mélinon, "Mutual orientation of two C₆₀ molecules: An *ab initio* study", Journal of Chemical Physics, Vol. 122, 094315, 2005.
- [71] J.C. Charlier, X. Gonze, and J.P. Michenaud, "First-principles study of the stacking effect on the electronic properties of graphite(s)", Carbon, Vol. 32, 289-299, 1994.

- [72] Y. Xue, S. Datta, and M. A. Ratner, “First-principles based matrix Greens function approach to molecular electronic devices: general formalism”, *Chemical Physics*, Vol. 281, 151-170, 2002.
- [73] M. Brandbyge, J. Mozos, P. Ordejón, J. Taylor, and K. Stokbro, “Density-functional method for nonequilibrium electron transport”, *Physical Review B*, Vol. 65, 165401, 2002.
- [74] S. Datta, “Quantum Transport: Atom to Transistor”, Cambridge University Press, 221, 2005.
- [75] W. Koch and M. C. Holthausen, “A Chemist’s Guide to Density Functional Theory”, Second edition, Wiley-VCH Verlag GmbH, 97-101, 2001.
- [76] C. J. Cramer, “Essentials of Computational Chemistry: Theories and Models”, Second edition, John Wiley & Sons Ltd., 170-175, 2002.
- [77] D. Hamann, M. Schülter, and C. Chiang, “Norm-Conserving Pseudopotentials”, *Physical Review Letters*, Vol. 43, 1494-1497, 1979.
- [78] Atomistix v.2008.10, www.quantumwise.com.
- [79] J. M. Soler, E. Artacho, J. D. Gale, A. García, J. Junquera, P. Ordejón, and D. Sánchez-Portal, “The SIESTA method for ab initio order-N materials simulation”, *Journal of Physics: Condensed Matter*, Vol. 14, 2745-2779, 2002.
- [80] G.B. Abadir, K. Walus, and D.L. Pulfrey, “Basis-set Choice for DFT/NEGF Simulations of Carbon Nanotubes”, *Journal of Computational Electronics*, Vol. 8, 1-9, 2009.
- [81] R. Saito, G. Dresselhaus, and M.S. Dresselhaus, “Physical Properties of Carbon Nanotubes”, Imperial College Press, 59-72, 2005.
- [82] K. Iyakutti, M. Rajarajeswari, and M.W.C. Dharma-wardana, “The interaction of nitrogen molecules with (4, 0) single-walled carbon nanotube: electronic and structural effects”, *Nanotechnology*, Vol. 19, 185704, 2008.
- [83] D. Shah, N.A. Bruque, K. Alam, R.K. Lake, and R.R., Pandey, “Electronic properties of carbon nanotubes calculated from density functional theory and the empirical π -bond model”, *Journal of Computational Electronics*, Vol. 6, 395-400, 2007.

- [84] M. Simeoni, S. Picozzi, and B. Delley, "An ab-initio study of pentacene on aluminum (1 0 0) surface", *Surface Science*, Vol. 562, 43-52, 2004.
- [85] N. Kurita and H. Sekino, "Ab Initio and DFT Studies for Accurate Description of van der Waals Interaction between Rare-Gas Atoms", *International Journal of Quantum Chemistry*, Vol 91, 355-362, 2003.
- [86] L.A. Girifalco and M. Hodak, "Van der Waals binding energies in graphitic structures", *Physical Review B*, Vol. 65, 125404, 2002.
- [87] P. Silvestrelli, "Van der Waals interactions in DFT made easy by Wannier functions", *Physical Review Letters*, Vol. 100, 053002, 2008.
- [88] W. Kohn, Y. Meir, and D.E. Makarov, "van der Waals Energies in Density Functional Theory", *Physical Review Letters*, Vol. 80, 4153-4156, 1998.
- [89] G.B. Abadir, K. Walus, R.F.B. Turner, and D.L. Pulfrey, "Biomolecular Sensing using Carbon Nanotubes: A simulation Study.", *International Journal of High Speed Electronics and Systems*, Vol. 18, 879-887, 2008.
- [90] D. Sung, S. Hong, Y. Kim, N. Park, S. Kim, S. Maeng, and K. Kim, "Ab initio study of the effect of water adsorption on the carbon nanotube field-effect transistor", *Applied Physics Letters*, Vol. 89, 243110, 2006.
- [91] E. Lewars, "Computational Chemistry: Introduction to the Theory and Applications of Molecular and Quantum Mechanics", Kluwer Academic Publishers, 251-253, 2003.
- [92] D.C. Young, "Computational Chemistry: A Practical Guide for Applying Techniques to Real-World Problems", John Wiley & Sons, 232, 2001.
- [93] H. Zeng, H. Fu, J. Wei, Z. Wang, L. Wang, and P. Peng, "Curvature effects on electronic properties of small radius nanotube", *Applied Physics Letters*, Vol. 91, 033102, 2007.
- [94] F. Jensen, "Introduction to Computational Chemistry", Second edition, John Wiley & Sons Ltd., 210, 2007.
- [95] N. Romero, "Density Functional Study of Fullerene-Based Solids: Crystal Structure, Doping, and Electron-Phonon Interaction," Ph.D. thesis, University of Illinois, 2005.

- [96] Y.L. Mao, X.H. Yan, Y. Xiao, J. Xiang, Y.R. Yang, and H. L. Yu, "First-principles study of the (2,2) carbon nanotube", *Physical Review B*, Vol. 71, 033404, 2005.
- [97] J. Zhong *et al.*, "Bio-nano interaction of proteins adsorbed on single-walled carbon nanotubes", *Carbon*, Vol. 47, 967-973, 2009.
- [98] R.Chen, Y. Zhang, D. Wang, and H. Dai, "Noncovalent Sidewall Functionalization of Single-Walled Carbon Nanotubes for Protein Immobilization", *Journal of the American Chemical Society*, Vol. 123, 3838-3839, 2001.
- [99] M. Shim, N. Kam, R. Chen, Y.Li, and H. Dai, "Functionalization of Carbon Nanotubes for Biocompatibility and Biomolecular Recognition", *Nano Letters*, Vol. 2, 285-288, 2002.
- [100] D. Whitford, "Proteins: Structure and Function", John Wiley & Sons: Chichester, West Sussex, 28, 2005.
- [101] Y. Kong, D. Cui, C.S. Ozkan, and H. Gao, "Modelling Carbon Nanotube Based Bio-Nano Systems: A Molecular Dynamics Study", *Proceedings of the Material Research Society Symposium 773*, N8.5.1, 2003.
- [102] X. Blase, L. Benedict, E. Shirley, and S. Louie, "Hybridization Effects and Metallicity in Small Radius Carbon Nanotubes", *Physical Review Letters*, Vol. 72, 1878-1881, 1994.
- [103] G.B. Abadir, K. Walus, and D.L. Pulfrey, "Bias-dependent amino-acid-induced conductance changes in short semi-metallic carbon nanotubes", *Nanotechnology*, Vol. 21, 015202, 2010.
- [104] M. Parrinello and A. Rahman, *Journal of Applied Physics*, "Polymorphic transitions in single crystals: A new molecular dynamics method", Vol. 52, 7182-7190, 1981.
- [105] A.T.C. Johnson, C. Staii, M. Chen, S. Khamis, R. Johnson, M.L. Klein, and A. Gelperin, "DNA-decorated carbon nanotubes for chemical sensing", *Semiconductor Science and Technology*, Vol. 21, S1721, 2006.
- [106] C. Staii, A. T. Johnson, Jr., M. Chen, and A. Gelperin, "DNA-Decorated Carbon Nanotubes for Chemical Sensing", *Nano Letters*, Vol. 5, 1774-1778, 2005.

- [107] G.B. Abadir, K. Walus, and D.L. Pulfrey, “Comment on “Curvature effects on electronic properties of small radius nanotub, [Appl. Phys. Lett. 91, 033102, 2007]”, Applied Physics Letters, Vol. 94, 176101, 2009.
- [108] G.B. Abadir, K. Walus, R.F.B. Turner, and D.L. Pulfrey, “Effect of Single-Biomolecule Adsorption on the Electrical Properties of Short Carbon Nanotubes”, Proceedings of the 8th IEEE Conference on Nanotechnology (Arlington, TX), 230-232, 2008.
- [109] H. Gokturk, “Electrical Properties of Ideal Carbon Nanotubes”, Proceedings of the 5th IEEE Conference on Nanotechnology, (Nagoya, Japan), 677-680, 2005.
- [110] P. Albrecht, S. Barraza-Lopez, and J. Lyding, “Scanning tunnelling spectroscopy and *ab initio* calculations of single-walled carbon nanotubes interfaced with highly doped hydrogen-passivated Si(100) substrates”, Nanotechnology, Vol. 18, 095204, 2007.
- [111] R. Seidel, A. Graham, B. Rajasekharan, E. Unger, M. Liebau, G. Duesberg, F. Kreupl, and W. Hoenlein, “Bias dependence and electrical breakdown of small diameter single-walled carbon nanotubes”, Journal of Applied Physics, Vol. 96, 6694-6699, 2004.
- [112] P. Collins, M. Hersam, M. Arnold, R. Martel, and P. Avouris, “Current Saturation and Electrical Breakdown in Multiwalled Carbon Nanotubes”, Physical Review Letters, Vol. 86, 3128-31, 2001.
- [113] J. Park, S. Rosenblatt, Y. Yaish, V. Sazanova, H. Ustunel, S. Braig, T. Arias, P. Brouwer, P. McEuen, “Electron-Phonon Scattering in Metallic Single-Walled Carbon Nanotubes”, Nano Letters, Vol. 4, 517-520, 2004.
- [114] A. Javey, J. Guo, M. Paulsson, Q. Wang, D. Mann, M. Lundstrom, and H. Dai, “High-Field Quasiballistic Transport in Short Carbon Nanotubes”, Physical Review Letters, Vol. 92, 106804, 2004.
- [115] R. Jasti, J. Bhattacharjee, J.B. Neaton, and C.R. Bertozzi, “Synthesis, Characterization, and Theory of [9]-, [12]-, and [18]Cycloparaphenylene: Carbon Nanohoop Structures”, Journal of the American Chemical Society, Vol. 130, 17646-17647, 2008.
- [116] T. Sano and C. Cantor, “Cooperative Biotin Binding by Streptavidin”, The Journal of Biological Chemistry, Vol. 265, 3369-3373, 1990.

- [117] G. Kurzban, E. Bayer, M. Wilchek, and P. Horowitz, “The Quaternary Structure of Streptavidin in Urea”, *The Journal of Biological Chemistry*, Vol. 266, 14470-14477, 1991.
- [118] P.C. Weber, J.J. Wendoloski, M.W. Pantoliano, and F. R. Salemme, “Crystallographic and Thermodynamic Comparison of Natural and Synthetic Ligands Bound to Streptavidin”, *Journal of the American Chemical Society*, Vo. 114, 3197-3200, 1992.
- [119] P.C. Weber, D.H. Ohlendorf, J.J. Wendoloski, F.R. Salemme, “Structural Origins of High-Affinity Biotin Binding to Streptavidin”, *Science*, Vol. 243, 85-88, 1989.
- [120] M. Radosavljević, S. Heinze, J. Tersoff, and P. Avouris, “Drain voltage scaling in carbon nanotube transistors”, *Applied Physics Letters*, Vol. 83, 2435-2437, 2003.
- [121] G. Friedli, “Interaction of Deamidated Soluble Wheat Protein (SWP) with other Food Proteins and Metals”, Ph.D. thesis, University of Surrey, 1996.
- [122] K. Odbadrakh, “Theoretical Investigations for Molecular Electronic Devices: Metal/Semiconductor Interfaces, Capacitance of atomic scale wires, and Organics on Diamond Surfaces”, Ph.D. thesis, North Carolina State University, North Carolina, USA, 2007.
- [123] J. Tersoff, “Schottky Barrier Heights and the Continuum of Gap States”, *Physical Review Letters*, Vol. 52, 465-468, 1984.
- [124] N. Pimparkar, Q. Cao, J. A. Rogers, and M. A. Alam, “Theory and Practice of “Striping” for Improved ON/OFF Ratio in Carbon Nanonet Thin Film Transistors”, *Nano Research*, Vol. 2, 167-175, 2009.

Appendix A

Chemical Structures

In this appendix, a description of the chemical structure of the different dimers used in the thesis is provided. As can be seen in Figure A.1, an amino acid in general has a central α -carbon atom, a carboxyl group, an amine group, and an R group, which is a side chain that makes the difference between one amino acid and the other. In water, amino acids are found in a “Zwitterion” configuration, with a positive charge on the protonated amine group, and a negative charge on the deprotonated carboxyl group as illustrated in Figure A.2.

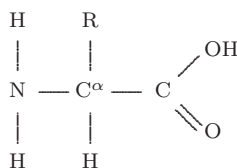


Figure A.1: Generic amino acid structure.

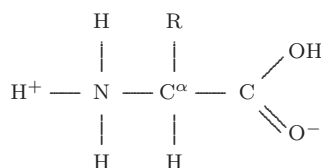


Figure A.2: Generic amino acid structure in the zwitterion configuration.

Amino acids are joined together by the formation of a peptide bond where the amino group of one molecule reacts with the carboxyl group of the other, resulting in the elimination of water as shown in Figure A.3. For the special case of a dimer, the general structure is as illustrated in Figure A.4. The different side chains of the amino acids used in this thesis are listed in Table A.1.

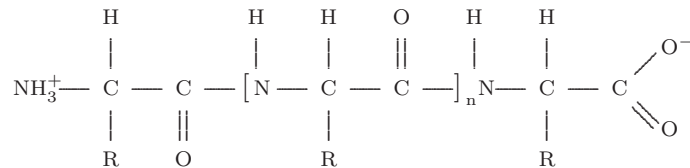


Figure A.3: Part of a polypeptide chain where n is the number of non-terminal residues.

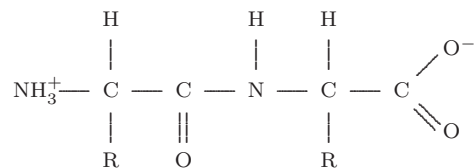


Figure A.4: General structure of an amino-acid dimer in the zwitterion configuration.

Table A.1: Side chains of the different amino acids used in the thesis.

Amino Acid	Side Chain
Arginine	$^+\text{H}_2\text{N} = \text{C}(\text{NH}_2) - \text{NH} - (\text{CH}_2)_3 -$
Asparagine	$\text{H}_2\text{N} - \text{CO} - \text{CH}_2 -$
Aspartate	$^- \text{OOC} - \text{CH}_2 -$
Glutamate	$^- \text{OOC} - (\text{CH}_2)_2 -$
Isoleucine	$\text{CH}_3 - \text{CH}_2 - \text{CH}(\text{CH}_3) -$
Phenylalanine	Phenyl - $\text{CH}_2 -$
Tryptophan	Phenyl - $\text{NH} - \text{CH} = \text{C} - \text{CH}_2 -$ <div style="text-align: center; margin-top: 5px;"> $\boxed{\hspace{10em}}$ </div>
Tyrosine	$\text{OH} - \text{Phenyl} - \text{CH}_2 -$

Appendix B

Related Publications

The following is a list of publications that are based on the research conducted for this thesis.

Journal Publications

1. G.B. Abadir, K. Walus, and D.L. Pulfrey, “Bias-dependent amino-acid-induced conductance changes in short semi-metallic carbon nanotubes”, *Nanotechnology*, Vol. 21, 015202, 2010.
2. G.B. Abadir, K. Walus, and D.L. Pulfrey, “Comment on “Curvature effects on electronic properties of small radius nanotube” [Appl. Phys. Lett. 91, 033102 (2007)]”, *Applied Physics Letters*, Vol. 94, 176101, 2009.
3. G.B. Abadir, K. Walus, and D.L. Pulfrey, “Basis-set Choice for DFT/NEGF simulations of Carbon Nanotubes”, *Journal of Computational Electronics*, Vol. 8, 1-9, 2009.
4. G.B. Abadir, K. Walus, R.F.B. Turner, and D.L. Pulfrey, “Biomolecular sensing using Carbon Nanotubes: A Simulation Study”, *International Journal of High-Speed Electronics and Systems*, Vol. 18, issue 4, 879-887, 2008.

Conference Publications

5. G.B. Abadir, K. Walus, and D.L. Pulfrey, “Modeling Sensing Mechanisms in Carbon Nanotube Biosensors”, in preparation, *IEEE Sensors 2010*, Hawaii, November 2010
6. G.B. Abadir, K. Walus, R.F.B. Turner, and D.L. Pulfrey, “Effect of Single-Biomolecule Adsorption on the Electrical Properties of Short Carbon Nanotubes”, *Proceedings of the 8th IEEE Conference on Nanotechnology (Arlington, TX)*, 230-232, 2008.